The Omnipolarizer

Julien Fatome

▶ **To cite this version:**

Julien Fatome. The Omnipolarizer. Optics / Photonic. Université Bourgogne - Franche-Comté, 2019. tel-04871900

HAL Id: tel-04871900
https://hal.science/tel-04871900v1

Submitted on 7 Jan 2025

HAL is a multi-disciplinary open access archive for the deposit and dissemination of scientific research documents, whether they are published or not. The documents may come from teaching and research institutions in France or abroad, or from public or private research centers.

L'archive ouverte pluridisciplinaire **HAL**, est destinée au dépôt et à la diffusion de documents scientifiques de niveau recherche, publiés ou non, émanant des établissements d'enseignement et de recherche français ou étrangers, des laboratoires publics ou privés.

Distributed under a Creative Commons Attribution - NonCommercial 4.0 International License

Université Bourgogne Franche-Comté

Ecole doctorale Carnot-Pasteur

Habilitation à Diriger des Recherches

Présentée par **Julien Fatome**

Ingénieur de Recherche CNRS
Laboratoire Interdisciplinaire Carnot de Bourgogne
UMR 6303 CNRS-Université de Bourgogne

L'Omnipolariseur
The Omnipolarizer

Habilitation soutenue le 18 Novembre 2019, devant la commission d'examen composée de :

Thierry CHARTIER	Professeur, Université de Bretagne, Lannion	*Rapporteur*
Arnaud MUSSOT	Professeur, Université de Lille 1, Lille	*Rapporteur*
Thibaut SYLVESTRE	Directeur de Recherche CNRS, Femto-st, Besançon	*Rapporteur*
Camille-Sophie BRES	Professeure, EPFL, Lausanne	*Examinatrice*
Guy MILLOT	Professeur, Université de Bourgogne	*Examinateur*
Alexandre BOUHELIER	Directeur de Recherche CNRS, Université de Bourgogne	*Examinateur*

www.cnrs.fr

Table of contents

ABSTRACT

This manuscript summarizes my research activities developed in the last ten years at the Laboratoire Interdisciplinaire Carnot de Bourgogne (ICB) of Dijon in the Solitons, Lasers and Optical Communications group (SLCO). The first part of this thesis provides an overview of my research activities dedicated to the study of linear and nonlinear effects occurring in optical fibers. During this last decade, I have exploited the whole richness of nonlinear dynamics occurring in optical fibers to demonstrate new physical phenomena, while always keeping in mind to achieve a good balance between fundamental science and applications. Following this rule of thumb, I have developed six main subjects of research centered on nonlinear fiber optics and dedicated respectively to the development of high repetition rate pulse sources, the all-optical control of polarization state, the exploitation of soft-glass fibers for strong spectral broadening in the mid-infrared, the study of universal physical phenomena such as dispersive shock waves based on the strong analogy between optics and hydrodynamics, the generation of polarization domain walls for data transmission or optical buffering, as well as a more recent topic dealing with nonlinear processing in few mode fibers. The second part describes in details one of these fields of research and deals with the all-optical control of the state-of-polarization of light in optical fibers. In this chapter, by means of numerical simulations, I first describe the physical basis of the polarization attraction process based on a cross-polarization interaction between two counter-propagating waves taking place in an optical fiber. Then, I report several experimental demonstrations and proof-of-principle experiments of optical functionalities dedicated to optical communications based on a device called Omnipolarizer. The last part of this chapter is then dedicated to future and on-going perspectives. Finally, the last part of this manuscript reports my curriculum vitae, including project management and supervising activities as well as a complete list of my publications, invited conferences, patents, book chapters as well as broad audience actions. Through this thesis, I aim to demonstrate my ability to lead international research activities and young researcher's management, in order to be graduate with the French HDR degree.

RÉSUMÉ

Ce manuscrit résume mes activités de recherche réalisées au cours de ces dix dernières années au sein de l'équipe Solitons, Lasers et Communications Optiques (SLCO) du Laboratoire Interdisciplinaire Carnot de Bourgogne (ICB) de Dijon. La première partie de ce mémoire est dédiée à fournir au lecteur une vue globale de mes activités de recherche portant sur l'optique non linéaire dans les fibres optiques. La deuxième partie décrit en détails mes travaux de recherche entrepris dans le cadre de mon activité portant sur le contrôle tout-optique de la polarisation au sein de fibres optiques. Nous y décrivons successivement les aspects fondamentaux, confortés par des simulations numériques, nos observations expérimentales, ainsi que plusieurs démonstrations de principe dédiées aux systèmes de communications optiques à travers le développement d'un prototype appelé Omnipolariseur. In fine, la dernière partie de ce manuscrit contient mon curriculum vitae ainsi qu'une liste complète de mes contributions, à savoir, liste de mes publications dans des revues à comité de lecture, brevets, chapitres de livre, vulgarisation et conférences invitées. La rédaction de ce mémoire tend à démontrer mes capacités à maîtriser une activité de recherche dans un domaine scientifique ainsi que mon aptitude à encadrer de jeunes chercheurs (doctorants, post-doctorants) en vue d'obtenir le diplôme d'habilitation à diriger des recherches.

À Adrien, Tristan, Lilou et Emilie
À Babou
Et à tous ceux qui ont inspiré et contribué de près ou de loin à ces recherches

RESEARCH ACTIVITIES

The first part of this thesis reports an overview of my main research activities that I developed all along my career at the Laboratoire Interdisciplinaire Carnot de Bourgogne and dedicated to the study of linear and nonlinear effects taking place in optical fibers. The results obtained in the context of the following scientific activities allow me to publish more than 110 publications with more than 150 different co-authors.

Pulse train generation

During my PhD (2001-2004) under supervision of Prof. Guy Millot, I acquired all the basis of linear and nonlinear effects taking place in optical fibers. During this period, we developed new concepts for generation, propagation and characterization of high repetition rate pulse trains. For instance, in 2002, we demonstrated for the first time the generation of high-quality 160-GHz repetition rate pulse trains through the nonlinear compression of an initial beat-signal within a single segment of anomalous dispersive optical fibre by means of a multiple four-wave mixing process [P113]. The main advantage of this technique, compared to other methods reported so far, is the capacity of generating high-quality, well-separated pulse trains by means of a quite simple experimental setup. This process was then studied in different experimental configurations in order to enlarge the range of applications. Among them, we demonstrated in 2006 the generation of femtosecond pulses at repetition rates of several THz [P101]. Subsequently, we optimized this process for telecom applications and demonstrated that this kind of pulse sources can be exploited for optical time division multiplexing applications (OTDM) [P64]. Moreover, in the aim to find possible industrial partners, we also developed a user-friendly pulse source prototype delivering picosecond pulse trains at 40 GHz. The following figure summarizes 10 years of research dedicated to the generation of high repetition rate pulse trains.

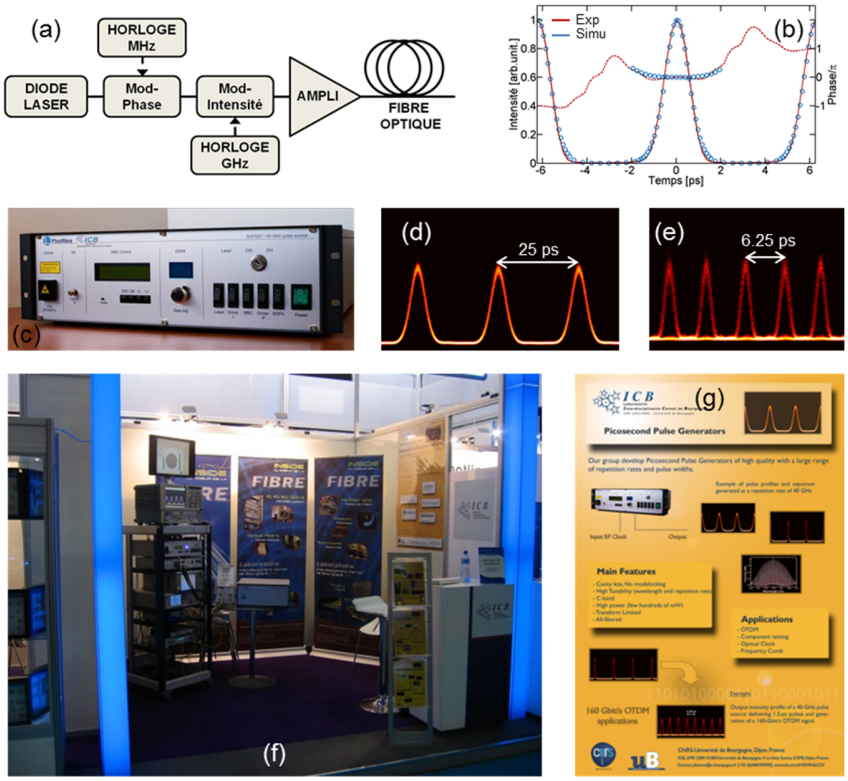

Fig-In. 1. (a) Experimental setup. (b) Intensity and phase profiles of the first 160-GHz pulse train demonstration obtained in 2002. (c) *So Fast* prototype. (d) Output intensity profile of the 40-GHz pulse train. (e) Eye-diagram of the output 160-Gbit/s OTDM signal. (f-g) Picture of the ECOC'11 exhibition booth in Geneva and data-sheet.

Fig-In.1a depicts the main experimental setup, while Fig-In.1b reports the first experimental demonstration obtained in 2002 at 160 GHz characterized by means of a home-made frequency resolved optical gating device (FROG). Fig-In.1c illustrates the final 40-GHz *So Fast* prototype designed in 2012 in collaboration with Photline technologies as well as the output pulse train in (d). Fig-In.1e displays the eye-diagram after a second stage of nonlinear compression and temporal multiplexing obtained at 160 Gbit/s for OTDM applications. Finally, this prototype has been showcased on the ECOC exhibition with a live demonstration (f-g).

Chalcogenide optical fibers

I also contributed to a research activity dealing with the characterization and exploitation of chalcogenide and tellurite optical fibers for the development of all-optical functionalities and supercontinuum generation. Indeed, thanks to their strong nonlinear coefficient (~2 orders of magnitude higher than silica) and wide transmission windows, these soft-glass fibers are excellent candidates for numerous applications in the infrared and mid-infrared spectral regions, such as supercontinuum generation or spectroscopy. This activity was carried out mainly between 2007 and 2013, in particular in the context of the ANR project FUTUR, in collaboration with the group of F. Smektala from our laboratory, the University of Rennes and FOTON-ENSSAT laboratory in Lannion. During this period, we performed a complete characterization of the different physical effects taking place in microstructured chalcogenide fibers, namely, chromatic dispersion, birefringence, Kerr effect, Brillouin and Raman effects in order to develop compact all-optical functionalities [P86]. The second way of research aimed to exploit the high nonlinear properties and large infrared transparency of such fibers to extend spectral broadening beyond the traditional 2.1-µm silica limit. Large spectral expansion were achieved via supercontinuum generation in concatenated systems [P68] or thanks to high peak-power femtosecond pumping [P54]. The following picture illustrates the experimental results obtained in 2012 during my stay in Nagoya at the Toyota Technological Institute (TTI) in the group of Prof. Ohishi. The fibers were fabricated in our laboratory and pumped in the femtosecond regime by means of a high-power OPO system available at the TTI. Fig-In.2a displays the cross-section of a typical suspended-core microstructured tellurite fiber under investigation. Subplot (b) illustrates the generation of third harmonic in the early stage of propagation, while panel (c) depicts the resulting spectral broadening as a function of the injected power.

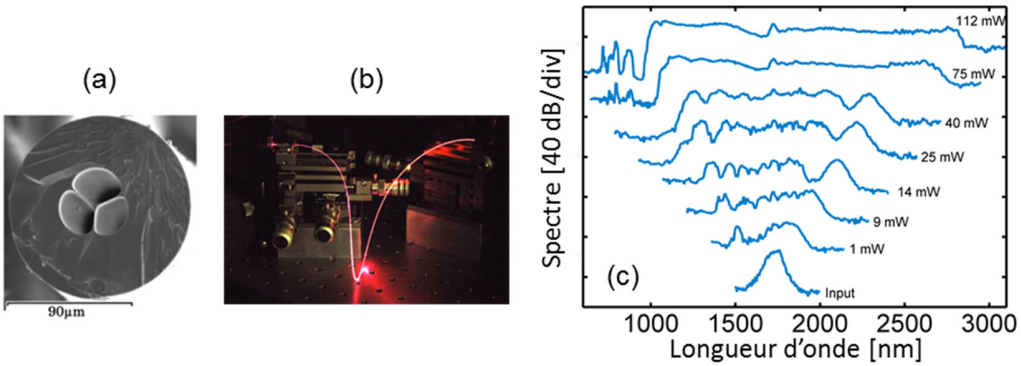

Fig-In. 2. (a) Cross-section of the microstructured tellurite fibre under-test. (b) Third harmonic generation along the fiber length. (c) Supercontinuum expansion as a function of pump power [P54].

Polarization attraction

The all-optical control of light state-of-polarization (SOP) propagating in optical fibre constitutes my main research activity of the last ten years, particularly in the context of my ERC starting grant PETAL (Polarization condEnsation for Telecom AppLications, 2012-2017). Indeed, despite the impressive improvements in the manufacturing process of modern optical fibers, the residual birefringence of the fiber

and its surroundings i.e. mechanical stress, bending, temperature fluctuations and so on, make the SOP of light completely unpredictable after a few tens of meters of propagation. Consequently, in order to exploit the light SOP as a full-controllable degree of freedom, it was highly desirable to develop an all-optical device enabling a lossless repolarization. This field of research started in 2008 in the context of the ANR FUTUR project. We demonstrated for the first time around 1.55 µm into a 2-m long segment of highly nonlinear fiber (HNLF) that a fixed polarized pump wave can act as a strong polarization attractor for any arbitrary polarized counter-propagating signal wave owing to a cross-polarization four-wave mixing interaction [P93]. An important step towards applications was achieved in 2010 when we demonstrated the all-optical control of the SOP of telecom signals in km-long standard optical fibers [P63, P77]. Thereafter, in 2012, as described in details in the following part of this manuscript, we show that this polarization attraction process can still occur in absence of any external SOP reference within a device called Omnipolarizer [P53]. In such a system, the incident light beam nonlinearly interacts with its own backward replica generated at the fiber end by means of a reflective element. In such a system, the light beam is then capable to self-organize its own SOP in a highly efficient manner, as shown in the following illustrations of Fig-In.3 for a 40-Gbit/s polarization scrambled incident signal.

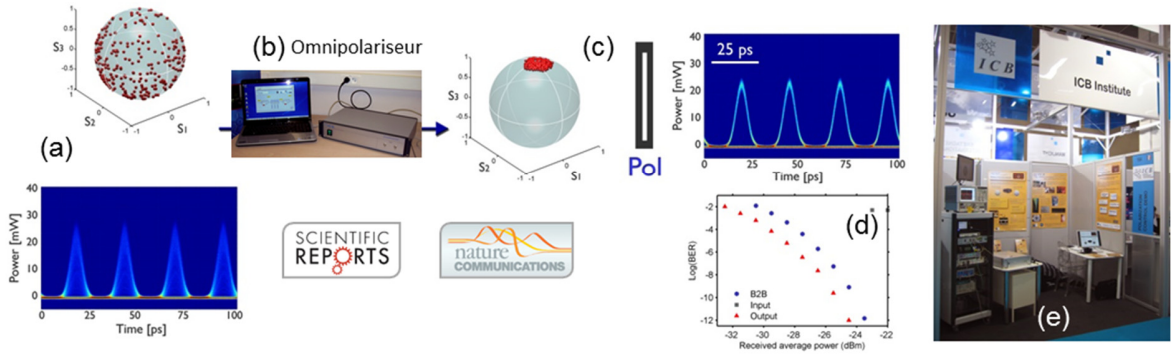

Fig-In. 3. From left to right (a) 40-Gbit/s polarization scrambled incident signal represented on the Poincaré sphere and corresponding eye-diagram monitored beyond a polarizer. (b) Omnipolarizer prototype. (c) Output self-repolarized signal and corresponding eye-diagram. (d) Bit-error-rate (BER) measurements. (e) ECOC'10 exhibition in Torino.

Hydrodynamics with Photons

Optical fibers and their intrinsic nonlinearity provide a powerful test-bed platform capable of mimicking fluid-type dynamics by means of photons. Indeed, the light-fluid analogy and advantages of all-fibre setups (compactness, perfect control over launching conditions, and possibility of direct observations) has allowed us to highlight striking wave phenomena which are often difficult to study or reproduce in their original environment such as rogue waves or dispersive shock wave (DSW) phenomena. The most celebrated example was our common publication in Nature Physics with J. Dudley in 2010, which reports the first experimental observation of Peregrine Soliton in fiber optics [P74]. Afterward, such a result has had a huge impact in the rogue wave community as the first experimental evidence of freak wave prototype. On the other hand, the formation of dispersive shock waves is also a fundamental mechanism encountered in many fields of science, and in particular in hydrodynamics. One of the most fascinating manifestations of DSWs in nature is for instance the appearance of the popular Mascaret wave, which can be generated in specific river estuaries due to a counter-flow between tide and current, resulting in the formation of large undular tidal bores travelling up-stream in a shallow water configuration. Since time immemorial, the group of Dijon has established a strong collaboration with Prof. S. Trillo dealing with nonlinear fiber optics and in particular on the analogy of DSWs in-between hydrodynamics and nonlinear optics. In optical fiber, the DSW formation occurs in defocusing regime and originates from the regularization of a gradient catastrophe

through chromatic dispersion, leading to an expanding area filled with fast oscillations. One of our main contributions was obtained in 2014 with the first experimental observation of DSWs induced formation of undular-bores and their subsequent collisions in a fibre system, illustrated here in Fig-In.4b [P36]. The process underlying this nonlinear dynamics was based on the self-phase modulation effect in normal dispersion regime leading to wave breaking. More recently, we have also reported the first experimental observation of ballistic DSW in optical fibers [C6]. In this experiment, in analogy with a supersonic object propagating through an inviscid perfect fluid, we have exploited the vectorial properties of the optical fiber to trigger a double piston shock imprinted on a continuous-wave background through a cross-phase modulation interaction induced by a high power piston pulse. The nonlinear phase profile imparted on the probe results in the formation of two oscillating fronts moving away from each other with opposite velocities, giving rise to an expanding zone of zero intensity, as depicted in Fig-In.4c.

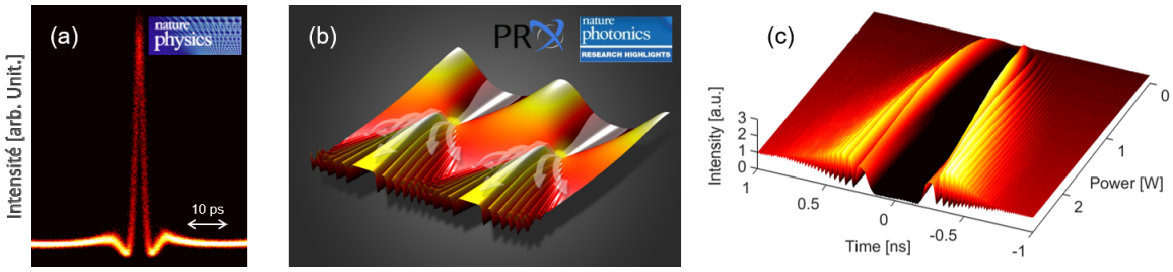

Fig-In. 4. (a) Experimental recording of the Peregrine soliton. (b) Numerical illustration of colliding undular bores in the defocusing regime of an optical fiber. (c) Experimental monitoring of a ballistic shock wave through cross-phase modulation in optical fiber.

Polarization domain walls

A domain wall (DW) is a type of topological defect that connects two stable states of a physical system. DWs are known to form as a result of a spontaneous symmetry breaking phase transition in a variety of contexts, among which the most popular are magnetism, condensed matter or Bose-Einstein condensates. They have been widely studied in ferromagnetic materials, in which they are known to bind regions in which all magnetic dipoles are aligned in opposite directions. Their equivalents in optics have been predicted theoretically a long time ago in the spatial and in the temporal domain and can be described as polarization knots (the field switches between two opposite handedness circular polarization states). While the spatial polarization domain wall (PDW) is directly connected to the polarization attraction process as I will show in the next chapter, the temporal PDW counter-part relies on the compensation between cross-phase modulation and normal chromatic dispersion. These temporal structures were predicted more than 25 years ago and have had never been observed so far. It was only recently that we performed the first generation and observation of PDWs in standard optical fibers. I attribute this success in the very low residual birefringence of modern optical fibers provided by the fast spinning process imposed during the drawing stage of the manufacturing process. This weak level of birefringence enables us to demonstrate the transmission of 40-Gbit/s optical PDWs in a 50-km long fiber line with a record of nonlinearity, as depicted in Fig-In.5a [P21]. More recently, in strong collaboration with the group of S. Coen and M. Erkintalo at the University of Auckland, in which I spent one term in 2015 and 2017, as well as with F. Leo from ULB, we have also highlighted and exploited the generation of PDWs in fiber Kerr resonators. In this dissipative configuration, the formation of these polarization knots is then based on a symmetry breaking phenomenon. This finding allows us to demonstrate a polarization based all-optical buffer, illustrated in Fig-In.5c by means of the recirculation of a PDW pattern in a 10-m long fiber ring, corresponding to a total equivalent distance of 3000 times the earth circumference [C4].

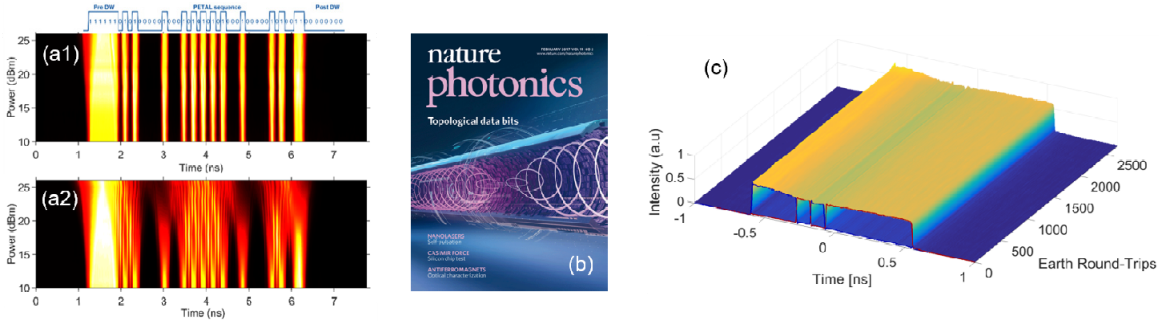

Fig-In. 5. (a) Experimental observation of PDWs transmission. (a1) Both polarization components of PDWs propagate. (a2) Only one polarization component propagates. (b) Cover of Nature Photonics illustrating our PDWs article. (c) Experimental recordings of a PDW pattern circulating within a 10-m long spun fiber cavity.

Parametric process in few-mode fibers

To conclude this short overview of my research activities, one of my recent topic deals with the exploitation of nonlinear effects in few-mode fibers (FMF). In fact, to match the continuously increasing data traffic in optical networks and to prevent a "capacity crunch" in the next decades, space-division multiplexing (SDM) has emerged as a breakthrough technology for modern optical communications. Therefore, more than 30 years after the pioneer experiments reported by R. H. Stolen, the development of SDM technology has generated a renew of interest for nonlinear parametric phenomena in FMF fibers. In this context, a new collaboration has been established between our Lab, the Prysmian group and the University of Lille. Fig-In.6 illustrates our first results recently published in Optics Express [P4]. In this work, we have demonstrated a simultaneous threefold modal and wavelength conversion process of a 10-Gbit/s signal in a 1.8-km long FMF thanks to multiple phase-matched inter-modal four wave mixing processes.

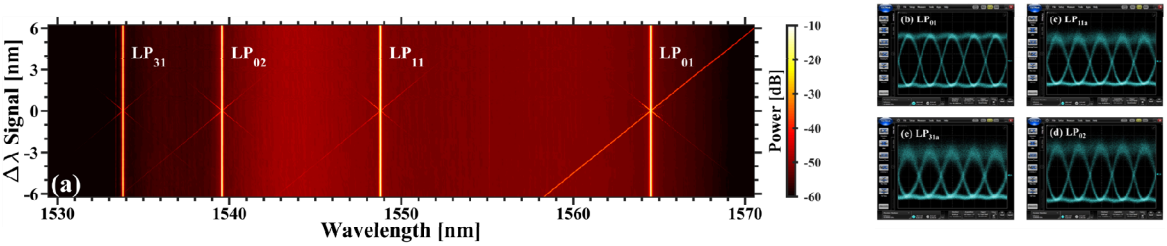

Fig-In. 6. (a) Experimental observation of simultaneous inter-modal four-wave mixing in a 6-LP FMF as a function of the input signal wavelength. (b-d) Eye-diagrams of the converted 10-Gbit/s idler waves.

All-optical signal processing based on self-induced polarization attraction in optical fibers: the Omnipolarizer

Summary. In this chapter, I will review our work dealing with the all-optical control of the light state-of-polarization in optical fibers upon propagation in a system called Omnipolarizer. More precisely, in this device we exploit the capability of light to self-organize its own state-of-polarization within optical fibers, towards universal and environmentally robust states. The underlying physical mechanism consists in a nonlinear cross-polarization feedback interaction between an arbitrary polarized incident signal and its own counter-propagating replica generated at the fiber end by means of a reflective element. Depending on the power ratio between both twin waves, e.g. the reflective coefficient, this self-repolarization process offers a rich variety of nonlinear dynamics for which we have highlighted and exploited the main three working regimes, identified by first a bistable behavior, then a polarization alignment process and finally a genuine chaotic scrambling regime. We have fully characterized these three operating regimes and found an excellent agreement between our theoretical/numerical predictions and experimental observations. Moreover, beyond the fundamental aspect of these studies, we have also exploited this self-induced repolarization phenomenon in order to implement several proof-of-principle experiments for all-optical signal processing. In particular, we have exploited the self-induced polarization tracking regime for all-optical data processing and successfully demonstrated the spontaneous repolarization of a 40-Gbit/s On-Off keying (OOK) optical signal without noticeable impairments. The bistability and associated hysteresis properties of the Omnipolarizer have been later involved to implement an optical flip-flop memory as well as a 10-Gbit/s polarization-based data packet router. We have finally taken advantage of the chaotic dynamics of our device to demonstrate an all-optical scrambler which enables a powerful polarization scrambling process with moving speeds up to 600-krad/s. The performance of this all-optical scrambler was evaluated on a 10-Gbit/s OOK telecom signal achieving an error-free transmission. To complete this part, we then describe how these temporal and chaotic polarization fluctuations can be harnessed as an all-optical random bit generator. To this aim, a billion-bit sequence was experimentally generated and successfully confronted to the dieharder benchmarking statistic tools. Interestingly, we also demonstrate that an arbitrary polarized incident signal, injected simultaneously at both sides of a standard telecommunication optical fiber can self-organize its SOP around two pools of attraction at the exact middle-point of the fiber. This system can be well understood as an unfolded version of the Omnipolarizer, outspread along the output mirror. Furthermore, in one of the final sections, we revealed a fascinating aspect of the Omnipolarizer, called polarization-based tunneling effect, for which the strong local coupling between the two counter-propagating waves has enable us to instantaneously let "jump" a polarization information onto the reflected signal, long before the expected time-of-flight induced by the round-trip along the fiber span. Finally, we discuss how the concept of self-organization could be generalized to multimode fibers, which paves the way to new important applications in the framework of spatial mode division multiplexing. In the last section, we conclude and derive some ongoing and future outlooks.

I. INTRODUCTION ON THE POLARIZATION ATTRACTION PROCESS

Among the three independent features that characterize a light beam propagating within a monomode optical fiber, namely the frequency, the energy and the state-of-polarization (SOP), the SOP remains the most difficult to predict and control. Indeed, despite outstanding technological developments in many fields of photonics, especially in all-fiber based systems, the SOP of light remains the most elusive of all parameters, which is still challenging to predict and master. In fact, it is noteworthy that in the past decade tremendous and impressive advances in the manufacturing of modern optical fibers have been carried out. In particular, by implementing well-optimized spinning process during the drawing stage, fiber providers now offer standard telecom fibers with spectacular weak levels of polarization-mode dispersion (PMD) [1-4]. Nonetheless, the amount of residual birefringence combined with surrounding stress and variations such as bending, squeezing, vibrations or temperature fluctuations still make the polarization of light genuinely unpredictable after only a few hundreds of meters of propagation in standard single mode fibers [5-10].

To overcome the impairments induced by this random nature of polarization in fiber-based systems,

from a general point of view, the mitigation solutions implemented nowadays mainly rest upon combative strategies rather than on a preventive strategy. For instance, in current high-capacity coherent transmissions, polarization impairments such as polarization randomness, polarization-mode dispersion [11-15], polarization depending loss [16] or cross-polarization interaction [17-18] are efficiently managed by means of digital signal processing (DSP) implemented at the coherent receiver [19-21].

Regarding highly polarization dependent systems such as on-chip integrated optical circuits or fiber-based nonlinear processing devices, special design and more or less complex polarization-insensitive schemes (polarization diversity, bi-directional loop or polarization splitting/recombination) may ensure the mitigation of polarization dependent performances [22-25]. From a different perspective, another elegant strategy consists in mastering the SOP of light in order to prevent or mitigate some of these impairments. The most common and commercially available way is to implement an opto-electronic polarization tracking solution [26-30]. These devices generally consist in linear polarization transformations followed by partial diagnostic associated with an active feedback loop control driven by complex algorithms. Thanks to these techniques, records of polarization tracking or diversity speeds have been achieved, reaching several of Mrad/s [31-32]. Nevertheless, these devices are essentially based on opto-electronic technologies, which could be seen as a limitation for future all-optical transparent networks. In this context and beyond its fundamental interest, the light-by-light polarization control represents a complementary and alternative approach. Indeed, the ability to all-optically master or trap the SOP of a propagating light beam without polarization depending loss could encounter numerous applications in photonics.

To this aim, several techniques have emerged in the literature in order to develop an “ideal polarizer” which could lead to a complete repolarization of an incident light with 100% of efficiency, whilst preserving the quality of the temporal intensity profile. “Ideal” here meaning: without polarization depending loss in contrast to classical polarizers. As opposed to these traditional polarizers which vanish 50% of an unpolarized incoming signal, Heebner *et al.* first proposed in 2000 a “universal polarizer” performing repolarization of unpolarized light with high efficiency [33]. Subsequently, this phenomenon of polarization attraction or polarization pulling has been the subject of a growing interest in the optical fiber community, involving the Raman effect [34-38], the stimulated Brillouin backscattering [39-40], the parametric amplification [41-42] as well as a counter-propagating four-wave mixing process, also called nonlinear cross-polarization interaction [43-58]. In particular, considering the counter-propagating interaction of two distinct optical beams injected at both ends of an optical fiber, it has been shown that an arbitrary polarized incident signal can be attracted toward a specific SOP, which is fixed by the backward pump SOP [46]. Several manifestations of this phenomenon of polarization attraction have been reported in the literature in conjunction with various types of optical functionalities, e.g., pulse reshaping [52], noise cleaner [53], data packet processing [55], phase shift-keying signal repolarization [56], Raman amplification [57] as well as spatial mode conversion [58]. According to these works and as demonstrated in the following section, the generally accepted point of view is that the injection of a pump beam at the fiber output is a prerequisite for the existence of the phenomenon of polarization attraction. The idea is that the fully polarized pump beam serves as a SOP reference for the signal beam, and thus plays the role of natural attractor for an incident unpolarized signal. However, the drawback of this system is that one need an in-site and stable SOP pump wave to ensure the attraction process.

In contrast with this common belief, we have been wondering since 2011 how to simplify this system. Is that possible to imagine a pump-free configuration? So as to avoid the needs of an external SOP reference. In other words, to force the incoming signal to self-organize its own SOP. Our proposed solution, based on a self-attraction process was then successfully submitted to the European Research Council (ERC) and funded under the ERC starting Grant PETAL (Polarization condEnsation for Telecom AppLications). The fundamental idea was to introduce a feedback loop system in which a single reflecting element is inserted at the output of the fiber so as to let the signal nonlinearly evolve to its own initiative with a particular mirror-like boundary condition. More precisely, in such a system, the signal beam interacts with its own counter-propagating replica, which can be generated at the fiber end by means of a Fiber Bragg Grating reflector (FBG), coating, or for more flexibility an amplified reflective fiber loop setup [59-61]. Unexpectedly, it was effectively demonstrated that this polarization attraction process can well occur in the

absence of any external SOP reference. The *Omnipolarizer* was born in which the incoming signal self-references its own SOP [59-60].

The aim of this chapter is to provide a general overview of the dynamics and applications of this phenomenon of self-induced polarization attraction process carried out during almost the whole last decade. In particular, after introducing the general mechanism of polarization attraction process in optical fibers, we will subsequently describe the principle of operation and experimental implementation of the Omnipolarizer. In a third part of this review, we will report the existence and exploitation of three different working regimes, i.e. the polarization alignment regime, the bistability regime and finally the chaotic regime. All of these peculiar regimes have been fully exploited to provide several proof-of-principles for telecom applications including the self-induced polarization tracking of a 40-Gbit/s On/Off Keying signal [59], an optical memory and 10-Gbit/s data packet routing operation [61], an all-optical scrambler and a random number generator [62-63] as well as the combination of these regimes to demonstrate a polarization-based cloaking operation [60]. In the later part of this manuscript we will demonstrate that an unfolded version of the Omnipolarizer, that is to say the symmetrical deployment of the Omnipolarizer with respect to the output mirror can provide a self-polarization process of an arbitrary polarized incident signal at the exact middle point of an optical fiber [64-70]. We will also highlight a novel intriguing behavior of the Omnipolarizer, based on the strong local coupling between the two counter-propagating waves, which allows us to instantaneously induce a "jump" of polarization information onto the reflected signal, long before the expected time-of-flight into the fiber span, which may be described as a polarization-based tunneling effect [71]. Finally, in the last sections we will discuss new perspectives for the generalization of this concept to multimode fibers, and trace out some conclusions, outlooks and current investigations.

II. ON THE ORIGIN OF THE POLARIZATION ATTRACTION PROCESS

The origin of the polarization attraction process can be understood, from my point of view, as a direct consequence of the existence of the spatial polarization domain wall soliton described in 1987 by Zakharov and Mikhailov [72]. This soliton represents a spatial transition of two stable states of co-rotating circular polarization SOPs within an infinite isotropic Kerr medium, here an optical fiber. In its simplest form, it represents a spatially localized polarization switching in the middle point of the fiber between the right- and left-handed circular SOPs of two counter-propagating waves of equal power [72-75]. This soliton originates from the fact that for a system of two counter-propagating waves injected at both ends of an isotropic nonlinear Kerr medium, the only stable polarization configuration relies on two co-rotating circular SOPs, as suspected by Kaplan in 1983 [76]. Any other couples of SOPs are unstable and then will spontaneously relax towards this particular arrangement of co-rotating SOPs [76-78]. It can be interpreted in terms of symmetry breaking phenomenon due to the mutual Kerr interaction, in a similar way observed recently in counter-rotating dissipative Kerr microresonators [79-80] and also described by Kaplan *et al.* as soon as the early 80s' for Sagnac interferometer [81]. In fact, when the two counter-propagating waves interact nonlinearly in a Kerr medium with arbitrary polarization states, they induce an intensity dependent non-reciprocal birefringence, thus different velocities for both forward and backward waves, due to the cross-polarization coupling. This mutual light-induced birefringence is highly sensitive and thus makes the system unstable [78]. Consequently, the system will relax preferentially towards a reciprocal stationary regime offering a mutual birefringence equilibrium, namely two co-rotating circular SOPs. This specific mutual arrangement of co-rotating SOPs is a kind of velocity locking and can be also interpreted in terms of nonlinear grating. Indeed, the nonlinear grating induced by the superposition of the forward and backward waves is stable in time (no velocity) and against a small perturbation only if the two waves travel at the same speed, which only occurs for co-rotating SOPs, thus creating a stable standing wave for the system.

In order to illustrate these fundamental properties, let's first introduce the theoretical model. u and $\bar{u}$ depict the right circular components of both counter-propagating waves, while v and $\bar{v}$ their left-circular components, respectively. The propagation of both waves in an isotropic fiber can therefore be modeled by [75, 82]:

$$\begin{cases} \dfrac{\partial u}{\partial t} + c\dfrac{\partial u}{\partial z} = i\dfrac{2}{3}\gamma[(|u|^2 + 2|v|^2)u + 2(|\bar{u}|^2 + |\bar{v}|^2)u + 2\bar{u}\bar{v}^*v] \\ \dfrac{\partial v}{\partial t} + c\dfrac{\partial v}{\partial z} = i\dfrac{2}{3}\gamma[(|v|^2 + 2|u|^2)v + 2(|\bar{u}|^2 + |\bar{v}|^2)v + 2\bar{u}^*\bar{v}u] \\ \dfrac{\partial \bar{u}}{\partial t} - c\dfrac{\partial \bar{u}}{\partial z} = i\dfrac{2}{3}\gamma[(|\bar{u}|^2 + 2|\bar{v}|^2)\bar{u} + 2(|u|^2 + |v|^2)\bar{u} + 2uv^*\bar{v}] \\ \dfrac{\partial \bar{v}}{\partial t} - c\dfrac{\partial \bar{v}}{\partial z} = i\dfrac{2}{3}\gamma[(|\bar{v}|^2 + 2|\bar{u}|^2)\bar{v} + 2(|u|^2 + |v|^2)\bar{v} + 2u^*v\bar{u}] \end{cases} \quad (1)$$

Where γ is the nonlinear Kerr coefficient of the medium. In the left side of Eqs. (1), we can first notice the opposite sign for group velocity in the equations of $\overline{wave}$, simply imposed by the counter-propagating configuration. In the right side of Eqs. (1), we retrieve subsequently the self-phase modulation effect, then the different cross-phase modulation terms and finally, the four-wave mixing interaction (FWM), responsible for the exchange of energy between left and right circular SOPs. We can also notice that there is no exchange of energy between the two waves, the power of each wave is conserved during propagation (losses are neglected here because they do not change the main dynamics). Indeed, the coupling between the counter-propagating waves is essentially a nonlinear phase term and the energy is only transferred inside the waves between the circular components. Since the general dynamics is governed by the last FWM term, note that in order to maximize its efficiency, both waves have to be centered at the same frequency to fulfill the phase matching condition imposed by the counter-propagating configuration (mainly in order to remove the propagation constant terms in the phase matching expression). Finally, chromatic dispersion (as well as its interaction with the Kerr effect) is also neglected since both waves are supposed to be continuous. We only focus our study on the spatio-temporal dynamics of both wave SOPs, (possible modulationnal instability effects is for instance vanished). It is then more convenient to use the Stokes formalism in order to simplify the above model. To this aim, we indicate with S=[S_1,S_2,S_3] and J=[J_1,J_2,J_3] the Stokes vectors associated with the forward and backward waves, respectively. More precisely, the forward wave S can be calculated as $S_1 = iu^*v + cc, S_2 = u^*v + cc, S_3 = |u|^2 - |v|^2$ (same procedure for the backward J wave). Finally, the spatiotemporal dynamics of S and J in the isotropic fiber is ruled by the following coupled nonlinear partial differential equations [72-73]:

$$\begin{cases} c^{-1}\partial_t S + \partial_z S = S \times DS + 2S \times DJ \\ c^{-1}\partial_t J - \partial_z J = J \times DJ + 2J \times DS \end{cases} \quad (2)$$

where D=γdiag(-2/3,-2/3,0) is a diagonal matrix. Note here that the two circular Stokes components (S_3 and J_3) of both waves don't interact together (null third coefficient in the D matrix), which underlines the fact that these circular components play an important role in the dynamics of the system.

Despite their simplicity, Eqs. (2) capture all the essential properties of the polarization dynamics involved within the polarization attraction process. Eqs. (2) can be numerically resolved by means of a traditional split-step method or/and Runge-Kutta algorithm. The only refinement, compared to basic single direction NLS propagation, is that Eqs. (2) have to be resolved in time instead of z. Basically, it means that an input condition feeling the whole fiber length is first introduced and subsequently, for each step of resolution in time, the field has to be recalculated in all z.

Let us first introduce the symmetry breaking phenomenon of linearly polarized counter-propagating waves of equal powers. This first approach will illustrate the universal rule of thumb, according to which, only co-rotating circular SOPs are stable upon counter-propagating nonlinear regime. For simplicity, we consider here only the circular components S_3 and J_3 of both waves, since they drive all the physical mechanism under-study. The simulations are also normalized in terms of power, i.e. the length of the fiber is normalized by the nonlinear length defined as $L_{nl}=1/\gamma P$ with P the input power. Figure 1a displays the

stationary states obtained when the two counter-propagating waves nonlinearly interact in a fiber with L=4 and boundary conditions close to linear SOPs. The final forward and backward waves are depicted with red (blue) triangles, while the injected conditions are displayed with black stars (S_3=0 and J_3=0), respectively. Note that in absence of noise, S_3 is here fixed slightly different from 0 (S_3=δ=10^{-3}) in order to reach faster the stationary regime. As expected by the pioneering works reporting in refs. [76-78], the only stable polarization configuration relies on a mutual reciprocal equilibrium, involving two co-rotated circular SOPs. Consequently, the system spontaneously targets this particular balance of co-rotating SOPs (S_3=J_3=±1), while satisfying the boundary conditions imposed at both edges of the fiber (S_3=0), leading to bell-shaped trajectories. More precisely, the system converges to the upper stationary trajectory if S_3 is slightly positive (+δ) and follows the second bottom path as soon as S_3 becomes negative (-δ). Since both boundary conditions are close to each over, the co-rotating arrangement is thus achieved at the exact middle point of the fiber.

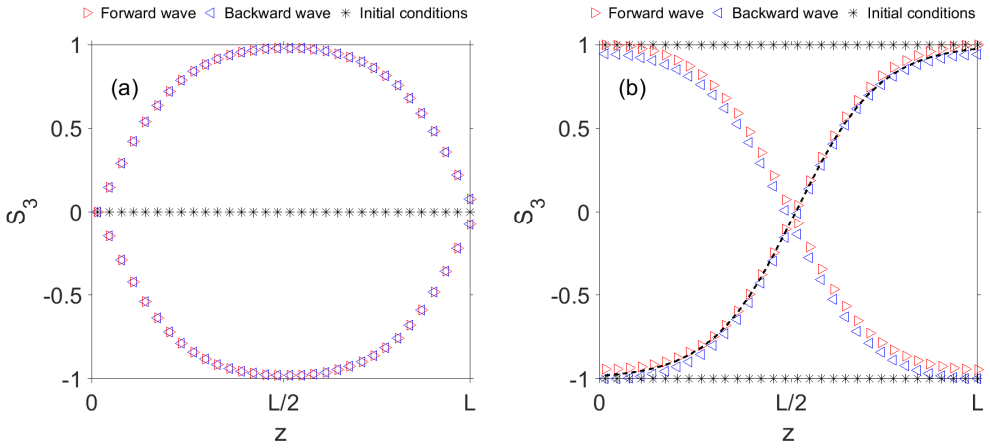

Fig. 1. (a) Stationary regime obtained in an isotropic fiber for an input condition (stars) close to a linear SOPs for both counter-propagating waves, here L=4. Forward wave (red triangles) interacts with the backward wave (blue triangle) in such a way to reach the only stable state of the system: co-rotating circular states. The upper trajectory corresponds to an input condition S_3=0.001, J_3=0, while the bottom trajectory corresponds to S_3=-0.001, J_3=0. (b) Spatial polarization domain wall (PDW). The input conditions (black stars) correspond to counter-rotating circular SOPs (S_3=0.999, J_3=-1). The X shape is obtained by inversing the sign of both S_3 and J_3 components at the input. The dashed-lines indicates the theoretical shape of this spatial PDW obtained from [72].

The second case illustrated in Fig. 1b, corresponds to the spatial PDW soliton predicted in ref. [72]. Here the injected conditions correspond to equal power counter-rotating circular SOPs (S_3=1 and J_3=-1+δ or S_3=-1 and J_3=1- δ, black stars). Similarly to the previous case, because of the nonlinear interaction between the two counter-propagating waves, the system tries to reach a stationary regime which must satisfy the co-rotating condition (S_3=J_3 to avoid nonreciprocity) while being locked at the edges by the boundary conditions. Consequently, the system spontaneously breaks the symmetry of the fiber and creates two orthogonal domains of polarization satisfying the co-rotating condition and linked by a polarization domain wall centered on L/2, along which the SOP of the waves are subsequently circular, elliptical and linear in the center. The fiber is then split in two regions of space with opposite handedness, in perfect analogy with polarization domain walls encountered in ferromagnetic materials which separate the regions of space characterized by opposite spins [82-84]. This soliton represents in fact a minimum of the Hamiltonian of the system and is found to be highly robust due to its topological nature if the length of the fiber is sufficiently long to be considered as semi-infinite [85-86]. This solution is a kink-like wave and takes the form of a *tanh* here given by $tanh\left(2\gamma S_0/\sqrt{3}\,(z-L/2)\right)$ and represented with dashed-lines in Fig. 1b [72, 74]. It is important to note that this spatial polarization domain wall is completely different from its temporal

counterpart [87-89]. Here this spatial soliton is a standing-wave solution, it corresponds to a distribution of the Stokes parameters inside the medium, which only depends on the propagation coordinate z and does not depend on time. On the opposite, the temporal PDW soliton is based on two co-propagating anti-correlated waves and originates from the compensation between chromatic dispersion and cross-phase modulation [87]. In contrast, in the present spatial case, the two waves are counter-propagating and the chromatic dispersion can be even neglected since both waves can be continuous (modulationnal instability is also supposed to be banned). Finally, it can be noticed in Fig. 1b that both counter-propagating waves nearly follow the same trajectory in opposite direction. Moreover, if the boundary conditions are flipped one another, the trajectory is also reverse, creating the X shape depicted in Fig. 1b.

These two fundamental examples depicted in Fig. 1 represent the basics of the polarization attraction process. For any case studied in this chapter, the system would be always understood by means of these two particular cases. As a general rule of thumb, we can conclude that the nonlinear interaction of two counter-propagating waves injected in an isotropic optical fiber, due to the mutual Kerr induced birefringence's, will always target a reciprocal co-rotating arrangement, while satisfying the boundary conditions imposed by the user.

This spontaneous relaxing behavior towards stable counter-propagating co-rotating SOPs can therefore be exploited to design a polarization attraction tool. This device was first introduced in the literature in 2001 by M. Haelterman and S. Pitois as a polarization funnel in a conference paper published in NonLinear Guided Waves and their applications taking place in Stresa [43].

Figures 2 illustrates its main mechanism. Fig. 2a displays the superposition of the stationary states, obtained from the numerical resolution of Eqs. (2), and resulting from the injection of a forward beam with different input S_3 values ranging from -1 to 1, while the counter-propagating "pump wave" is characterized by a fixed ellipticity, which therefore plays the role of polarization reference for the forward beam, here in J_3=0.

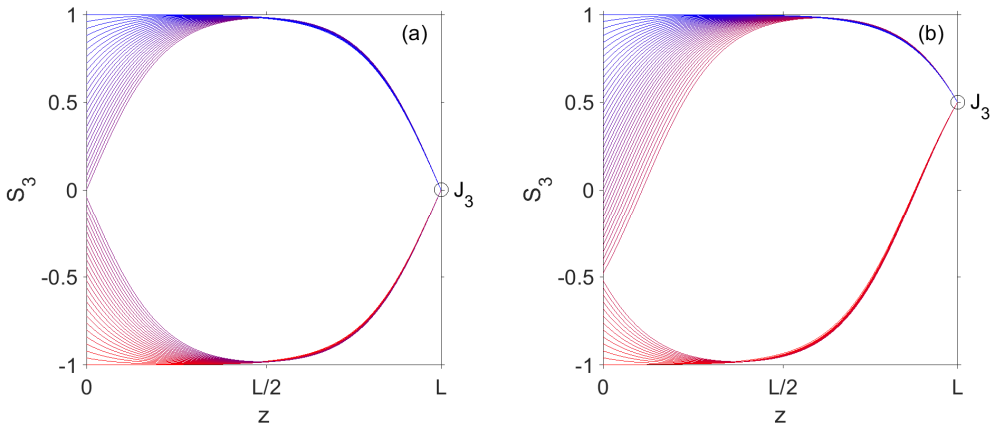

Fig. 2. Polarization funnel, L=4 (a) Stationary regimes obtained for different input conditions of $S_3(0)$ and for a backward wave ellipticity fixed at $J_3(L)$ =0 (black circle). (b) Same as (a) but for a backward wave ellipticity fixed at $J_3(L)$ =0.5.

It can be then clearly observed that all the trajectories of the forward wave, whatever its input ellipticity, converge to a single output point, corresponding to the backward input condition J_3=0, thus creating a lossless polarization funnel. This polarization attraction process is the direct consequence of the spontaneous symmetry breaking phenomenon described above. Indeed, for any input value of S_3, the system will relax towards a reciprocal equilibrium state targeting the co-rotating circular SOPs arrangement corresponding to S_3=J_3=±1, while satisfying the imposed output boundary conditions. Therefore, when the sum in inputs $S_3(0)$+$J_3(L)$ is positive, the system relaxes towards the co-rotating state S_3=J_3=1 and the forward beam

follows one of the upper trajectories. In contrast, when S_3+J_3 in input is negative, the system will relax towards the co-rotating state $S_3=J_3=-1$ and the forward beam will follow one of the lower trajectories. This properties can be well illustrated by repeating the previous simulations for a backward pump wave polarized with an ellipticity $J_3=0.5$ (Fig. 2b). We can observe that, depending on the initial value of S_3, the polarization of the waves follows a different path passing by either $S_3=1$ or $S_3=-1$, according to the sign of $S_3(0)+J_3(L)$.

In order to go further into the analysis, we have then study the whole dynamics of the three Stokes parameters during the polarization attraction process towards the north pole of the Poincaré sphere ($S_3(L)=1$). Since the dynamics is here mainly ruled by the co-rotating circular SOPs, in fact the two other Stokes parameters (S_1 and S_2) just follow the shortest path to reach this particular attraction point. Figure 3 illustrates the results of the numerical simulations obtained when a fixed counter-propagating pump wave J is injected with a fixed right-handed circular SOP ($J_1(L)=0$, $J_2(L)=0$ and $J_3(L)=1$) while the forward S signal SOP covers the entire Poincaré sphere (Fig. 3a).

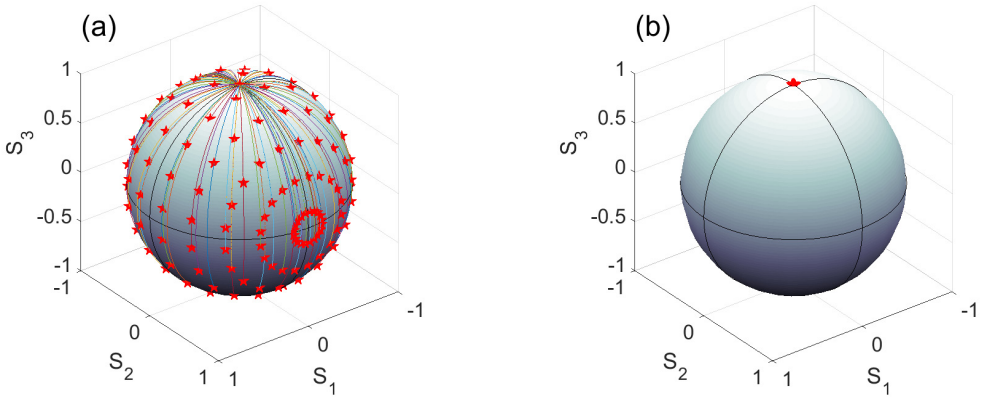

Fig. 3. SOPs at the input (a) and output (b) of the isotropic polarization funnel represented on a Poincaré sphere. The counter-propagating pump wave is fixed to $J_1(L)=0$, $J_2(L)=0$ and $J_3(L)=1$, while the input conditions are well distributed on the Poincaré sphere (Fig. 1a). In (a), the color solid lines indicate the spatial trajectories followed by the different input conditions to reach the attraction point.

We can observe in output of the system (Fig. 3b), that all the points well converge to the right circular SOP fixed by the counter-propagating pump wave, in good agreement with the theoretical description above. Moreover, we have plotted in Fig. 3a, with multi-color solid lines, the different trajectories followed by each of the forward input conditions. It is clear from this figure that the stationary regime corresponds to the shortest path which allows for any input condition to target the output SOP imposed by the counter-propagating wave in z=L. The only restriction, in absence of noise, is to avoid the input conditions corresponding to the exact opposite ellipticity of the backward pump wave, here for instance, $S_3(0)=-1$.

III. Principle of operation of the Omnipolarizer

The Omnipolarizer constitutes a particular arrangement of the polarization attraction system described above. Basically, a reflective element is placed at the output of the fibre in order to replace the external pump wave by a backward replica of the signal. Before describing theoretically in details the dynamics of the Omnipolarizer, let's first introduce the principle of operation in Fig. 4 based on experimental consideration. The device consists in a segment of optical fiber encapsulated in between an input optical circulator (to inject the incident signal and clear out its backward replica) and a partially reflective element at the opposite end (to generate the backward replica and collect the output signal). This reflecting component can be made of a fiber Bragg grating, metal or dielectric coating, or consists in an amplified reflective fiber loop so as to adjust the its reflective coefficient. In this configuration, to achieve an efficient

self-induced repolarization process, the arbitrary polarized incident signal has to nonlinearly interact with its backward replica [61]. Consequently, to generate an efficient cross-polarization effect along the entire fiber length, both counter-propagating beams have to propagate along at least some few nonlinear lengths (typically 5 L_{nl}) [82]. Therefore, in a typical configuration involving a 5-km long standard optical fiber with a Kerr coefficient $\gamma \approx 2$ W^{-1}.km^{-1}, a relatively high level of average power close to 500 mW is then necessary.

Secondly, the Omnipolarizer can be characterized by its reflection coefficient ρ, which is defined as the ratio of power between backward and forward signals. Depending on the value of ρ, which has to be above 0.8 for an efficient interaction and can be even larger than 1 for specific purposes, three main operating regimes have been identified.

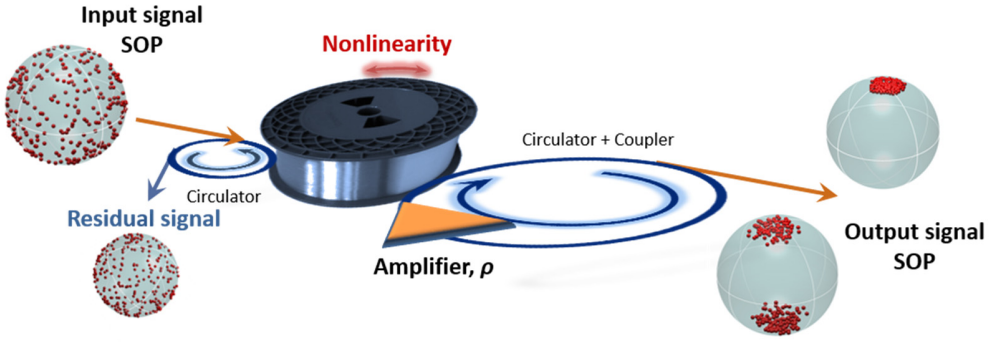

Fig. 4. Principle of operation of the Omnipolarizer.

The first operating regime is the *bistable* regime, and is reached for a reflection coefficient below unity, typically $0.8 \leq \rho \leq 1$. Basically, it corresponds to a simple reflection at the fiber end, and thus can be also achieved by means of a mirror, a FBG, a special coating or an amplified reflective fiber loop with a moderate amplifier gain. In this regime, for any arbitrarily polarized input signal, two opposite poles of attraction for the output SOP can be identified on the Poincaré sphere (see Fig. 4). In practice, the sign of the input signal ellipticity defines which of the two SOPs is obtained in the output. Consequently, for an initially depolarized signal, i.e., quickly scrambled in time all over the Poincaré sphere, the output signal SOP distribution will be highly localized around both poles of the sphere at the fiber output, corresponding theoretically to the right- and left-handed circular states (Fig. 4) [61]. In the second operating regime, the backward signal is amplified in such a way to achieve a reflective coefficient in the range of $1.2 \leq \rho \leq 2$. In this case, one of the two steady states becomes unstable and any arbitrarily polarized input signal is attracted towards a single output SOP, whose position over the Poincaré sphere can be controlled by means of the polarization rotation R imposed by the feedback loop (practically by means of a classical polarization controller implemented into the reflective loop) [59-60]. Given that any input SOP vector over the Poincaré sphere is aligned to a unique SOP vector at the device output, we define this functionality as the *alignment* regime. Finally, for larger reflection coefficients, i.e., $\rho >> 1$, a chaotic dynamics can be reached, leading to an all-optical scrambling of the output polarization [62-68]. Roughly speaking, this third regime is the opposite of the first two. Indeed in this case an initially fully polarized signal turns out to be completely depolarized in output, which corresponds to a *scrambling* regime. This chaotic behavior can be even more magnified through the implementation of a fiber delay into the feedback loop (typically larger than the L_{nl}), which can lead to practical applications in chaotic secure communications or random number generation [63].

IV. THEORETICAL DESCRIPTION

A. Isotropic fiber

In this section, based on the first theoretical part, we introduce numerically the different regimes of the spatiotemporal dynamics occurring in the Omnipolarizer and illustrated above in Fig. 4. As introduced so far, we indicate with $S=[S_1,S_2,S_3]$ and $J=[J_1,J_2,J_3]$ the Stokes vectors associated with the forward and backward beams, respectively. As in the previous section, the spatiotemporal dynamics of S and J in the fiber can be modelled by the system of Eqs. (2). However, in huge contrast with the previous section dealing with an external pumping, here the boundary conditions at the fiber end will read as $J(z=L,t)=\rho RS(z=L,t)$, and allows to univocally determine S(z,t) and J(z,t) once the input fields S(z=0,t) and J(z=0,t) are known. In its simplest form, ($\rho=1$, R=unity), similarly to the case of the first theoretical section, once an incident arbitrary polarized wave enters the system, the field S and its backward replica J spontaneously targets a nonlinear reciprocal stationary state characterized by co-rotating circular SOPs [76-78]. Since J(z=L,t=0) is initially not defined and remains a free variable, the system rapidly self-converges in z=L to either the right- or left circular state. This phenomenon of self-repolarization can be simply understood by placing a mirror in z=L/2 in the stationary states of Fig. 2a. Fig. 5a confirms this picture and shows the stationary regimes obtained from the numerical resolution of Eqs. (2), and resulting from the injection of an incident signal S with different values of ellipticity ranging from -1 to 1, while the counter-propagating wave J is characterized by J(z=L,t)=S(z=L,t), here the normalized length is fixed to L=4. It can be clearly observed that all the trajectories, whatever the input ellipticity, spontaneously converge to an equilibrium defined by co-rotating SOPs in z=L ($S_3(z=L,t)=J_3(z=L,t)=\pm1$), leading to a digitalization of the input ellipticity called bistable regime of the Omnipolarizer. In this particular regime, the system converges to the upper stationary trajectories as soon as S_3 is slightly positive and at the opposite, reaches ($S_3=J_3=-1$) as soon as S_3 becomes negative. At the end of the day, since the system is perfectly symmetrical, S_3 and J_3 follow the same path in opposite directions, illustrated in Fig. 5a by two examples of trajectories, marked with circles for J_3.

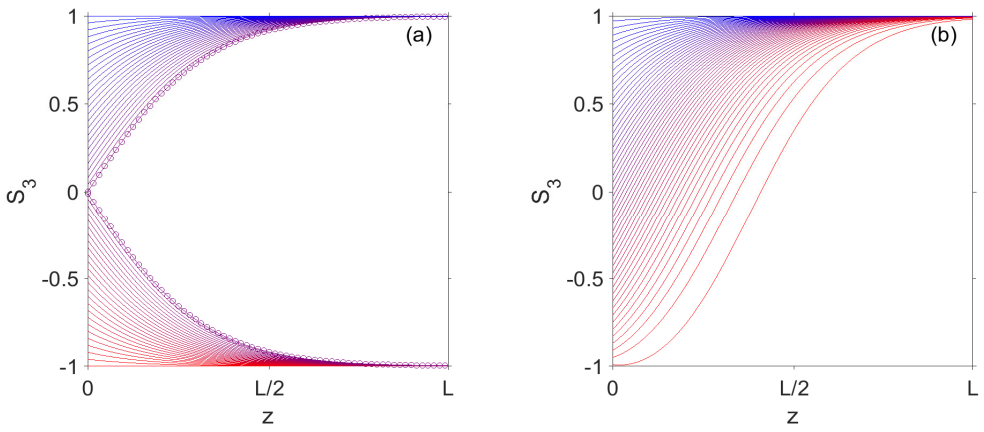

Fig. 5. (a) Bistable regime of the Omnipolarizer. Stationary regimes of the forward wave ellipticity S_3 obtained for different input conditions of $S_3(0)$ and for a boundary condition given by J(z=L,t)=S(z=L,t) and L=4. The circles correspond to two examples of the backward wave ellipticity J_3 (b) Alignment regime of the Omnipolarizer. Stationary regimes of the forward wave ellipticity S_3 obtained for different input conditions of $S_3(0)$ and for a boundary condition given by $J(z=L,t)=\rho RS(z=L,t)$. $\rho=1.2$ and R is a $\pi/4$ rotation around the S_3 axis.

In order to reach the alignment regime of the Omnipolarizer, one has to break the symmetry of the system. This action can be carried out by imposing a boundary condition defined by $J(z=L,t)=\rho RS(z=L,t)$, for which ρ and R correspond to the gain and rotation matrix of the reflective element and are chosen differently from unity. In this case, the broken symmetry leads to a single point of polarization attraction illustrated in Fig.

5b for a reflective coefficient ρ=1.2 and a rotation around the S_3 axis of $\pi/4$. As can be seen, whatever the initial ellipticity at the input of the system, all the stationary regimes converge to $S_3(L,t)=+1$. This broken symmetry effect can be understood by the fact that the rotation θ around the S_3 axis associated to the gain ρ force the SOPs initially localized in the wrong hemisphere, to be pushed in opposite direction of its closest natural attractor in such a way to reach the reverse pole of the sphere in an helical trajectory. Indeed, the derivative of S_3 in z=L is then proportional to $\sin(\theta)$, which pulls the output SOP towards the north pole if $\theta > 0$ or to the south pole if $\theta < 0$. Two examples are shown in the following figures illustrating the evolution of the output SOP as a function of time and reaching a stationary state. The starting point is depicted with a red circles, while the stationary state is highlighted with a red star. In Fig. 6a, it corresponds to a particular case used in Fig. 5b with $S_3(0)=-0.95$, ρ=1.2 and a rotation around the S_3 axis of $\pi/4$. The output SOP is then attracted to the north pole of the sphere $S_3(L)=+1$ following the red-line trajectory. In contrast, Fig. 6b displays the opposite case in which the attraction point is localized in the south pole of the sphere owing to a rotation around the S_3 axis of $-\pi/4$. For both cases, it can be clearly observed that the phenomenon is strong enough to pull the initial SOP at the opposite side of the sphere. Note that if an additional rotation is added in z=L along another axis of the sphere, then the point of attraction is simply shifted on the sphere.

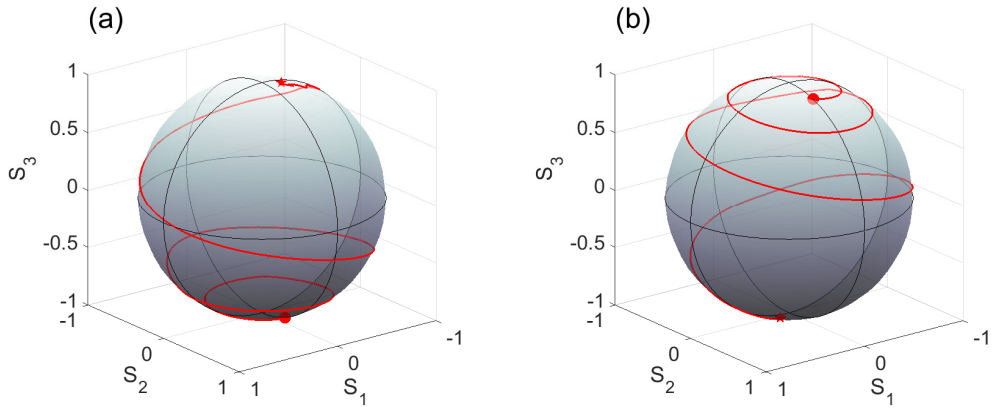

Fig. 6. Trajectories followed by an input SOP (red circles) and reaching a stationary regime (red stars) at the output of the Omnipolarizer in the alignment regime (a) $S_3(0)=-0.95$, ρ=1.2 and the rotation matrix R corresponds to a rotation around the S_3 axis of $\pi/4$ (b) Same as (a) with $S_3(0)=+0.95$, ρ=1.2 and R is a $-\pi/4$ rotation around the S_3 axis.

The dynamics of the Omnipolarizer is closely related to the stability of the stationary solutions of Eqs. (2), which are found by dropping the time derivatives. When the powers of the forward and backward beams can be considered as similar, which is the case for the bistable and alignment regimes, only the stable stationary SOPs can play the role of polarization attractors for the output forward and backward signals. As mentioned previously, they correspond to the simplest path shared by both counter-propagating waves to reach a reciprocal nonlinear birefringent regime. Consequently, these stable solutions are characterized by a non-oscillatory behavior along the fiber length, while unstable states are oscillating [50]. More generally, even for telecom fibers with random birefringence, it was found numerically that a stationary state of the system is stable only if its spatial period of oscillations is lower than the quarter of the fiber length [47-48]. This stability behavior is illustrated here in Fig. 7a. If we numerically solve Eqs. (2) into the alignment regime of the Omnipolarizer (ρ=1.2, R: $\pi/4$ rotation around S_3) and by using an initial stable-stationary state (red solid line) as input longitudinal field, then this state is preserved in time due to stability. Even if the input longitudinal field is now slightly perturbed by some additional noise (cyan solid line), then the stable stationary state plays the role of attractor which “cancels” the noise component, so that the field relaxes again towards the original stable state (red solid line). In contrast, if an ansatz of stationary state characterized by several spatial periods along the fiber length is now used as input longitudinal field (see

Fig. 7a, blue solid line) then it has been found to be unstable. Indeed, this stationary state cannot be preserved in time: the system gradually leaves this state and converges towards the only stable stationary state with a non-oscillatory behavior (again the red solid line).

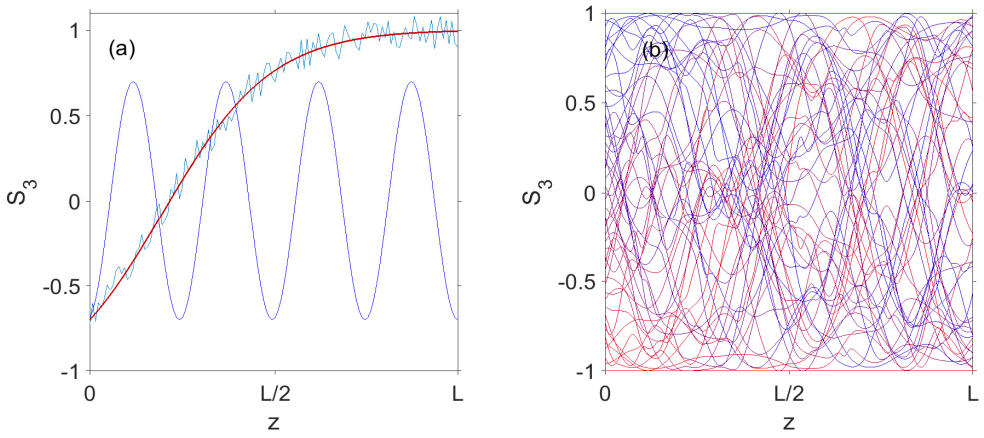

Fig. 7. (a) Stability of the stationary state in the attraction regime of the Omnipolarizer, ρ=1.2 and R is a π/4 rotation around the S_3 axis and L=4. Two different input stationary states are tested: one corresponding to a cos-like ansatz solution (blue solid line) and the second one corresponding to the stationary state solution with presence of an additional white noise (cyan solid line). Both of the input conditions converge to the stationary state solution plotted with red solid line (b) Chaotic regime of the Omnipolarizer. Forward wave ellipticity S_3 obtained for different input conditions of $S_3(0)$ ranging from -1 to 1 and for a boundary condition given by J(z=L,t)=ρS(z=L,t) with ρ=10 and L=2. None stationary regime is achieved, the output SOP is continuously scrambled.

In order to break the stability of the system, one has to make the system non reciprocal. It was even already highlighted in the 80's by Gaeta and coworkers in ref. [78]. The main idea is to impose a different amount of nonlinear birefringence on both counter-propagating waves in such a way that none stable stationary regime can be established within the Omnipolarizer because of the non-reciprocal criterion. This regime can be obtained by imposing a high difference of power in-between the two counter-propagating replicas, i.e. for high values of the reflective coefficient (ρ>>1). The co-rotating stable SOPs cannot be reached anymore and thus the output SOP fluctuates continuously in time leading to the chaotic regime of the Omnipolarizer. Fig. 7b displays typical results of numerical simulations in the chaotic regime. The incident signal S is characterized by different values of ellipticity ranging from -1 to 1, while the counter-propagating wave J is defined by the boundary condition of the Omnipolarizer J(z=L,t)=10S(z=L,t). We can then observed that none stationary regime is achieved and that the output SOP fluctuates in a random manner. This chaotic regime can then be exploited for polarization scrambling applications and random bit generation [63].

To conclude this part, we have summarized in the following figure the 3 main regimes of the Omnipolarizer by numerically solving the system of Eqs. (2) for a fiber length equal to 6. Figure 8a shows the distribution of input SOPs used to illustrate the bistable and alignment regimes of the Omnipolarizer. As can be seen, the incident SOPs cover the entire Poincaré sphere. Figure 8b displays the output SOPs obtained in the bistable regime of the Omnipolarizer. To this aim, the boundary conditions imposed to Eqs (2) read ρ=1, R= unity. In output of the device, we then observe that the system relaxes to either the north or south pole of the sphere corresponding to the right- or left-handed circular states, depending only on the sign of the input ellipticity. In contrast, in the alignment regime, displayed in Fig. 8c and obtained for ρ=1.2 and R: π/4 rotation around S_3, the system breaks its symmetry and only one pool of attraction remains, leading to a single pool of attraction on the Poincaré sphere. Finally, for a large reflective coefficient, here ρ=10, the system is unable to satisfy the reciprocal criterion and none stationary states can be achieved. Consequently, the output SOP drifts on the Poincaré sphere in a random motion (Fig. 8e).

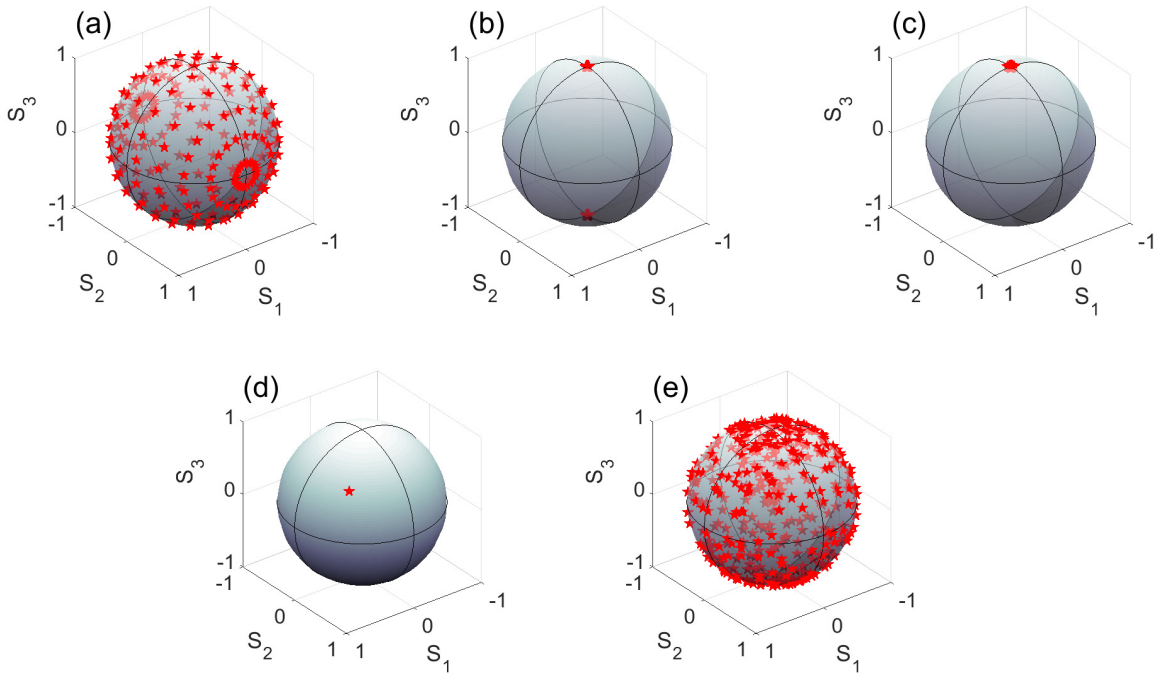

Fig. 8. SOPs at the input (a, d) and output (b,c,e) of the isotropic Omnipolarizer represented on the Poincaré sphere, here L=6. (b) Bistable regime ρ=1 and R is unity (c) Alignment regime, ρ=1.2 and R is a $\pi/4$ rotation around the S_3 axis (e) Scrambling regime ρ=10, L=2.

B. Randomly birefringent telecom fiber

So far in this report, all the theoretical/numerical description of the attraction process was performed in the case of an isotropic Kerr medium modeled by means of Eqs. (2). If the physical approach remains valid in order to describe the phenomenology of the Omnipolarizer, the model can be refined so as to take into account for km-long randomly birefringent telecom fibers often involved in the following experimental demonstrations. Following a similar averaging treatment of the random birefringent along the fiber length introduced by Wai in Menyuk for the celebrated Manakov system [14], Kozlov, Wabnitz and coworkers derive the equivalent vectorial Stokes system for counter-propagating waves interacting into a randomly birefringent fiber leading to the following coupled nonlinear partial differential equations [46]:

$$\begin{cases} c^{-1}\partial_t S + \partial_z S = S \times DJ \\ c^{-1}\partial_t J - \partial_z J = J \times DS \end{cases} \tag{3}$$

where D=8/9γ diag(-1,-1,1) is a diagonal matrix [46]. This system of equations is only valid if the length of the fiber L is much larger that the intrinsic beat-length and correlation length of the SOP fluctuations (typically L>>100m). Despite its simplicity, Eqs. (3) capture all the essential properties of the polarization dynamics involved within the telecom-fiber based Omnipolarizer, which is highlighted by the good qualitative agreement with experimental results discussed in the next sections. In fact, compared to the isotropic model described above in Eqs. (2), we can observe that the self-induced birefringence term vanishes. Indeed, all the polarization basis contribute with the same weight to the self-induced birefringence term. More importantly, the stationary system (by dropping the time derivative) is here characterized by three conservative quantities (instead of only one for the isotropic case), defined by the vector K=S-DJ: $K_1=S_1(z)+J_1(z)$, $K_2=S_2(z)+J_2(z)$ and $K_3=S_3(z)-J_3(z)$ (K_3=0 in the case of the Omnipolarizer because of the

boundary conditions imposed at the mirror $S_3(L)=J_3(L)$). Despite these new properties and changes in the matrix *D*, the general features described above for the isotropic case remain still valid for this randomly birefringent system. Both waves will relax towards the reciprocal stationary state characterized by co-rotating SOPs. It is even more intuitive in that case, since the stationary states are characterized along z by the three constant coordinates of the vector K, each corresponding to a Stokes parameter. Indeed, we can notice that S_1 and J_1 (as well as S_2 and J_2) follow opposite trajectories and thus can mutually compensate for their nonlinear birefringence contributions, while S_3 and J_3 relax to the same co-rotating ellipticity ($K_3=0$). Finally, thanks to these additional constants of motion, the stationary system of the randomly birefringent fiber is qualified as super-integrable (more constant quantities than degrees of freedom), which provides interesting mathematical properties [50-51]. Among them, spatio-temporal steady-state solutions of the system take the form of cosine and sine standing waves of period $2\pi/|K|$, which can play the role of polarization attractor [70]. Nevertheless, we have to notice that these solutions can only be derived once the system has relaxed to its stationary regime, since K has to be evaluated from S and J at the same fiber location z. Figure 9 illustrates the case of the randomly birefringent fiber with L=4. Figures 9(a-c) display the evolution of the three Stokes parameters obtained in a single numerical realization in the bistable case (ρ=1). Starting from an initial condition S=(0,-1,-0.15) at the input of the fiber, we can see that the system self-organizes the output SOP in z=L close to the left-handed circular SOP (S_3=-1). As expected, the system is characterized by three constants of motion, K_1, K_2 and K_3, depicted here with green dashed lines in subplots (a-c), which lead to opposite trajectories for S_1 (J_1), (Fig. 9a), and S_2 (J_2), (Fig. 9b), along the fiber length, while S_3 and J_3 follow the same ellipticity variations ($K_3=0$) (Fig. 9c). Moreover, we can observe that the analytical expressions derived in ref. [70] for the stationary state trajectories along the propagation distance (black circles) well follow the numerical simulation results.

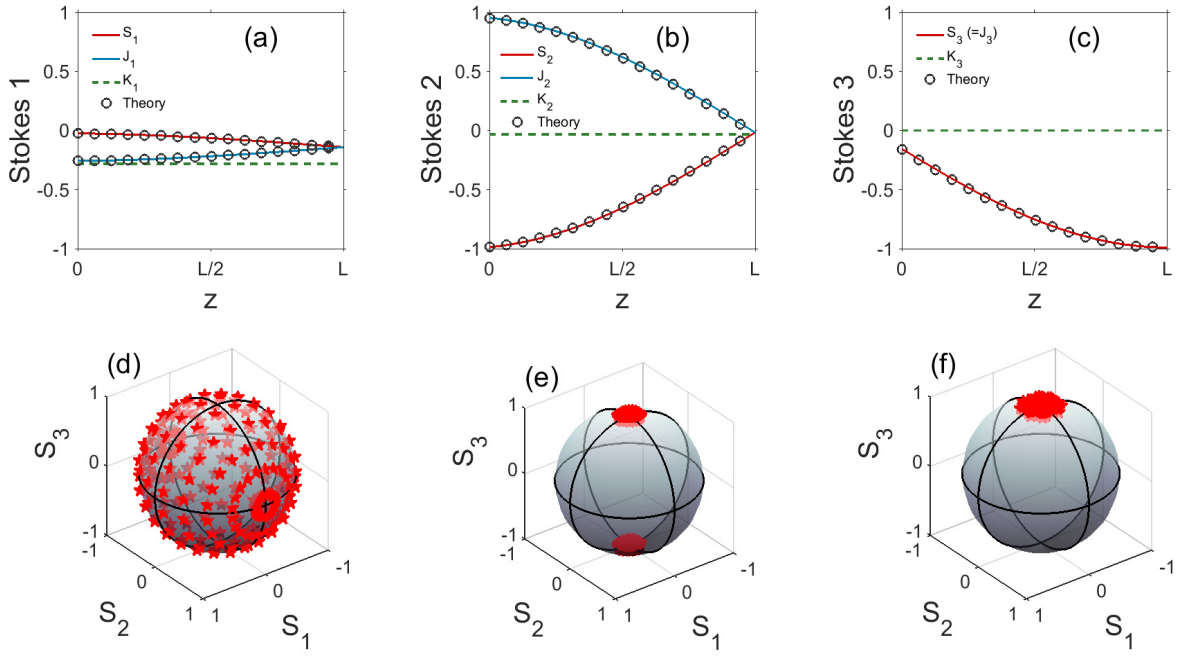

Fig. 9. Randomly birefringent Omnipolarizer (L=4). (a-c) Single numerical simulation results. The three Stokes parameters for counter-propagating waves S and J in their stationary regimes are depicted along the fiber length with red and blue solid lines. The green dashed line show the associated K vector, while dark open circles depict the analytical expressions derived from Ref. [70]. (d) SOPs at the input and output (e, f) of the Omnipolarizer represented on the Poincaré sphere. (e) Bistable regime ρ=1 and R is unity (f) Alignment regime, ρ=1.2 and R is a $\pi/4$ rotation around the S_3 axis.

Finally, Figs. 9(d-f) display the input (Fig. 9d) and output Poincaré spheres obtained in the case of the randomly birefringent Omnipolarizer with L=4 for the bistable regime (Fig. 9e) and for the alignment regime (Fig. 9f, ρ=1.2 and R: $\pi/4$ rotation around S_3). Similarly to the previous isotropic case, the output SOP of the incident signal is well attracted to either the north or south pole of the sphere. However, we can notice that the area of the resulting pool of attraction is larger than in the previous study. This behavior is attributed to the lower cross-polarization efficiency resulting from the Manakov model (twice below the isotropic case). A longer fiber (larger input power) is thus required to better converge towards a single attraction point.

V. EXPERIMENTAL OBSERVATION OF THE SELF-POLARIZATION PROCESS

A. Experimental setup

Figure 10 depicts the experimental setup implemented in order to characterize the first two operating regimes of the Omnipolarizer described above in the context of a 40-Gbit/s OOK Return-to-Zero (RZ) transmission. An initial 40-Gbit/s RZ signal is first generated thanks to 10-GHz mode-locked fiber laser delivering 2.5-ps pulses at 1562.4 nm. The pulses are then reshaped into 7.5-ps Gaussian pulses by means of a programmable optical bandpass filter (Waveshaper). The resulting 10-GHz pulse train is then encoded by means of a LiNbO3 intensity modulator driven by a 2^{31}-1 pseudo-random bit sequence (PRBS) and finally multiplexed in the time domain so as to achieve a total bit rate of 40-Gbit/s. A commercial polarization scrambler is used to introduce strong polarization fluctuations at the input of the Omnipolarizer with a rate of 0.625 kHz. Before injection into the device, the 40-Gbit/s signal is amplified thanks to an Erbium doped fiber amplifier (EDFA) to an average power of 27 dBm, leading to a normalized fiber length close to L=5.

The Omnipolarizer is made of a 6.2-km long Non-Zero Dispersion-Shifted Fiber (NZDSF) characterized by a normal chromatic dispersion D = -1.5 ps/nm/km at 1550 nm, a Kerr coefficient γ=1.7 $W^{-1}.km^{-1}$ and a polarization mode dispersion (PMD) coefficient of 0.05 $ps/km^{1/2}$. An optical circulator is inserted at the input of the fiber in order to inject the incident signal as well as to extract the residual counter-propagating replica through its port #3. At the opposite end of the fiber, the feedback loop consists in a second circulator, a 90:10 coupler and a second EDFA whose gain enables us to directly adjust the reflection coefficient ρ. Note that a polarization controller is also inserted into the loop and corresponds to the rotation matrix R introduced in the theoretical sections.

After polarization processing, the resulting 40-Gbit/s signal was optically filtered by means of a 70-GHz Gaussian shape optical bandpass filter shifted by 170 GHz from the initial signal frequency, in order to reshape the output signal and improve its extinction ratio, just like the well-known Mamyshev regenerator [87-93]. At the receiver, the SOP of the output signal is characterized on the Poincaré sphere by means of a commercially available polarimeter. The residual polarization fluctuations as well as the intensity profile degradations are also characterized in the temporal domain by monitoring the corresponding eye-diagram beyond an inline polarizer or a polarization beam splitter (PBS). Finally, the data are detected by means of a 70-GHz photodiode and electrically demultiplexed into the time domain to four 10-Gbit/s tributary channels to perform bit-error-rate (BER) measurements.

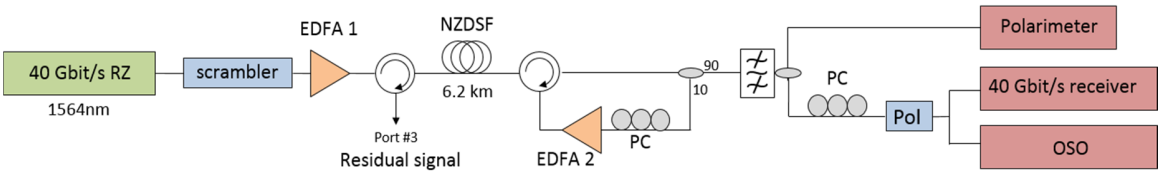

Fig. 10. Experimental setup of the Omnipolarizer: polarizer (Pol), Erbium doped fiber amplifier (EDFA), non-zero dispersion fiber (NZDSF), polarization controller (PC), Optical sampling oscilloscope (OSO).

B. Polarization segregation of a 40-Gbit/s signal

The efficiency of the polarization attraction process provided by the Omnipolarizer was first characterized in the polarization domain. Figure 11a displays on the Poincaré sphere the different incident SOPs of the 40-Gbit/s signal recorded at the input of the device. Because of the initial polarization scrambling, the signal SOP distribution well covers the entire sphere. This arbitrarily polarized signal is then injected into the Omnipolarizer with an average power of 27 dBm. Figure 11b&c show the evolution of the SOP characterized at the output of the system. In a first step (Fig. 11b), the back-reflected power is adjusted to an average power of 25 dBm by means of the EDFA 2, corresponding to a reflective coefficient ρ=0.8. In this case, and in pretty good agreement with the previous numerical results of Fig. 9e, the Omnipolarizer enters into the bistable regime and the output SOP of the 40-Gbit/s signal converges to two different orthogonal SOPs, here adjusted on both poles of the sphere thanks to the polarization controller of the reflected loop. In this regime, the Omnipolarizer clearly acts as an ideal polarization beam splitter. Indeed, depending only on the sign of its initial ellipticity, all the energy of the incident signal is routed to either the north or south pole of the sphere. It is noteworthy that these two output SOPs are independent of any environmental changes or stress induced on the fiber. Indeed, we have checked that straining the fiber does not influence the position and width of the output SOP distribution.

Next, increasing further the backward power to 28 dBm (ρ=1.2) forces the Omnipolarizer to switch to the second regime of polarization attraction. In this regime, one of the previous two poles of attraction becomes unstable, and the device acts as an ideal nonlinear polarizer. All the input polarization fluctuations are canceled and consequently, all the output SOPs remain trapped around a small area of the sphere, as shown by Fig. 11c and in fair agreement with numerical results of Fig. 9f. Note that the selection of one or the other poles of attraction is only determined by the angle of polarization rotation in the reflective loop, and thus can be selected by means of the polarization controller. As mentioned above, such rotation around the S_3 axis, is at the origin of the spontaneous imbalance phenomenon occurring between the two stable spots of attraction [50].

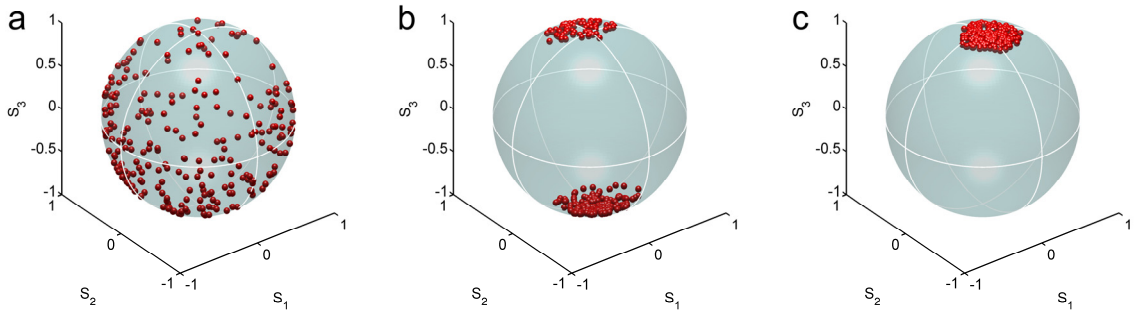

Fig. 11. (a) Poincaré sphere of the 40-Gbit/s signal at the input of the device (b) Poincaré sphere recorded at the output of the Omnipolarizer in the bistable regime (ρ=0.8) for an input power of 27 dBm (L=5) (c) Poincaré sphere recorded at the output of the Omnipolarizer in the attraction regime (ρ=1.2)

Finally, Fig. 12 summarizes the experimental evolution of the output DOP as a function of the reflective coefficient ρ of the Omnipolarizer for an input power of 27 dBm. The DOP is classically defined as followed:

$$\mathrm{DOP} = \frac{\sqrt{\langle S_1(t)\rangle^2 + \langle S_2(t)\rangle^2 + \langle S_3(t)\rangle^2}}{\langle S_0(t)\rangle} \quad (4)$$

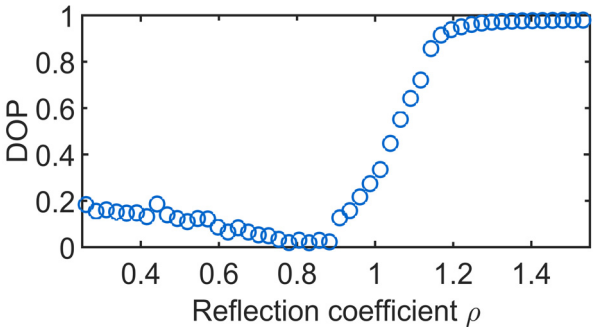

Fig. 12. Degree-of-polarization (DOP) recorded at the output of the Omnipolarizer as a function of the reflective coefficient ρ.

We can clearly observe the different working regimes of the device. Indeed, for $0.8 \leq \rho \leq 1$, the system operates in its bistable regime and thus its output DOP becomes close to zero because of the two opposite pools of attraction, despite the self-organization process. On the contrary, for $\rho \geq 1.2$, the device enters into its alignment regime and the DOP asymptotically reaches a value close to unity. The efficiency of this repolarization processing is even more impressive when monitored in the time domain. To this aim, we first display in Fig. 13a the eye-diagram of the 40-Gbit/s RZ signal recorded at the input of the Omnipolarizer and detected after an inline polarizer. Obviously, due to the initial polarization scrambling, all polarization fluctuations imposed by the scrambler are transferred into the time domain, thus inducing large intensity variations and a complete closure of the eye-diagram.

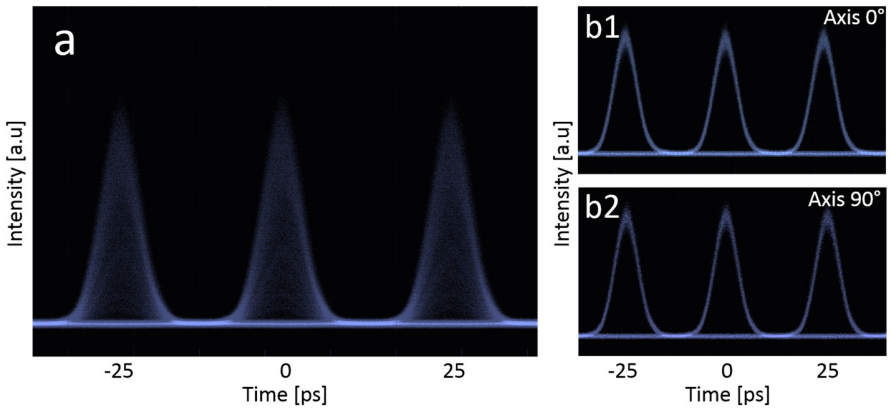

Fig. 13. (a) Eye-diagram of the 40-Gbit/s signal monitored behind an inline polarizer at the input of the device. (b1-b2) Eye-diagram of the 40-Gbit/s signal at the output of the Omnipolarizer in the bistable regime and monitored along both axes of a PBS.

In contrast, when the Erbium doped fiber amplifier of the reflective loop (EDFA 2) is turned on with ρ = 0.8, the Omnipolarizer first acts in its bistable regime, corresponding to the output Poincaré sphere of Fig. 11b. In this case, as highlighted by figures 13b1 & b2, no more intensity fluctuations can be observed in the output eye-diagrams of the 40-Gbit/s signal when detected behind the output PBS. Indeed, in this operating regime, the whole energy of the incident signal is routed in a binary manner to either one of the other axis of the output PBS depending only on the sign of its input ellipticity. The output eye-diagrams remain wide-open without any pulse splitting and with an extinction ratio above 20 dB between both axes, thus confirming the previous results observed in the Poincaré sphere of Fig. 11b.

This symmetry breaking behavior of the Omnipolarizer, leading to the switching of the output SOP among two orthogonal axes, can be also clearly observed in Fig. 14. In this figure, we have reported the

evolution of the 40-Gbit/s data stream at the output of the device recorded behind a PBS by means of a 1-GHz low bandwidth oscilloscope, in such a way to only monitor the polarization fluctuations. These results confirm that, despite the initial polarization scrambling imposed on the input signal at a rate of 0.625 kHz, the output SOP is characterized by a random binary nature, since it is routed to either one or the other axis of the PBS with a high extinction ratio. This process could be useful for instance to develop an all-optical random bit generator [105] from a chaotic polarization device, as well as a polarization-based optical memory or a polarization switch [61].

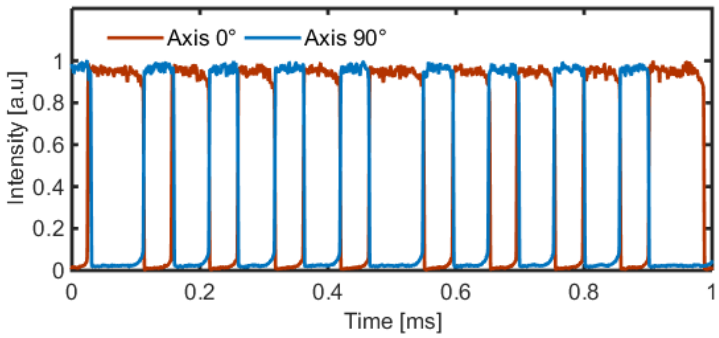

Fig. 14. Temporal evolution of the polarization state of the 40-Gbit/s signal recorded at the output of the Omnipolarizer in the bistable regime and monitored along both axes of a PBS thanks to a low-bandwidth oscilloscope.

C. Self-polarization alignment of a 40-Gbit/s signal

By increasing further the average power of the backward replica until 28 dBm, the Omnipolarizer switches from the bistable regime to the alignment regime, corresponding to the Poincaré sphere reported in Fig. 11c. As in the previous study, the eye-diagram of the 40-Gbit/s signal is then recorded at the output of the device after an inline polarizer in order to transfer the residual polarization fluctuations into amplitude noise. The resulting eye-diagram is depicted in Fig. 15a. Despite the input polarization scrambling, illustrated by the initial closed eye-diagram of Fig. 13a, here we can clearly monitor a well-open eye-diagram. Indeed, no more intensity fluctuations can be observed behind the polarizer, which confirms the efficiency of the self-induced repolarization process undergone by the signal within the Omnipolarizer.

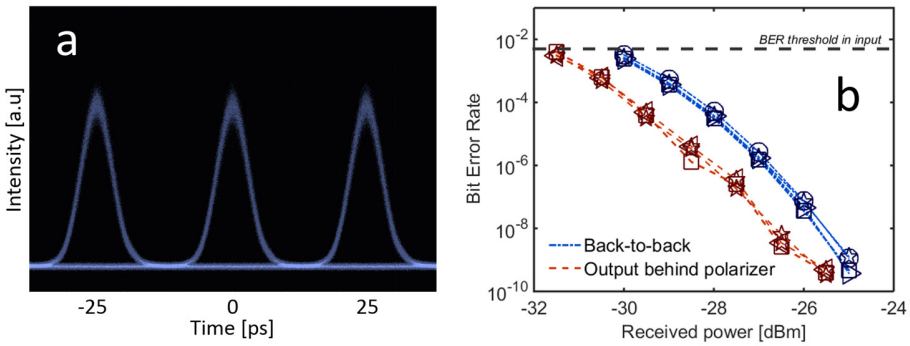

Fig. 15. (a) Eye-diagram of the 40-Gbit/s signal at the output of the Omnipolarizer in the attraction regime and monitored behind a polarizer (b) Corresponding BER measurements as a function of the received power for all the four 10-Gbit/s tributary channels demultiplexed from the 40-Gbit/s signal.

More importantly, as displayed in Fig. 15b, the corresponding BER measurements, performed after the output polarizer as a function of the incoming power on the receiver, show that the Omnipolarizer is able to maintain optimal performance of data-processing through any polarization-dependent optical component.

More precisely, whereas the input BER is limited to a threshold of 10^{-2} due to the initial scrambling process which closes the eye-diagram through the polarizer, the output signal is forced to align its SOP on the polarizer axes, thus enabling a complete recovery of the transmitted data with an error-free measurement for all the four 10-Gbit/s tributary channels demultiplexed from the 40-Gbits data stream.

It is also worth noting that the output BER is characterized by a 1-dB sensitivity improvement with respect to back-to-back measurements. This phenomenon is attributed to the pulse reshaping properties of the device. Indeed, to be efficient, the polarization attraction regime of the Omnipolarizer imposes a high level of average power close to 500 mW. Consequently, the optical pulses of the RZ 40-Gbit/s signal propagate within the NZDSF with a peak power close to 3 W (N~7), and thus undergo a large self-phase modulation (SPM) effect. The SPM leads to a wide spectral broadening, as illustrated in the optical spectrum of Fig. 16a (orange curve) recorded after the NZDSF, when compared with the input spectrum (blue curve). This SPM effect combined with the normal chromatic dispersion of the fiber induces a nonlinear reshaping of the pulses towards a parabolic shape first and then to a square shape, as shown in Fig. 16b with the eye-diagram recorded at the output of the NZDSF. In order to retrieve the initial shape of the propagating pulses and improve the extinction ratio, we thus carried out a 170-GHz Gaussian shape offset filtering (see output spectrum in Fig. 16a, red solid-line), which led us to obtain the eye-diagram of Fig. 15a, by using the principle of a Mamyshev regenerator [87-93]. Therefore, it is important to note that the strong nonlinear regime of propagation undergone in the Omnipolarizer can also be a limitation for practical implementations and high-bit-rate signals. Indeed, a careful design, in particular a proper choice of the fiber has to be done, especially for OOK signals, in order to avoid complex soliton dynamics in anomalous dispersive fibers, or wave breaking phenomena in the normal dispersion regime [82]. Note also that despite the strong nonlinear regime of propagation within the Omnipolarizer, the polarization attraction process is also compatible with phase shift keying formats, as demonstrated in ref. [56].

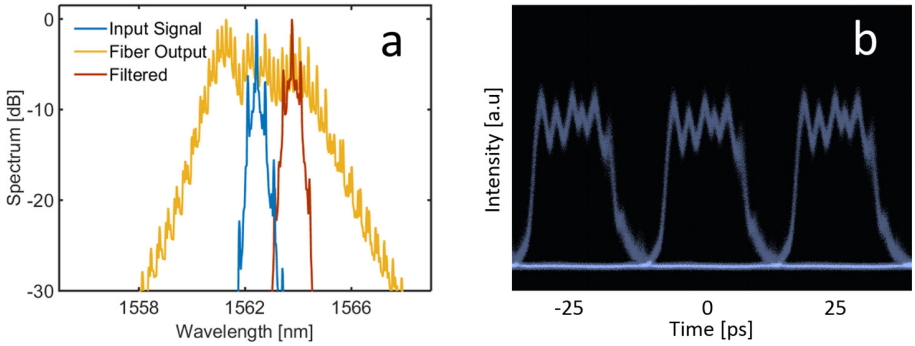

Fig. 16. (a) Optical spectra of the 40-Gbit/s signal measured at the input of the device (in blue), at the output of the NZDSF fiber (in orange) and after the offset filtering (red solid-line) (b) Eye-diagram of the 40-Gbit/s signal directly recorded at the output of the NZDSF fiber in the attraction regime (P=27 dBm) and monitored without filtering operation.

Following our encouraging results obtained for Telecom signals at bit rates up to 40 Gbit/s, we have decided to design and promote an integrated prototype. The resulting system is displayed in Fig. 17 and was funded in the context of a maturation program Synerjinov and Oseo (now Sayens). This device was designed on the basis of the experimental setup depicted in Fig. 10 and includes two high-power EDFA modules as well as an electronically addressed polarization controller implemented into the reflective loop. The whole device is then controlled through a user-friendly software based on a Labview environment. In parallel, a study market has been also performed by the Tematys consulting firm with the idea to find some potential industrial partners and start our own business. Promoting live demonstrations were also held at the international conference ECOC exhibition in 2010 in Turin, in Geneva 2011 and Amsterdam 2012. Unfortunately, no market, at least with a sufficient market size, has been identified to launch a potential

product. We attribute this unsuccessful story to the price of the prototype (>12k€) and to the similar performance of our main competitors [31-32]. Indeed, while commercially available optoelectronic polarization devices are able to tract the polarization state at a rate of several MHz, here we are clearly limited by the time response of the polarization attraction process, which is more or less related to the nonlinear time of the phenomenon c/L_{nl}, typically in the range of a few µs. Moreover, based on an optical fiber spool, its potential of integration is limited and its power consumption remains quite high (typically 50 W, mainly from 2 high power EDFAs). To overcome these crucial drawbacks, one way of research could be to develop an Omnipolarizer on an optical chip…

Fig. 17. Picture of the Omnipolarizer prototype.

VI. BISTABILITY: FLIP-FLOP MEMORY AND SWITCHING OPERATION

A. Principle and hysteresis cycle

In this section we go further into the physical understanding of the bistable behavior and associated hysteresis cycle already outlined in section III. We will also discuss the potential of proof-of-principle experiments for applications based on polarization bistability [61]. As already described, the stationary system associated to Eqs. (3) admits as a constant of motion the vector K = S-DJ. By insertion of DJ= S-K in the stationary system (taking the time derivative to zero) we then obtain $\partial_z S = K \times S$, whose solution are rotations around K corresponding to trajectories of spatial period $2\pi/|K|$ [59]. In the simplest form of the Omnipolarizer, $\rho \simeq 1$, R=diag(1,1,1), the component K_3 of K is null and therefore the system $\partial_z S = K \times S$ is symmetric with respect to rotations around the S_3 direction. This practically allows restricting the study to find the relation between the input ellipticity $S_3(z=0)$ and the output ellipticity $S_3(z=L)$ of the stationary states of Eq. (3). These curves are displayed in Fig. 18(a-b) for two different situations of injected power, namely the normalized fiber length.

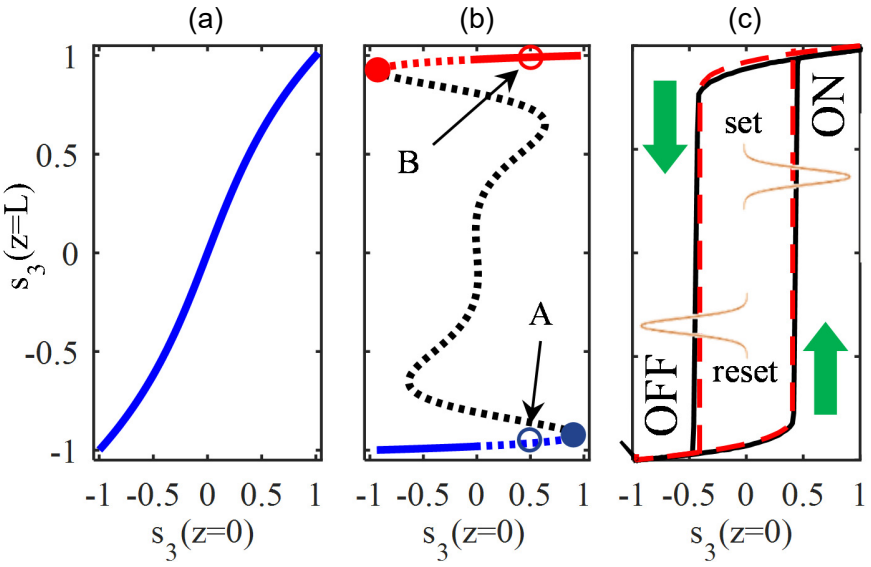

Fig. 18. (a): $S_3(z=L)$ versus $S_3(z=0)$ for the stationary solutions of Eqs.(3) in the simplest passive configuration ρ=1, R=unity, null losses and L=0.4. All points of the curve correspond to stable stationary solutions. (b): same as in (a) but when L=4. Solid blue and red lines correspond to the stable states such that $S_3(z=L)\simeq$-1 and $S_3(z=L)\simeq$+1, respectively. Dashed blue and red lines correspond to the metastable states. The black dashed line corresponds to the set of unstable states. The blue and red spots in $s_3(z=0)=\pm0.85$ identify the extremities of the line of unstable states. The empty circles A and B represent respectively the metastable and the stable states corresponding to $S_3(z=0)=0.5$. (c): Hysteresis cycle recorded experimentally at the output of the Omnipolarizer (black solid line) for L=4 and ρ=0.9. Numerical solutions of Eqs. (3) are also represented with red dashed-lines.

First-of-all, if the normalized fibre length is weak (Fig. 18a), the propagating regime is close to be linear. We then clearly get a quasi-straight line that corresponds to the limit $L\simeq0$, for which $S_3(z=L) \simeq S_3(z=0)$. In huge contrast, for stronger nonlinear regime, i.e. when L increases, the transfer function of the system becomes sharper and sharper until it exhibits a vertical tangent. Beyond this power, the curve becomes multivalued, as shown in Fig. 18b for L=4, so that for a given input $S_3(z=0)$ we may find several output values for $S_3(z=L)$, corresponding to a variety of stationary solutions $S_3(z)$ (not necessary stable) associated with $S_3(z=0)$. However, only one among these stationary solutions appears stable (here depicted with solid line in Fig. 18b). Indeed, if $-1\leq S_3(z=0) \leq 0$ then the lower-valued solution $S_3(z=L)$, represented by the blue solid line in Fig. 18b, is the only one related to a stationary state which fulfills the reciprocal nonlinear birefringence criterion and which is not oscillating along the fiber length, thus remaining stable [50]. At the opposite, if $0\leq S_3(z=0)\leq 1$ then only the higher-branch solution of $S_3(z=L)$, represented by the red solid line in Fig. 18b, is stable and can play the role of polarization attractor. Furthermore, it is clear from Fig. 18b that when L>>1 then the blue and red segments correspond respectively to $S_3(z=L)\simeq$-1 and $S_3(z=L)\simeq$+1. Therefore, as anticipated in the previous sections, in the highly nonlinear regime, the stable stationary states are such that $S_3(z=L) \simeq \text{sign}[S_3(z=0)]$ [59]. Consequently, in agreement with the previous results of Fig. 9b and 11b, if a constant-in-time input SOP S(z=0), localized in the north (south) hemisphere of the Poincaré sphere is injected into the Omnipolarizer, namely $S_3(z=0)>0$ ($S_3(z=0)<0$), then the corresponding output S(z=L,t) will relax towards the north (south) pole of the sphere, that is $S_3(z=L,t)\simeq+1$ ($S_3(z=L,t) \simeq$-1).

One may wonder what happens if the input S(z=0,t) is not constant but varies in time. On these above basis, one may wrongly deduce that if $S_3(z=0,t)$ moves from negative values to positive values (i.e. it changes sign) then the corresponding output $S_3(z=L,t)$ will suddenly jumps from -1 to +1 in $S_3(z=0,t)=0$. However, this is not completely true because another class of stationary solutions exists that are metastable, indicated by the blue and red dashed lines in Fig. 18b, and which can sustain the system into its current stable state. Roughly speaking, these metastable states are qualified as stable under "small" perturbations and can be adiabatically reached from the stable states. This means that if we "slowly" vary $S_3(z=0,t)$ from

-1 to +1, after having covered the blue solid line of stable states, we then enter into the blue dashed line region of metastable states which starts in correspondence of $S_3(z=0)=0$. Moving further, we find the first vertical tangent, which is indicated by the blue spot in Fig. 18b and that corresponds to the first unstable state at $S_3(z=0)=0.85$. It is beyond this point that the output $S_3(z=L,t)$ abruptly jumps towards the opposite branch of stable states, corresponding to the red solid line. This switching threshold strongly depends on how fast the input $S_3(z=0,t)$ varies: the more its transition from -1 to +1 is slow, the larger is the switching value, but in any case the upper limit is represented by the value corresponding to the first unstable state, which is $S_3(z=0)=0.85$ in the case under analysis. As an example, in Fig. 18b the switching value $S_3(z=0)=0.5$ makes the system to jump from the point A, which is close to -1 and is related to a metastable state, to the point B, which is close to +1 and corresponds to a stable stationary state. In a similar manner, the same behavior is observed when $S_3(z=0,t)$ moves from +1 to -1. In this case, after following the red solid line corresponding to stable states, the output SOP follows the red dashed line of metastable state and reaches the vertical tangent indicated by the red spot in $S_3(z=0,t)=-0.85$. Beyond this value, the output $S_3(z=L,t)$ is forced to suddenly jump towards the opposite branch of stable states, reaching the blue solid line.

These abrupt transitions between the upper and the lower branches, combined with the existence of a metastable class of stationary states are a clear signature of an hysteresis phenomenon. This behavior, here described in the ideal case of zero losses and unit reflection coefficient, is still observed for typical experimental propagation losses of 0.2 dB/km and for $0.8 \leq \rho \leq 1$. Figure 18c illustrates a complete hysteresis cycle obtained in experiments (black solid line) and numerically from Eqs. (3) (red dashed-line) when employing a 4-km long non-zero dispersion shifted fiber (NZ-DSF) characterized by a chromatic dispersion of -1.16 ps/nm/km, a Kerr coefficient $\gamma=1.7$ $W^{-1}km^{-1}$, propagation losses of 0.2 dB/km and a PMD coefficient of 0.05 $ps/km^{1/2}$. The reflective element is here a single fiber Bragg mirror (FBG 99% of reflection) which enables us to achieve a reflective coefficient $\rho \simeq 0.9$. The input signal consists in a 100-GHz polarized incoherent signal obtained from a filtered spontaneous noise emission Erbium source. This quite simple home-made, large bandwidth input signal allows us to avoid any Brillouin back scattering in the fiber undertest, thus preventing the implementation of strong phase modulation traditionally used for coherent CW signal. Subsequently, in order to monitor the hysteresis response of this Omnipolarizer, we have carefully controlled the SOP of the incident signal in such a way to follow an adiabatic transition making the input ellipticity $S_3(z=0,t)$ to vary from -1 to +1 and vice-versa with a ramping time of 200 ms thanks to an opto-electronic polarization controller. The input average power is 570 mW (27.5 dBm) and the corresponding nonlinear length is $L_{nl}=1.03$ km, so that $L \simeq 4$. In Fig. 18c, the switching of the output $S_3(z=L,t)$ between the two branches of the hysteresis when the input $S_3(z=0,t)$ reaches ± 0.4 is clearly visible. It is important to note that the output S_3 component maintains its value close to -1 (OFF state in Fig. 18c) or +1 (ON state) and that transitions are remarkably sharp, so that the hysteresis cycle appears well opened. As previously underlined, this is due to the presence of a strong nonlinearity ($L \simeq 4$). Note also the excellent agreement with numerical results, obtained by solution of Eqs. (3) including exact experimental parameters and fiber losses. Once again, these agreement confirms the full validity of Eqs. (3) for the description of the polarization dynamics in the Omnipolarizer.

An interesting application of this hysteresis cycle relies on the possibility to imprint or reset the ON or OFF state and to maintain this state even if the flipping cause has disappeared, in such a way to implement a polarization-based flip-flop memory [61]. The principle of operation can be inferred from Fig. 18c. For an input constant in time SOP centered on $S_3(z=0)=0$, a polarization spike introduced in the S_3 component is then injected into the fiber. The high value of ellipticity makes switch the S_3 component to the ON state close to +1. Afterwards, the set pulse vanishes to 0 but the system remains locked to the ON state because of its hysteresis properties. It is only by means of a reset pulse, which makes the output ellipticity to cross the switching point, that S_3 drops back to the OFF state and clear the memory. Finally, the system remains in this OFF condition until a next writing pulse is applied.

B. Experimental demonstration of a polarization based all-optical memory

Based on the above concept, Figs. 19(a-b) illustrates the experimental proof-of-principle observation of

a polarization-based flip-flop memory that is loaded (cleared) by a train of set (reset) pulses, respectively. The fiber and the average input power are those employed when reproducing the hysteresis cycle of Fig. 18c. Therefore, the peaks of the set and reset input pulses should be respectively larger than +0.4 and lower than -0.4 in order to induce the transition of the output S_3 from the OFF state to the ON state and vice-versa.

To this aim, a random sequence of set/reset input spikes $S_3(z=0,t)$ with a width of 2 ms, a rise time of 20 μs and ellipticity peaks of ± 0.7 was imprinted on the 100-GHz polarized incoherent wave by means of an opto-electronic polarization controller. This signal was then amplified to an average power of 570 mW. The S_3 input sequence as a function of time is depicted in Fig. 19a. When injected into the Omnipolarizer, this set/reset polarization spike sequence gives rise to the output evolution of the $S_3(z=L,t)$ parameter displayed in Fig. 19b. We can clearly observe that the system is able to perpetually store the OFF/ON state until a new input set/reset control pulse appears, thus demonstrating the storage capacity of this polarization-based flip-flop memory. We must stress that the sharp transition edges of the output $S_3(z=L,t)$ represent the temporal counterpart of the sharp transitions in the hysteresis cycle observed in Fig. 18b, and are thus linked to the nonlinear time of the system: as a rule of thumb the larger is L or input power, the sharper are the edges.

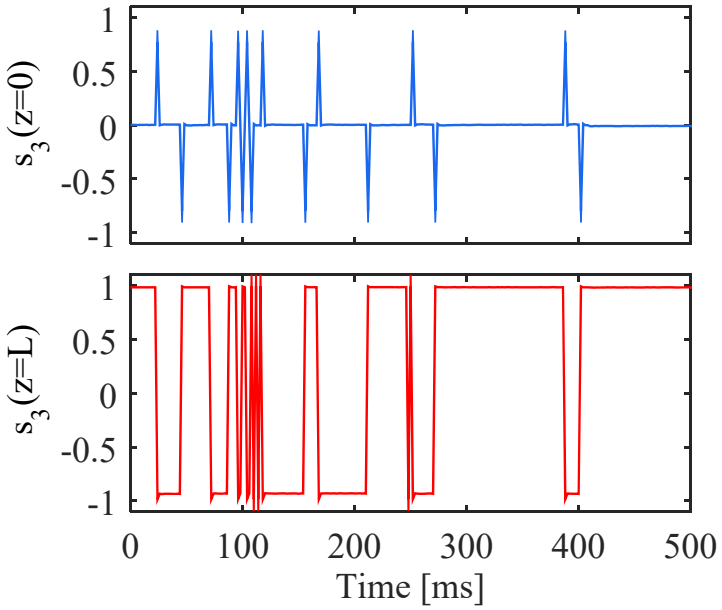

Fig. 19. Experimental proof-of-principle of a flip-flop polarization memory based on the hysteresis behavior outlined in Fig.18c. The Omnipolarizer consists in a 4-km long NZ-DSF fiber with an average power of 570 mW (L=4) and ρ=0.9. (a) Triggering sequence set/reset $S_3(z=0,t)$ injected into the fiber (each polarization spike is characterized by a width of 2 ms, and a rise time of 20 μs). (b) Experimental recording of the output $S_3(z=L,t)$ component.

C. Polarization based all-optical router

Another interesting exploitation of the hysteresis properties of the Omnipolarizer may consist in the implementation of a polarization-based all-optical router [61]. The key-principle is the same as in the flip-flop memory described just above, which is the sharp transitions in presence of set/reset input polarization events. To this aim, the initial partially incoherent signal is now replaced by a 10-Gbit/s RZ signal. As in the flip-flop memory experiment reported above, an arbitrary sequence of 2-ms set/reset s_3 spikes is imprinted on the incident 10-Gbit/s signal thanks to an opto-electronic polarization controller. In order to characterize the switching efficiency, a polarization beam splitter (PBS) is inserted at the output of the Omnipolarizer to monitor the intensity profile corresponding to both orthogonal branches of the hysteresis. The envelopes of the switching packets are first detected with a low-bandwidth oscilloscope while the 10-

Gbit/s eye-diagrams are monitored by means of a 50-GHz sampling oscilloscope.

Figure 20a1 displays the input S_3 set/reset control spikes imprinted on the 10-Gbit/s signal and detected on the low bandwidth oscilloscope beyond the PBS. No polarization segregation still occurs and thus the eye-diagram (a2) presents a combination of both orthogonal polarization PBS channels. At the opposite, when the average power is increased to 27.5 dBm (L=4), the combined effects of polarization digitalization and associated hysteresis cycle make the whole energy to switch from one axis of the PBS to the other with an excellent discrimination. Remarkably, the output polarization does not depend on its current input value but also on its past value. Indeed, the switch remains in its last state until an erasing polarization trigger is sent in input, thus demonstrating the all-optical remote processing capability of that system. As a result, we can observe on both axes of the PBS in Figs. 20b1 and 20c1 the appearance of anticorrelated data packets corresponding to the set/reset initial sequence. Finally, the 10-Gbit/s eye-diagrams displayed in Fig. 20b2 and 20c2 show a wide opening as well as a high polarization digitalization efficiency with an extinction ratio between each orthogonal axis above 20 dB.

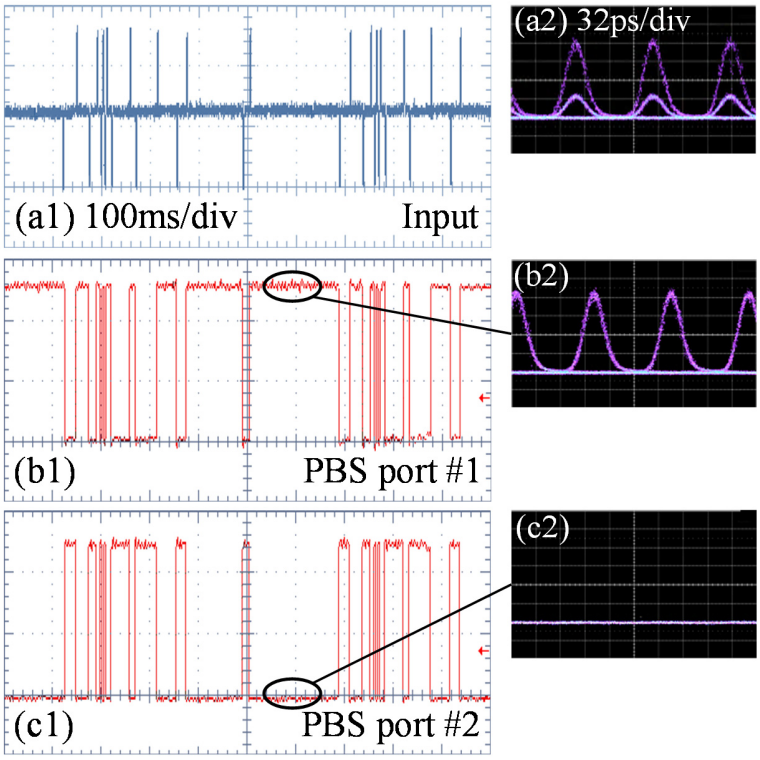

Fig. 20. Proof-of-principle of data-packet switching operation based on the hysteresis properties of the Omnipolarizer. Parameters of the system are the same as in Fig. 18c. The 10-Gbit/s RZ input signal has an average power of 27.5 dBm (L=4). The left column displays the temporal evolution of the intensity profile recorded beyond a PBS and monitored on a low-bandwidth oscilloscope. (a1) Input set/reset $S_3(z=0,t)$ spike sequence. (b1, c1) Output intensity profile on port#1 and port#2 of the PBS. (a2, b2 and c2) Corresponding 10-Gbit/s eye-diagrams.

Finally, as already noticed in previous sections, for typical fibers undertest which correspond to few-km long DSF fibers, a Kerr coefficient γ close to 2 $W^{-1}km^{-1}$, and an injected power of 500 mW (L~5), the system relies on a strong nonlinear regime which enables an effective flip-flop and switching operations. Higher input powers can obviously improve the performance of the present device with wider hysteresis cycles and shorter switching time. However, these performances grow asymptotically and therefore, using higher average power than 500 mW do not bring real and evident benefits with respect to the present experimental conditions.

VII. ALL-OPTICAL CHAOTIC POLARIZATION SCRAMBLER

In this section we discuss the third operating regime of the Omnipolarizer, first introduced in section IV with Figs. 7b & 8e, which enables us to implement an all-optical fully chaotic polarization scrambler. Indeed, as underlined in sections IV, for a large power imbalance between the forward beam and its backward replica, the system cannot reach a stationary regime. Indeed, the two counter-propagating paths are not reciprocal and the system exhibits a genuine chaotic dynamics so that even a well-polarized incident signal becomes scrambled all over the Poincaré sphere at the fiber output [62-68]. Moreover, in order to magnify this route to chaos, it is well known that the addition of a temporal delay into the feedback loop of a nonlinear system (to decorrelate the temporal fluctuations of the incoming and reinjected signals) can improve the performance [94-97]. The key idea of this section is then to implement an additional segment of fiber into the reflective loop which length is much larger than the response time of the Omnipolarizer, typically much larger than L_{nl}. This study enables us to develop a fully chaotic all-optical scrambler with drifting speeds up to 600-krad/s [63]. In contrast to commercially available polarization scramblers that are usually based on the cascade of fiber resonant coils, rotating wave-plates, or fiber squeezers and opto-electronic elements [98-104], here the present device is fully chaotic instead of deterministic and can in principle achieve similar performance. However, clearly commercial units are less expensive and benefit from a significantly lower power consumption (typically 10 W compare to 50 W for the present solution).

The second practical application highlighted in this section relies on the possibility for this chaotic regime to harvest its randomness properties in order to generate a sequence of random numbers. Indeed, a genuine random number generator (RNG) must produce unpredictable, unreproducible and unbiased sequences of numbers. For that specific reason, many true RNGs are based on the peculiar properties that characterize a chaotic dynamics. Practically, the advantage of using an optical approach is that one can generate random numbers at high repetition rate directly in the physical layer rather than using classical algorithmic techniques. Examples of such all-optical RNG include optoelectronic devices such as chaotic oscillations of high-bandwidth lasers [105-106], polarization chaos from a VCSEL diode [107], supercontinuum generation [108], homodyne detection of vacuum states [109], cosmic photons [110], spontaneous emission [111], super-luminescent diodes [112] or exploiting the randomness inherent to quantum mechanics effects [113-114]. Here we exploit the chaotic SOP dynamics of the Omnipolarizer to generate random binary sequences. In this proof-of-concept experiment, the evolution over time of the output Stokes parameters has been recorded and sampled according to a fixed threshold so as to compute a binary sequence of one billion of bits. The degree of randomness of the generated bit sequence has been then evaluated using the standard statistical benchmark provided by the dieharder testing suite [115], which shows that polarization chaos in optical fiber can be an efficient source of randomness for the generation of random numbers.

A. Numerical modelling

In order to simulate such a random system including the time-delayed feedback loop *Ld*, we implement the following numerical procedure illustrated in Fig. 21. Eqs. (3) are numerically resolved along the whole propagation distance *L+Ld* while the boundary conditions and time-delay are taken into account in such a way that $\mathrm{J}(\mathrm{L}+\mathrm{Ld},\mathrm{t}) = \rho\mathrm{RS}(\mathrm{L}+\mathrm{Ld},\mathrm{t})$, where R, as in the previous sections, denotes the rotation matrix of the reflective device. The key point here, compared to previous sections, is that the nonlinear Kerr coefficient γ (as well as fiber losses) is taken to zero along the *Ld* segment. In this way, the nonlinear coupling between the counter-propagating waves is only effective in the first segment z = [0, *L*], thus emulating the desired feedback delay.

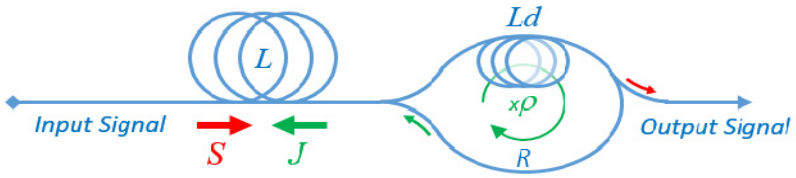

Fig. 21. Principle of operation of our all-optical scrambler: The signal wave S is injected and interacts only in the fiber of length *L* with its backward replica J generated by an amplified reflective delayed loop.

Before describing the experimental and numerical results, we would like here to briefly comment by means of simple qualitative arguments the mechanism underlying the chaotic regime of the Omnipolarizer introduced above in Fig. 8e. As will be shown below, polarization scrambling is characterized by a fast and disordered motion of the Stokes vector on the surface of the Poincaré sphere. This scrambling process originates from the fact that both waves, due to their large power imbalance and through their mutual cross-polarization interaction, cannot converge towards a mutual reciprocal nonlinear birefringence equilibrium. Consequently, even weak polarization fluctuations present in the incident waves are magnified through the nonlinear coupling that exists between the wave itself and its counter-propagating amplified replica. In fact, this feedback avalanche process prevents the Omnipolarizer to reach a stationary state, leading to large polarization temporal fluctuations at its output. Moreover, the insertion of an optical delay within the feedback loop allows to achieve a complete decorrelation between the incident and backward wave fluctuations, which greatly helps the system to enter into its chaotic operation regime.

B. Experimental setup

In order to study the chaotic dynamics of the Omnipolarizer, we have implemented the experimental setup depicted in Fig. 22, which is roughly similar to the one described in Fig. 10.

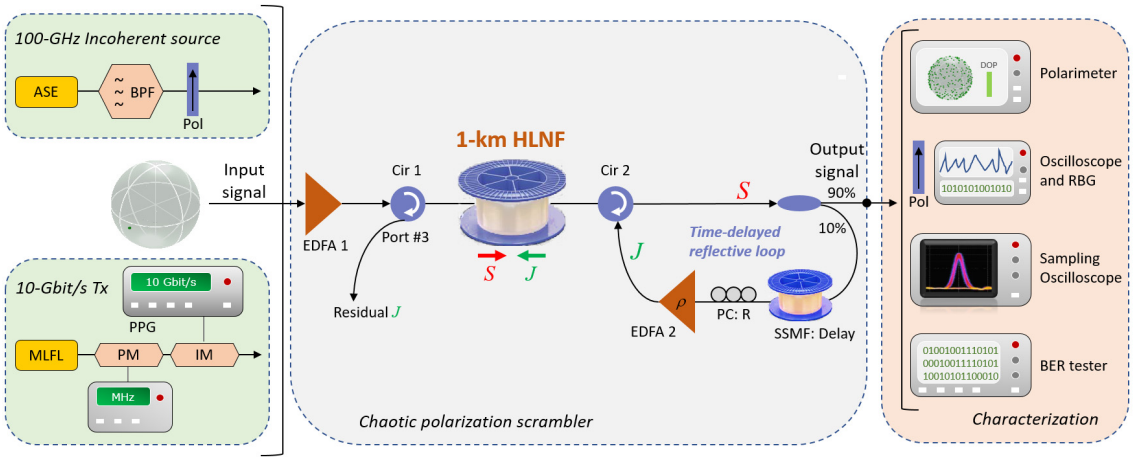

Fig. 22. Experimental setup of the all-optical polarization scrambler. ASE: Amplified spontaneous noise emission, BPF: bandpass filter, Pol: Polarizer, PPG: Pulse pattern generator, MLFL: Mode-locked fiber laser, PM: Phase modulator, IM: Intensity modulator, EDFA: Erbium-doped fiber amplifier, CIR: Optical circulator, HNLF: highly nonlinear fiber, PC: polarization controller, SSMF: Standard single mode fiber, RBG: Random bit generation, BER: Bit-error-rate.

The nonlinear Kerr medium consists here in a 1-km long highly nonlinear fiber characterized by a nonlinear coefficient $\gamma = 9$ W^{-1}.km^{-1} and fiber losses α of 0.7 dB/km. In contrast to the classical Omnipolarizer of Fig. 4, here the feedback loop, made of an optical circular coupled to a polarization controller and EDFA-2, also

includes an additional km-long spool of standard single mode fiber (SSMF) as optical delay line. As in the previous sections, for fundamental studies, the input signal consists in a fully-polarized 100-GHz bandwidth incoherent wave centered at 1550 nm. The incident signal is amplified to 14 dBm by means of the EDFA-1 before injection into the HNLF. At the output of the system, the SOP of the resulting signal is characterized by means of a standard commercial polarimeter. Furthermore, for the next random bit generation experiments, the output signal SOP is projected on an inline polarizer in order to transfer the polarization chaos into intensity fluctuations. The resulting random signal is then recorded by means of a 1-GHz photodiode and a fast oscilloscope before digitalization process. In a final step, in order to further assess the performance of this all-optical chaotic scrambler for telecom applications, the incoherent wave has been also substituted by a 10-Gbit/s OOK signal at 1550 nm. This return-to-zero (RZ) optical signal is generated from a 10-GHz mode-locked fiber laser (MLFL) delivering 2.5-ps pulses at 1550 nm. This 10-GHz pulse train is then intensity modulated thanks to a LiNbO3 Mach-Zehnder modulator driven by a 10-Gbit/s pulse pattern generator (PPG). Note that the initial pulse train is also phase modulated at 100 MHz in order to prevent any deleterious effect from Brillouin backscattering.

C. Route to chaos

Fig. 23a displays a typical example of a 3-dimensionnal bifurcation diagram recorded at the Omnipolarizer output as a function of the amplification factor g. More precisely, it corresponds to the projection of the output SOP in the S_2-S_3 plane. For that measurements, the input power is fixed to 14 dBm while the optical delay-line imposed on the backward signal consists in a 5-km long spool of SSMF.

Three different regions for the ρ parameter can be observed in Fig. 23a. First-of-all, for a moderate value of the reflective coefficient ($\rho < 8$, corresponding to a backward average power close to 20 dBm), it can be clearly seen that the two waves do not interact, consequently, the output SOP remains almost constant. For higher values of ρ, typically ($8 \leq \rho < 20$, ~ 24 dBm), the system becomes unstable and starts to oscillate. In this transient regime, more or less complex and closed trajectories can be observed whose complexity and fundamental frequencies increase with the level of backward power. Metastable fixed points can be also observed in this transient region. Moreover, in this transient regime, the dynamics of the system was found to be dependent on both the input SOP and the rotation matrix R. In contrast, increasing further the reflective coefficient ρ beyond 20 allows the Omnipolarizer to enter into its chaotic regime. In this case, clouds of points can be observed in the S_2-S_3 plane. Indeed, large fluctuations and aperiodic chaotic behaviors are reached independently of the input SOP and its rotation matrix R, leading to a full scrambling of the output SOP.

In order to further characterize the scrambling and chaotic behavior of the output SOP, we have then compared in Figs. 23b-e the output Poincaré spheres extracted from the previous measurements for different values of the reflective coefficient. While the output signal is characterized by a fixed SOP for a weak value of ρ=1 (a single point on the sphere in Fig. 23b), we can clearly note in Fig. 23c that the output SOP describes a closed trajectory in the transient regime (here ρ=10) and then exhibits a more or less complex behavior for larger values of the reflective coefficient (ρ=17 in Fig. 23d), before covering almost homogeneously the entire surface of the sphere for higher values of ρ (ρ=53 in Fig. 23e). The present results demonstrate the scrambling potential of the underlying process. The two remaining questions are how fast and what the degree of randomness is at the output of the system? To go deeper into these opened questions, we have also reported in Figs. 23b-e the corresponding RF spectra of the output S_1 Stokes component. As the reflection coefficient ρ is increased, one can easily notice that the resulting RF spectrum evolves from a DC component (stationary state) to well-defined set of discrete frequencies in the transient regime (closed periodic trajectories), until reaching a broad continuum of frequencies without any discrete lines (Fig. 23e), which further evidences the aperiodic and random nature of SOP fluctuations in the chaotic regime.

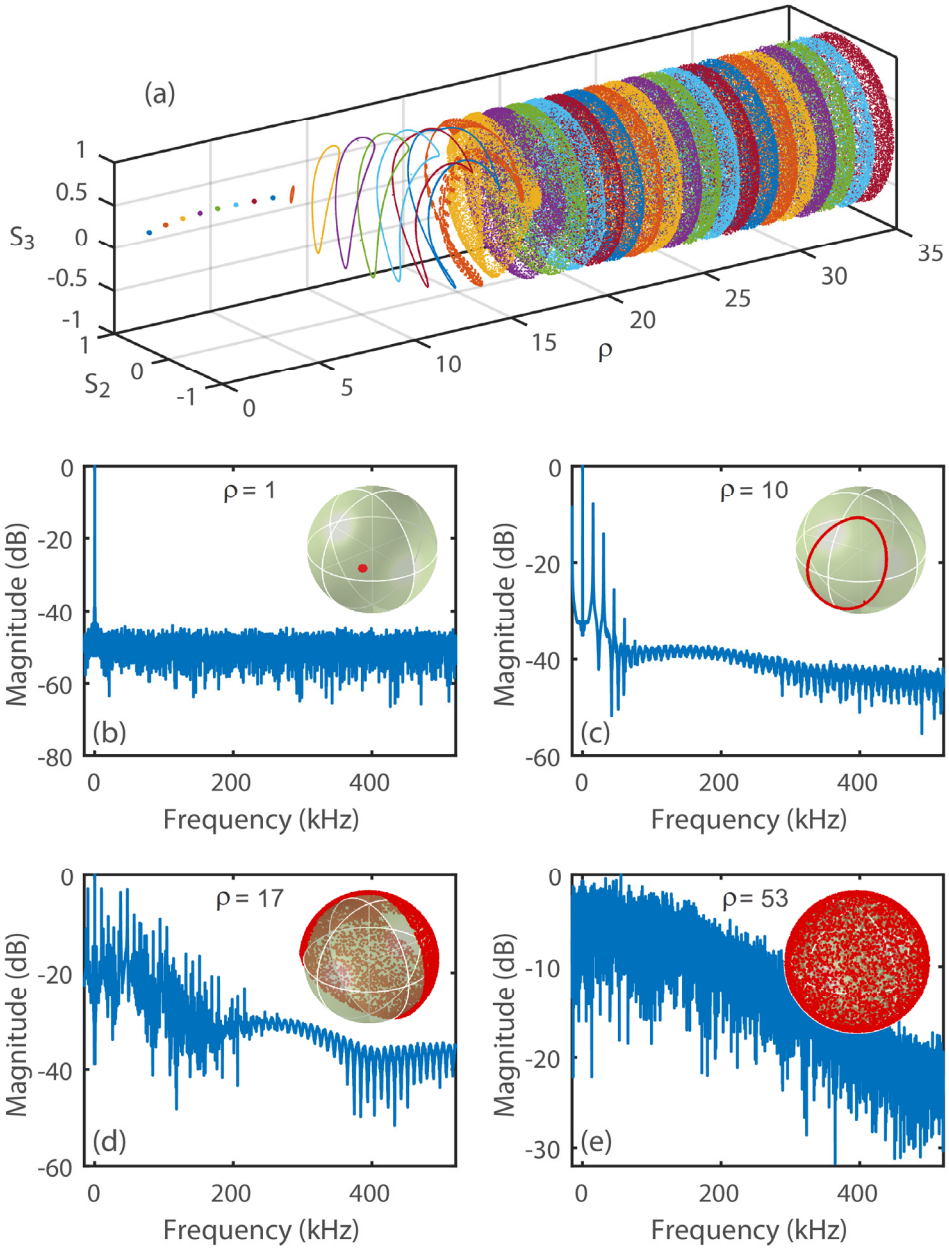

Fig. 23. (a) Bifurcation diagram recorded in the scrambling regime of the Omnipolarizer: Projection of the measured output SOP in the S2-S3 plane as a function of the reflective coefficientρ. (b-e) Poincaré sphere for different values of the reflective factor ρ as well as corresponding RF spectrum of the S_1 component: (b) ρ=1, (c) ρ=10, (d) ρ=17 and (e) ρ =53.

Finally, to further understand the key role of the time-delay introduced into the reflective loop as well as its reflective coefficient ρ, we have carried out a series of experiments and numerical simulations in three different configurations of delay: 0 delay (Omnipolarizer configuration reported in ref. [62]), 1 km of SSMF included into the reflective loop and then 5 km. Furthermore, we have carefully recorded 100 of realizations for each value of the parameter ρ, each of them having a different polarization rotation matrix R adjusted randomly thanks to the opto-electronic polarization controller in the loop so as to ensure that the chaotic

regime is reached independently of the SOP of the backward replica. The input power is still kept constant to 14 dBm. The scrambling performances have been evaluated thanks to the calculation of the DOP by means of Eq. (4) and scrambling speed (V_{scr}), defined as:

$$V_{scr} = \langle 2 \arcsin\left(\frac{1}{2}\frac{\partial \vec{s}(L,t)}{\partial t}\right)\rangle \tag{5}$$

Figs. 24(a-c) summarize the experimental results of the output DOP as a function of ρ, while Figs. 24(d-f) report the corresponding scrambling speed V_{scr}. Red solid lines depict average values of DOP and speed, while the shaded areas display respective fluctuations (standard deviation in grey and maximum excursion in ochre).

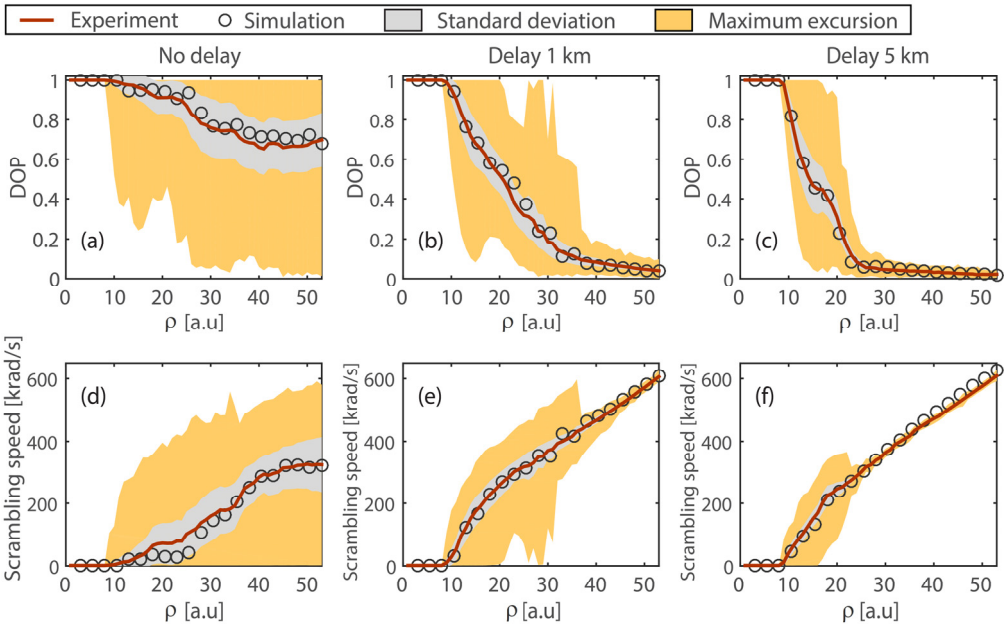

Fig. 24. (Top line) DOP measured at the output of the system as a function of the reflective coefficient ρ for the 0-delay configuration (a) a 1-km long delay-line (b) and 5-km long delay-line (c), respectively. (Bottom line) Scrambling speed as a function of amplification factor ρ (same convention as for DOP measurements). The red solid-lines correspond to the experimental data averaged over 100 realizations, while the shaded areas represent respective fluctuations (standard deviation in grey and maximal excursion in ochre). The black circles correspond to the numerical simulation results averaged over 24 realizations.

From Figs. 24, the influence of the delay-line becomes evident. Indeed, for an increasing delay starting from 0 to 5 km, the threshold value of ρ required to enter into a genuine chaotic scrambling regime and thus reach a DOP close to zero (at least <5%) is found to be significantly reduced. More precisely, compared to the zero-delay case, depicted here in Fig. 24a, the insertion of a delay-line within the reflective loop allows to achieve at least a 2.5-fold reduction of the reflective coefficient ρ so as to enter into the chaotic regime. Moreover, it is important to stress that the strong system fluctuations, typically generated in the transient regime, progressively vanish for $\rho \geq 40$ when a 1-km long delay-line is inserted into the system and just above 30 (backward power of 26 dBm) with a 5-km spool of delay, thus making the scrambling performances more reproducible and reliable. The same behavior can be observed for the scrambling speed in Figs. 24(d-f) for which at least a 2-fold increase of V_{scr} is achieved for the same reflective coefficient value when a 5-km long delay-line is inserted into the system. The performance and repeatability of the device are also greatly improved due to a strong reduction of fluctuations of the output scrambling speed.

These results underline the fact that the polarization instability and its route to chaos can be significantly improved by feeding this self-organized system with an optical time-delay. We attribute this behavior to the fact that the polarization fluctuations of the backward waves are mutually decorrelated from each other, which greatly helps the system to enter into its chaotic regime. Finally, we have also reported in Figs. 24 with black circles the results obtained from numerical resolution of Eqs. (3) averaged over 24 realizations, each involving a different rotation matrix R and including the exact experimental parameters, in particular taking into account for the limit response of our polarimeter (1Msa/s). We can observe an excellent agreement between our numerical predictions and the experimental data, thus validating our theoretical model and providing a reliable tool for designing a home-made chaotic polarization scrambler.

Finally, to highlight in more details the key role played by the length of the delay-line, we have carried out the following additional measurements. For a fixed reflective coefficient ρ=53, we have measured the resulting scrambling speed and DOP at the output of the Omnipolarizer as a function of the length of SMF inserted into the reflective loop. Moreover, to further characterize the chaotic nature of our system, we have also calculated the corresponding Lyapunov coefficient $\mathscr{L}$ following the procedure described in ref. [116]. A positive value of the Lyapunov coefficient means that the system is highly unstable and highly sensitive to initial conditions, a prerequisite for any chaotic system. These measurements are summarized in Figs. 25, and have been averaged over 100 realizations involving different rotation matrices R.

From this figure, we can fairly observe the strong impact of the feedback delay-line with a clear threshold around 200 m which enables to reach a maximum scrambling speed close to 610 krad/s (blue circles) and very low values of DOP (red triangles). This threshold behavior is consistent with the nonlinear response of the system and can be explained by the fact that, to enter into a fully chaotic regime, the decorrelation time-scale between both counter-propagating waves is governed by the nonlinear length of the system, evaluated here close to 180 m for ρ=53. Note also the excellent agreement between our measurements and numerical predictions (averaged over 24 runs), depicted in Fig. 25a by means of blue stars for the scrambling speed and red crosses for DOP. Finally, the calculation of the experimental Lyapunov coefficient $\mathscr{L}$, depicted in Fig. 25b, shows that thanks to an increase of a delay-line into the feedback loop, $\mathscr{L}$ becomes largely positive for a fiber length beyond 200 m when ρ=53, confirming aforementioned conclusions and providing a clear signature of the chaotic nature of the SOP at the output of the system. As already highlighted in previous Fig. 24, we can also notice the strong reduction of fluctuations in the system performance owing to the feedback delay, thus making our device more reliable.

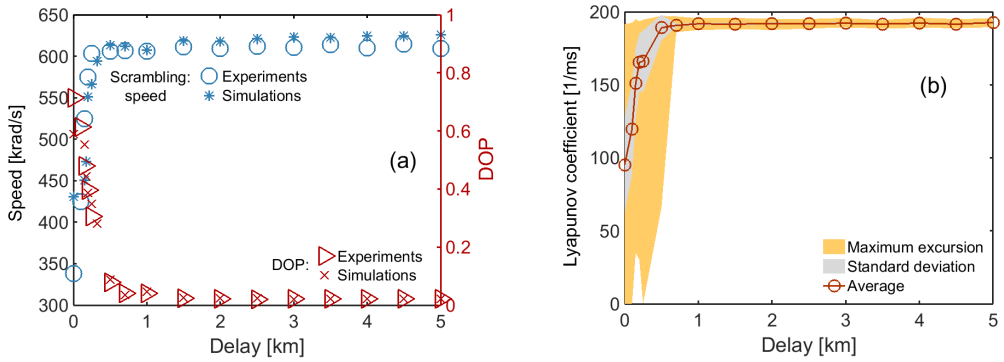

Fig. 25. (a) Scrambling speed (blue circles) and corresponding DOP (red triangles) as a function of the fiber length used as delay-line within the reflective loop of the Omnipolarizer. The amplification factor is kept constant to ρ=53. Numerical simulations are displayed with blue stars (scrambling speed) and red crosses (DOP), respectively. (b) Corresponding experimental Lyapunov coefficient $\mathscr{L}$. All measurements have been averaged over 100 realizations.

D. *Polarization scrambling of a 10-Gbit/s optical signal*

Our chaotic all-optical scrambler has been then tested in a telecommunication configuration. For this proof-of-principle, we used a 10-Gbit/s RZ signal centered at 1550 nm. The pulse width has been chosen as short as 2.5 ps in order to evaluate the impact of the scrambler for higher repetition rates of data or high-frequencies analogic signals. The delay-line inserted into the reflective loop is fixed to 5 km while the input power is kept constant to 14 dBm. To ensure that our device operates in a genuine chaotic regime, the amplification factor has been chosen to ρ=53, corresponding to a backward power of 28 dBm. Figure 26 summarizes our results.

Firstly, Figs. 26a&b display respectively the input and output Poincaré sphere of the 10-Gbit/s signal. While the SOP is totally fixed at the input of the system (one single point), the output Poincaré sphere appears entirely covered, thus confirming that an efficient scrambling process can be achieved, even with high-repetition rate pulsed signals. Furthermore, Figs. 26c&d depict the output eye-diagrams when the backward signal is OFF (Fig. 26c) and in scrambling regime (Fig. 26d, pump ON). We can observe that the shape of the output pulses is ideally preserved with a clear-open eye-diagram, which validates the applicability of our polarization scrambler for RZ telecom signals. Note however the presence of an additional amplitude jitter into the scrambled eye-diagram in Fig. 26d. This source of noise was attributed to the Rayleigh backscattering imposed by the backward signal on the output beam. Nevertheless, in a wavelength division multiplexing (WDM) configuration, one could exploit one isolated pump channel in order to filter out this deleterious noise source, as already proposed in our ref. [62] which shows in particular that the scrambling regime of the Omnipolarizer is fully compatible with WDM systems.

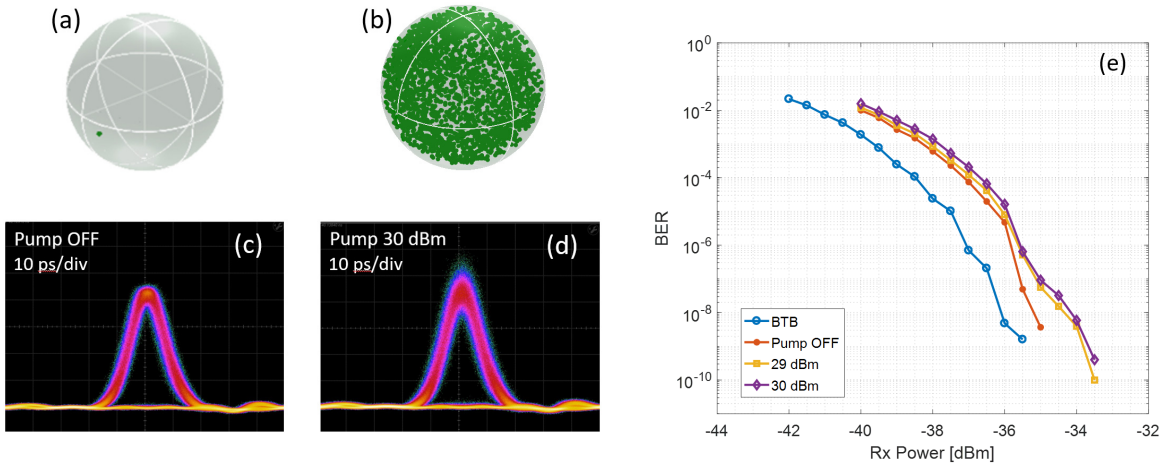

Fig. 26. (a) Input Poincaré sphere of the 10-Gbit/s RZ signal. (b) Output SOP in scrambling regime for ρ=53. (c&d) Output eye-diagrams of the 10-Gbit/s signal recorded in pump OFF (c) and pump ON configuration (d). (e) BER measurements as a function of the average power incoming on the receiver, back-to-back configuration (blue circles), pump OFF (red dots) and pump ON: 29 dBm (yellow squares) and 30 dBm (purple diamonds).

Next, to further assess the quality of the transmitted signal, we have performed BER measurements as a function of the average power incoming on the receiver. Figure 26e compares the back-to-back configuration (blue circles) with the pump OFF (red dots) and ON (purple diamonds) cases for two values of the backward power (29 dBm and 30 dBm). We can first stress that an error-free transmission is achieved for the scrambled signal, confirming that our scrambler is fully compatible with such single-channel RZ telecom configuration. However, a slight power penalty (0.5 dB) has been measured between the pump ON/OFF curves, which is attributed to the Rayleigh backscattering induced by the intense backward signal. A power penalty of 1.5 dB has been detected compared to the input configuration, which is mainly attributed to the deleterious effects of chromatic dispersion and Kerr effect on the ultra-short pulses used in our experiments.

E. Random bit generation

The genuine chaotic nature of our all-optical scrambler provides a good opportunity to exploit this optical system as random number generator (RNG), a field that has recently received much attention in photonics [63, 105-112]. To this aim, in the last part of this section dedicated to polarization chaos, we take advantage of the chaotic evolution of the output Stokes parameters to experimentally generate random bit sequences. For this proof-of-concept experiment, the evolution over time of a Stokes parameter has been recorded and concatenated from a large number of different realizations in order to build a 10^9-long bit sequence. Such long sequences are mandatory in order to perform standard statistical Dieharder tests as described below [115]. The principle of operation is to convert a Stokes component of the output field into either a 0 or 1 depending on its relative value according to some specific threshold, here calculated from the median value of the waveform. In this series of experiments, the S_1 component is recorded beyond an inline polarizer by means of a photo-receiver connected to a 1-Gsa/s oscilloscope. For that purpose, the chaotic polarization scrambler uses a 5-km delay-line as well as an amplification factor ρ=53. The input signal corresponds to the 100-GHz partially coherent wave described in the previous sections.

Fig. 27a displays a part of a typical experimental realization of the raw data (blue solid-line) as well as the post-processing involved in the random numbers extraction. Basically, the waveform is first under-sampled at a clock rate whose frequency is chosen well below the typical correlation length of the signal under test so as to ensure a reliable randomization. In our practical case, the clock (in black) has been chosen to 10 kHz for a typical scrambling speed of 610 krad/s. The S_1 signal is then sampled (red points) at each rising edge of the clock. After suitable thresholding by calculating the median value of the sampled signal, the binary random sequence represented in Fig. 27b has been obtained. Note that 5 days of continuous recording involving more than 1.2 To of raw data have been necessary to construct the billion bit sequence required for the dieharder test. Finally, in order to improve the randomness of the sequence and successfully pass the benchmark tests (which in fact represents a challenging task), we also remove any residual correlation and bias associated with binary conversion using an exclusive-or (XOR) gate between the initial sequence and its time-delayed replica [63, 108, 111-112]. A delay of 50 bits was here applied.

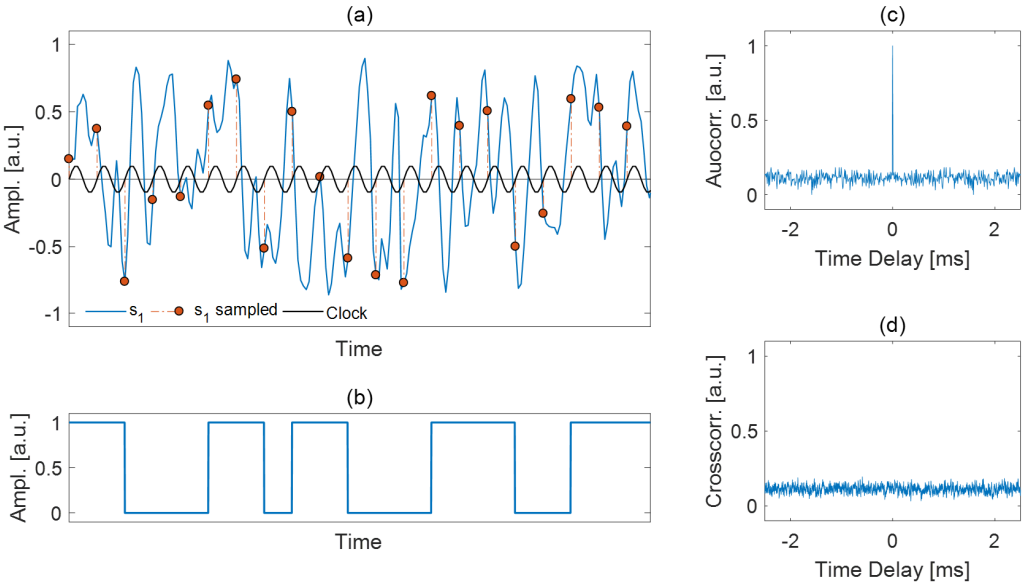

Fig. 27. (a) In blue, evolution of the S_1 Stokes parameter over time. In red: sampled values taken in correspondence of rising edges of an ad-hoc defined clock (in black). (b) Random sequence generated after thresholding samples chosen in (a). In (c) and (d) autocorrelation and cross-correlation functions of different random sequences generated in experiments.

The degree of randomness of the computed binary sequence was first tested through calculation of the autocorrelation trace (Fig. 27c), and the cross-correlation function between two different sequences (Fig. 27d). These first results reveal a vanishing cross-correlation for all of the generated random bit streams, indicating that all the sequences are different and that the proposed technique is a good candidate for RNG.

Finally, to further assess the degree of randomness of the generated billion bit sequence, we have implemented the celebrated statistical benchmark dieharder tests [116]. Results are summarized in Fig. 28 and show that the generated sequence pass all the statistical tests (a requirement p-value > 0.01), thus demonstrating that the polarization chaos induced by a counter-propagating time-delayed feedback is a suitable source of randomness to generate arbitrary binary sequences.

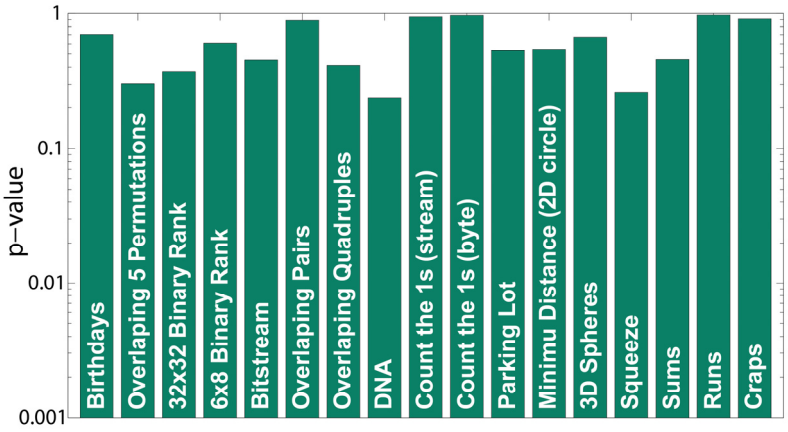

Fig. 28 Dieharder benchmark tests results for the 10^9 experimental binary sequence generated from polarization chaos.

VIII. POLARIZATION-BASED TEMPORAL CLOAKING

A. Principle

Recent research has been focused on the ability to manipulate a light beam in such a way to hide, namely to cloak, an event over a finite time or localization in space. The main idea is to create a hole or a gap in the spatial or time domain so as to allow for an object or data to be kept hidden for a while and then to be restored. By enlarging the field of applications of this concept to telecommunications, researchers have reported the possibility to hide transmitted data in an optical fibre. In these latter cases, inspired by the space-time cloak technique originally introduced in [117] by McCall and co-workers, the concept of space-time duality between diffraction and dispersion has allowed Gaeta *et al.* [118], to successfully demonstrate the temporal cloaking of an isolated time event upon tens of picoseconds as well as Weiner *et al.* to hide a 12.7-Gbit/s dark-return-to-zero data stream in optical fibers by means of a 46% temporal cloaking window [119]. In order to surf on this trendy topic, we have tried to exploit all the dynamics offered by the Omnipolarizer (alignment and chaotic regime) in order to demonstrate a polarization-based temporal spying and blinding process of optical data replicated by a parametric FWM process [60].

Indeed, in previous temporal cloaking demonstrations reported in refs [118-119] for which the roles of space and time were analyzed, a temporal event was revealed or hidden to an observer thanks to the spectral modifications of an illuminating CW probe. Here, from a different perspective, we introduce the SOP of the incident signal as a potential new degree of freedom. We consider the following scenario in which a pump wave is used by an *indiscreet-eye* to copy incident optical data thanks to a FWM conversion process. Since the parametric process under used is highly polarization dependent, the ability of the Omnipolarizer to self-trapped, or self-scrambled the signal SOP allows to maximize (copying mode) or, alternatively, make blind the wavelength conversion process. Moreover, in contrast to previous demonstration of temporal cloaking,

the present polarization-based scenario enables to copy or conceal 100% of an optical data stream, without any restriction to a finite temporal window or a localized time event. In the following, we successfully characterize the performance of our system by alternatively copying and then concealing 100% of a 10-Gbit/s transmitted signal.

B. Experimental implementation

In order to demonstrate the capability of the Omnipolarizer to prevent the wavelength conversion process occurring in a parametric amplifier, we have implemented the following experimental setup displayed in Fig. 29 and involving two different Omnipolarizers and one fibre optical parametric amplifier (FOPA). The initial signal consists in a 10-Gbit/s 25-ps RZ sequence generated at a wavelength of 1554.1 nm. In order to mimic the random nature of the signal SOPs resulting from the propagation in an optical transmission line, we make use of a polarization scrambler that spreads the incident signal SOP all over the Poincaré sphere. The first Omnipolarizer is made of a 6.2-km long NZDSF fiber in which the 26-dBm input signal nonlinearly interacts with its own counter-propagating replica generated at the fibre-end by means of a reflective-loop setup with a reflective coefficient ρ close to 1.6 in order to fully operate in the alignment regime of the Omnipolarizer. In a second stage, we make use of a polarization sensitive FOPA to simulate a "spying process". It basically consists in a 1-km long segment of weakly anomalous dispersion HNLF in which a 26-dBm CW pump wave centered at 1550.55-nm is coupled with the incident signal, so as to carry out a parametric wavelength conversion process towards an Idler-wave centered on 1547 nm. Finally, in order to keep the process reversible and potentially "undetectable", the randomness of the signal SOP needs to be restored. As a consequence, after the copying or blinding process, the signal beam is injected into a second Omnipolarizer OP2, whose large power imbalance (typically 13-dBm vs 28-dBm for the forward and backward beams, ρ~60) ensures an efficient polarization scrambling process.

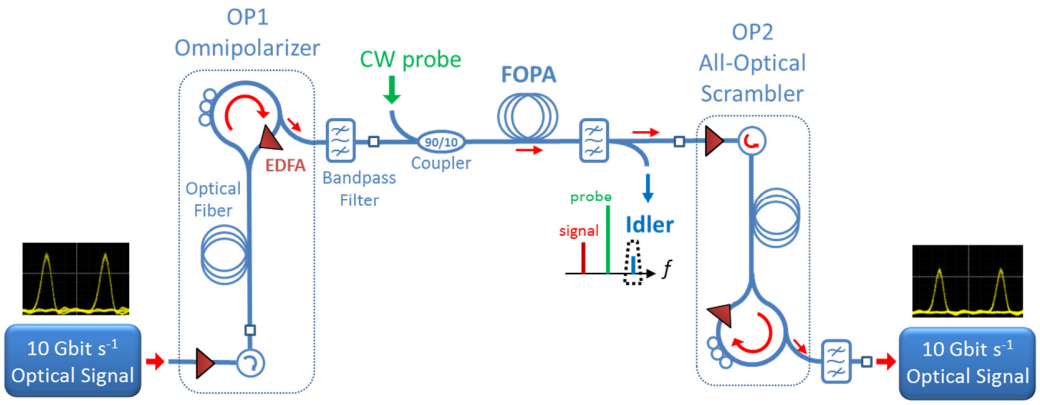

Fig. 29 Experimental setup of the polarization-based cloaking process. OP: Omnipolarizer, EDFA: Erbium doped fiber amplifier, FOPA: Fibre optical parametric amplifier.

C. Proof-of-principle experiment

The following figure summarizes our experimental results for both the copying and blinding operation modes. In a first stage, the copying process of the incident signal is analyzed in the case where both Omnipolarizers are turned OFF. In order to emulate the propagation in a genuine optical telecommunication link, the incident signal exhibits a random polarization which covers uniformly the whole surface of the Poincaré sphere (Fig. 30a). As a result, when the 1-dBm 10-Gbit/s signal is coupled into the FOPA with its 26-dBm CW pump wave, due to the strong polarization dependence of the parametric process, all the polarization fluctuations are transferred into the time domain on the Idler wave. Consequently, after filtering the 1547-nm wavelength converted signal, the resulting eye-diagram of the duplicated signal remains

completely closed (see Fig. 30b), which reflects a complete loss of the data and thus an ineffective reading or hiding process.

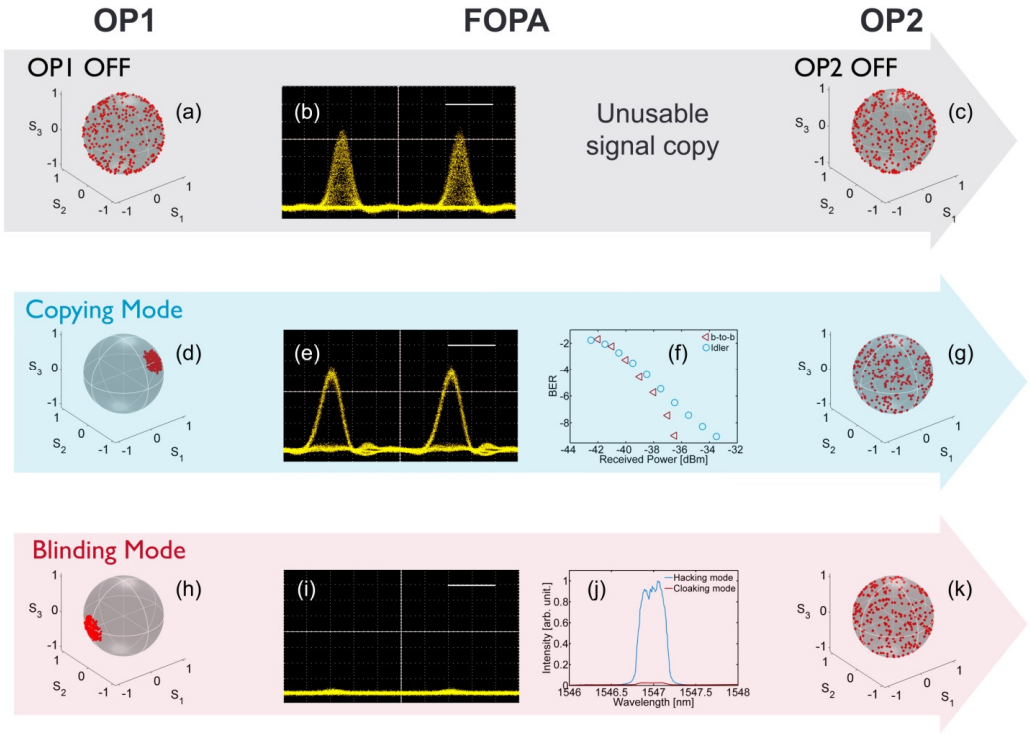

Fig. 30 Experimental results of copying and cloaking operations. First top row, both Omnipolarizers are OFF: Since the incident signal is randomly polarized, its corresponding Poincaré sphere is uniformly covered (a). Consequently, due to the strong polarization dependence of the parametric process taking place in the copying FOPA device, all the polarization fluctuations are transferred in the time domain on the Idler wave and the resulting eye-diagram appears completely closed. In output of the system, the initial propagating signal remains unaffected, just a simple rotation of its Poincaré sphere (c). Copying mode: Both Omnipolarizers are turned ON. The first OP self-traps the SOP of the incident signal parallel to the SOP of the FOPA pump (d). As a result, the generation of the Idler (copy) wave in the FOPA is maximized and an error-free detection of these replicated data is successfully achieved independently of the initial signal SOP (f, b-to-b: back-to-back measurements at the emission). Finally, the second OP ensures a transparent operation processing thanks to its ability to self-scramble the SOP of the output signal (g). Blinding modes: Both Omnipolarizers are turned ON. The first OP self-traps the SOP of the incident signal orthogonally to the FOPA pump SOP (h). As a result, the generation of the Idler (copy) wave in the FOPA is minimized, thus making blind the copying setup; (i) eye-diagram recorded at the output of the FOPA; (j) optical spectrum at the output of the FOPA. A temporal concealing of the incident signal is successfully achieved independently of its initial SOP. In the final stage, the randomness of the signal SOP is restored thanks to the OP2 (k). In subplots b, e and i, the scale bar corresponds to 40 ps.

In contrast, when the Omnipolarizer OP1 is turned ON, the incident signal spontaneously self-traps its polarization state parallel to the pump FOPA SOP, in such a way to maximize the generation of the Idler wave (copy). Therefore, the corresponding Poincaré sphere recorded at the output of the first OP1 is characterized by a strong reduction of polarization fluctuations, as illustrated by the small residual SOP area on the sphere displayed in Fig. 30d. The phenomenon of polarization trapping is even more striking when monitored in the time domain. Indeed, for a reflective coefficient of ρ=1.6 in the feedback loop of the OP1, the duplicated 10-Gbit/s signal is now able to overcome the strong polarization dependence of the

wavelength conversion process in the FOPA and is now characterized by a wide-open eye-diagram (Fig. 30e). Moreover, the BER measurements carried out on this converted signal and depicted in Fig. 30f with blue circles confirm that an error-free detection is continuously achieved with a weak penalty compared to the back-to-back configuration (red triangles). Finally, in order to ensure the user-transparency of this copying process, the second OP2 is turned ON so as to restore a random polarization state for the signal wave at the FOPA output as illustrated in Fig. 30g.

In contrast, in the blinding mode, when the first OP traps any incident signal SOP orthogonally to the FOPA pump SOP (Poincaré sphere in Fig. 30h), the generation of the Idler wave in the FOPA is then reduced in a dramatic way, independently of the incoming signal SOP. Therefore, the power of the duplicated signal is decreased by more than an order of magnitude (13.5 dB), which makes the present copying setup completely blind to the transmitted signal. This is remarkably illustrated by the spectrum depicted in Fig. 30j, which compares the Idler spectra obtained in the copying (blue) and blinding (red) modes. Indeed, despite the CW-illumination process, the eye-diagram detected in the blinding mode (Fig. 30i) is continuously kept below the detection noise level and does not exhibit any kind of usable signal. We finally note that, as in the copying mode, the signal at the HNLF output is finally scrambled thanks to the OP2, which operates into its chaotic regime (see the Poincaré sphere in Fig. 30k).

IX. Polarization condensation in the middle-point of an optical fiber: The unfolded Omnipolarizer

In our first pioneer studies dealing with polarization attraction process, we have seen and demonstrated that the injection of a pump beam with a fixed SOP at the fiber output was a prerequisite for the existence of the phenomenon of polarization attraction [43-45]. At this time, the general concept was that the fully polarized pump beam serves as a SOP reference for the signal beam, and thus plays the role of natural attractor for any arbitrary polarized incoming signal. Then, we have demonstrated with the Omnipolarizer that polarization attraction can also take place in the absence of any SOP reference thanks to a mirror-induced feedback mechanism [59]. An arbitrary polarized incident light beam is then able to self-organize its SOP upon propagation in an optical fiber, into a universal and environmentally robust SOP owing to its own feedback replica. The remaining question is what does happen if a randomly polarized incident signal (a scrambled signal) is now injected simultaneously at both sides of a standard telecommunication optical fiber?

A. Numerical results

Not so surprising, the polarization process still occurs but in the exact middle point of the optical fiber [69-70], as already mentioned in sections III & IV. More precisely, for a perfect symmetric configuration (same injected powers), as shown numerically for the isotropic case in Fig. 1a, both counter-propagating replicas converge to the only stable state leading to a reciprocal nonlinear birefringence and corresponding to co-rotating SOPs. Consequently, whatever the initial ellipticity, the system relaxes towards two pools of attraction corresponding to the right and left circular polarization states at the exact middle point of the fiber. Beyond this attraction point, both signal replicas recover their initial polarization distributions at their corresponding fiber outputs. In a loose sense, this attraction effect remains completely ‘hidden’ in the fiber for an external observer. This is probably the reason why, although intuitive, this effect has never been highlighted so far. Another approach to describe this mechanism is that this attraction in the mid-point of the fiber can be viewed as an unfolded version of the Omnipolarizer, simply outspread around the central mirror and for which the boundary conditions impose $S(z=0,t) = J(z=L,t)$.

For the randomly birefringent fiber, the mechanism appears quite similar. However, we have seen in the theoretical description of section IV that the system modeled by Eqs. (3) is characterized by additional physical properties due to the averaging of birefringence fluctuations along the fiber length. In this particular case, the left and right-circular SOPs are still the natural attractors of the system, which is now characterized

by three constants of motion defined by the K vector. Therefore, the stationary states of S and J take the form of sine and cosine standing waves that naturally tend to co-rotating SOPs in order to fulfill the reciprocal birefringent criterion. Since both the boundary conditions and the physical systems are perfectly symmetrical, both waves reach these circular SOPs at the exact middle point of the fiber.

To further illustrate the origin of this self-ordering process, we have to make reference to the stationary states. To this aim, we have resolved numerically Eqs. (3) by imposing an initial conditions such as S(z=0,t) = J(z=L,t) (same arbitrary polarized signal injected simultaneously at both ends of the fiber). Figs. 31(a-c) display the final stationary states along the fiber length for the three Stokes parameters of S and J. It can be seen that S and J follow quite the same spatiotemporal dynamics with an inversion of the sign in components S_1 and S_2 due to the particular constant of motion $K_1=S_1+J_1$ and $K_2=S_2+J_2$, as described in Fig. 9 for the case of the Omnipolarizer. Since $K_3\sim0$, S_3 and J_3 follow exactly the same spatial trajectories and reach the co-rotating SOPs in L/2. Moreover, as the boundary conditions are the same for S and J, then the trajectories are symmetric with respect to L/2 and cross the 0 point near L/2 for S_1 (J_1) and S_2 (J_2) whist reaching S_3=+/-1. We can also note the excellent agreement between numerical results and analytical expressions of the stationary states obtained from ref. [70]. Note also that compared to the isotropic case, described in Fig. 1a, we can notice that the curvature of the spatial trajectories in the telecom fiber is more pronounced. This is due to the sine-shape of the spatial trajectories in the telecom fiber, compared to hyperbolic solutions in the isotropic case. Consequently, the measurements would be more sensitive in terms of symmetry and precision in the middle-point of the fiber.

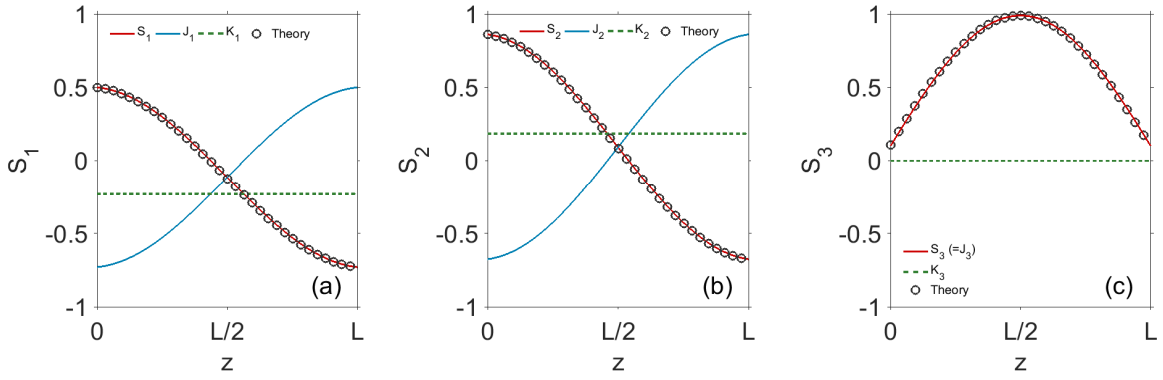

Fig. 31 Example of stationary states obtained for S and J when the same boundary conditions ($S_1=J_1=0.5$, $S_2=J_2=0.86$, $S_3=J_3=0.1$) are injected in both sides of a telecom fibre of length L=10. Circles display the theoretical stationary states.

If we now compute a large number of different stationary states and calculate the probability density function (pdf) along the propagation distance *z*, we obtain the subplots of Fig. 32 which display the pdf of each Stokes parameter of the forward beam S. We can then clearly see that in the stationary regime, the first two Stokes components S_1 and S_2 shrink in z=L/2 around $S_1\sim S_2\sim0$, whilst almost all the spatial trajectories are passing close to S_3=+/-1 in the middle point of the fiber, thus confirming that the right- and left-circular SOPs remain the natural attractors of the system, even in the absence of any SOP reference. Note however that if the input SOP is too close to the equator ($S_3\sim0$), the system becomes unstable due to its bistability.

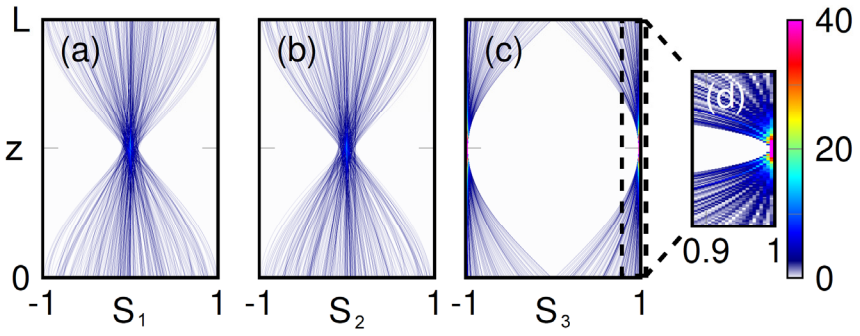

Fig. 32 Probability density function of the three Stokes components of the SOP for the forward beam as a function of distance z. The PDFs have computed from 342 realizations.

Let us now consider the Poincaré sphere representation, which represents the most convenient quantity measured in experiments. We consider here the simplest scenario in which the same arbitrarily polarized wave is injected simultaneously at both ends of the fiber leading to S(z=0,t) = J(z=L,t). As mentioned above, the phenomenon of self-polarization manifests itself by the spontaneous organization of the SOP of both waves around two pools of attraction in the exact middle point of the optical fiber, at z=L/2. This is illustrated by the following results of the numerical simulations of Eqs. (3).

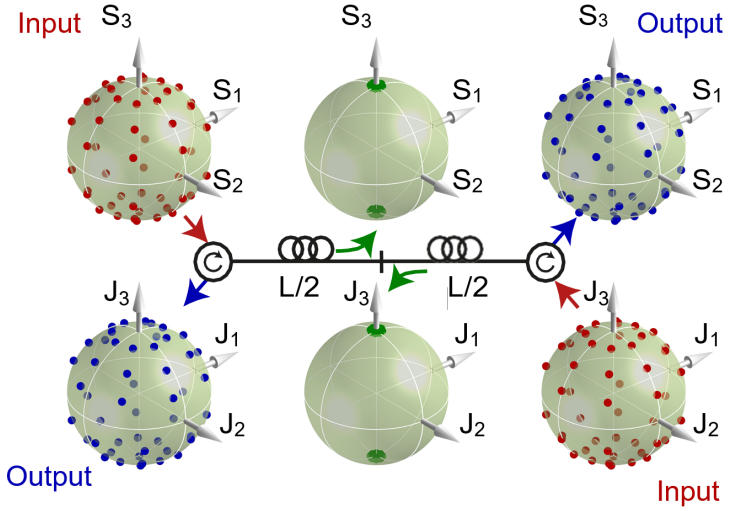

Fig. 33 Numerical simulations of the polarization attraction process occurring in the middle point of an optical fiber for a normalized length L=15. The red, green and blue dots denote respectively the initial (z=0), middle (z=L/2) and output (z= L) SOPs of the signal S (upper panels) as well as its counter-propagating replica J (lower panels).

In this computation, 64 different initial SOPs of the signal, and thus of its counter-propagating replica have been uniformly distributed over the surface of the Poincaré sphere. The boundary conditions are kept fixed in time and we report in Fig. 33 the stationary states of the SOP which are reached after a sufficient long and more or less complex spatio-temporal transient regime. The simulations clearly reveal that the system relaxes towards a different stationary state for each injected polarization S(z=0). These stationary states have the property that all the resulting SOPs are close to a circular state in the middle of the fiber for L large enough (here $15L_{nl}$). Note that the SOPs initially localized on the equatorial plane are not attracted towards a circular polarization. These numerical results show the remarkable efficiency of this self-polarization process originated from the symmetry breaking phenomenon described in the first sections of this

manuscript. Note also the symmetric behavior of the forward and backward beams. After propagation, it is also remarkable that both propagating replicas recover their random nature at their respective outputs, just as this spontaneous phenomenon of self-organization was hidden in the middle point of the fiber and was undetectable from its both ends.

B. Experimental setup

To demonstrate experimentally the polarization attraction occurring at the middle point of an optical fiber, we have implemented the experimental setup depicted in Fig. 34. It corresponds basically to an unfolded version of the Omnipolarizer described above. Here we use in input a partially 100-GHz incoherent wave, which is injected into a fiber loop made of 10 km of TWHD. Each counter-propagating replica propagates along the loop on only one single round-trip before being evacuated by means of two optical circulators. At the exact middle point, we extract 1% of the circulating beams in order to analyze the SOP in L/2. Moreover, a 4-port optical switch associated to a commercial polarimeter is used to characterize the output SOPs in z=L/2 as well as in z=0 and L for both counter-propagating waves. It is important to notice that due to the different paths of fiber pigtails between each inputs and outputs, the resulting measurements of the Poincaré spheres are not absolute, but only relative to each other, i.e., there is an arbitrary polarization rotation between the two signal replicas.

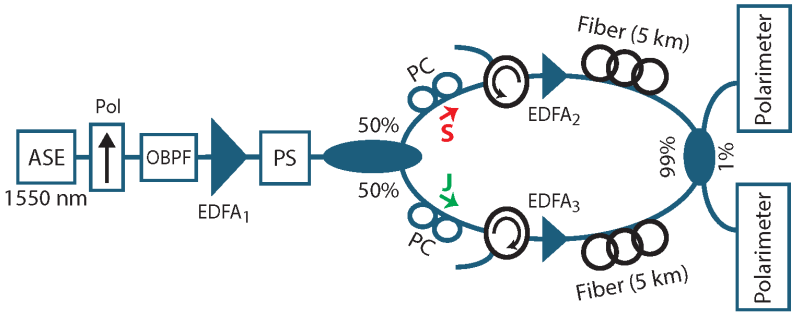

Fig. 34 Experimental setup implemented to highlight the polarization condensation process occurring in the middle-point of a telecom optical fiber. The present setup corresponds to the classical Omnipolarizer, such as shown in Fig. 4 but unfolded in a loop configuration.

C. Experimental results

Figure 35 displays the experimental recording of the resulting Poincaré spheres of both S and J when the same polarization scrambled signal is injected at opposite ends of the fiber with an average power of 27 dBm, which leads to a normalized fiber length of L=10. In this example, 256 randomly distributed polarization states are used as input signals (red spheres in Fig. 35). The initial polarization rotation between both replicas of the signal is adjusted by means of the polarization controllers in each arms of the loop so as to maximize the efficiency of the attraction process. Indeed, this self-polarization effect is experimentally observed for only a limited range of input rotations, corresponding to the absence of rotation along the S_3-axis [70].

In contrast to the fully disordered input spheres, when monitoring the SOPs at the exact middle point of the optical fiber for both S and J (see green spheres in Fig. 35), we can clearly observe an aggregate of points localized around two pools of attraction as predicted by the numerical simulations of Fig. 34 (here arbitrarily oriented along the S_3-axis). These spheres demonstrate a powerful self-organization process of the two polarized waves during their propagation as well as an efficient attraction of their SOPs in z= L/2, in good qualitative agreement with theoretical predictions. In contrast, when monitoring the output Poincaré spheres, the mutual attraction process is no longer observable and both waves recover their respective random polarization distributions, as expected from previous simulations. This observation is fully similar to the

case of the Omnipolarizer for which the backward wave recovers its disordered state before exiting the fiber. In a loose sense, it could be understood by the conservation of disorder imposed by a constant entropy.

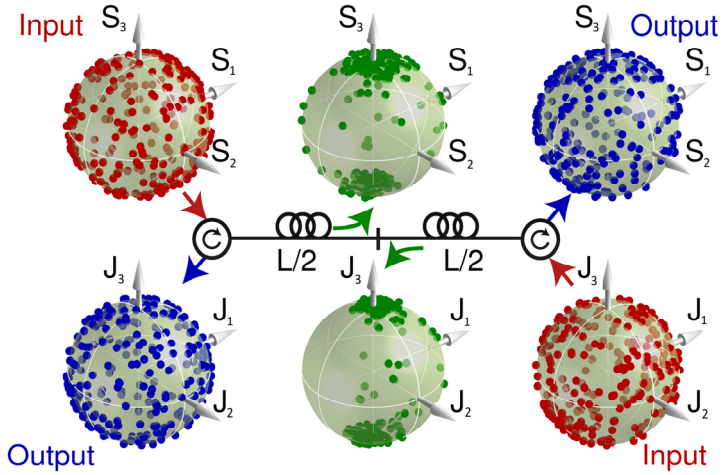

Fig. 35. Experimental Poincaré spheres recorded for S (top) and J (bottom) when the same disorder polarization beam is injected at both ends of a telecom optical fiber. The spheres are monitored in the input (red dots), output (blue dots) and in the middle point of the fiber (green dots). The power of each wave is set to 27 dBm (L=10) and the number of different input SOPs is 256.

Figure 36a shows the efficiency of this attraction process as a function of the input power, here represented by the fiber length normalized by the nonlinear length. For each recording, we carefully check that the system corresponds to a symmetric configuration for which the same power is injected at both ends of the fiber. In order to fairly characterize the efficiency of this process, instead of the classical DOP calculation introduced in the above sections, here we use a geometrical definition of the DOP. More precisely, for each initial SOP, we compute the distance on the sphere to the ideal polarization (here, left or right circular SOP) and we define the amount of spreading d as the average value of the different distances.

$$d = \frac{1}{N}\sum_{1}^{N}\sqrt{(\theta_k - \theta_c)^2 + sin^2\theta_c(\phi_c - \phi_k)^2} \tag{6}$$

where θ and ϕ are respectively the polar and azimuthal angles on the sphere, the indexes k and c refer to the initial and circular SOPs. Note that the index k runs over all the initial SOPs of the signal beam which effectively relax towards the circular polarization under consideration. Indeed, the quantity d appears more appropriate to quantify the attraction efficiency than the classical DOP, since d takes into account not only for the averaging of the Stokes parameters, but also for the ordered nature of the SOPs ensemble. Indeed, a small value of the distance d reflects an efficient attraction process towards both poles of the Poincaré sphere, while the conventional DOP would be zero in this case.

As can be seen in Fig. 36, the efficiency of this phenomenon increases significantly with the injected power, as revealed by the reduction of the average spreading d of the SOPs in Fig. 36a. Moreover, for a fiber length larger than L=15, the distance d remains almost constant, which corresponds to the lower limit of the attraction process and its asymptotic nature.

Figure 36b shows how the system evolves when a power imbalance (asymmetric case) is introduced between the two beams defined as ρ=S(z=L)/J(z=L). In this case, the power of the signal replica under study remains fixed to 28 dBm, while the power of the counter-propagative beam varies from 18 to 28 dBm. Note that the results for S and J are obtained with two different runs of measurements. We can then clearly observe the sensitivity of this process and the detrimental effect of power imbalance on the repolarization effect.

Indeed, we note that for a power imbalance higher than 40%, the self-repolarization effect vanishes completely in the middle point of the fiber.

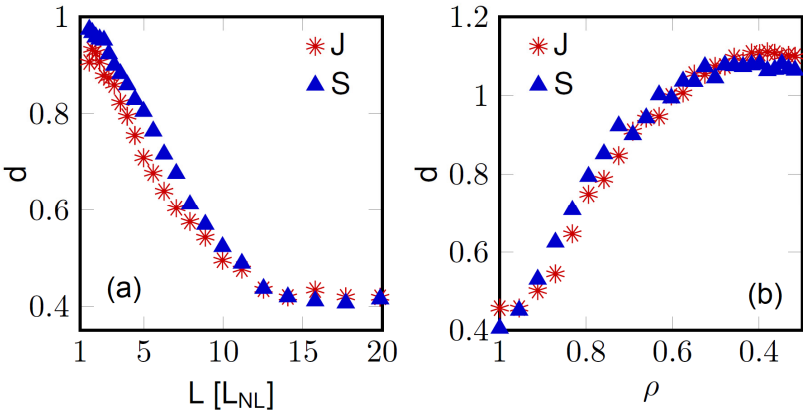

Fig. 36. (a) Experimental evolution of the SOP spreading *d* defined in Eq. (6) as a function of the fiber length L (normalized by the nonlinear length) (b) Experimental evolution of the SOP spreading *d* as a function of the power imbalance ratio ρ. Note that in panel (b), the state of polarization of S (resp. J) is measured at fixed power, by varying the power of J (resp. S).

X. POLARIZATION CONDENSATION OF RANDOM WAVES IN THE MIDDLE-POINT OF AN OPTICAL FIBER

In order to go deeper into the repolarization of counter-propagating arbitrary polarized waves, the ultimate configuration consists in injecting two independent random waves characterized by uncorrelated polarization fluctuations at both ends of an optical fiber. This configuration is clearly the link between the Omnipolarizer (self-feedback reference) and the pioneer polarization funnel using an external pump with fixed SOP. Surprisingly, in contrast with our common belief and previous studies which require either the injection of a polarization reference or a feedback, we will see in the following that when two random waves counter-propagate through an isotropic fiber, they are first attracted towards a specific SOP in the middle-point of the fiber and then, as in the previous case, both recover their polarization randomness at their corresponding fiber outputs [69]. This effect is quite unexpected, since this phenomenon is here able to create an order state from two distinct uncorrelated disordered waves.

A. Numerical modelling

The origin of this phenomenon is mainly related to the phenomenon of symmetry breaking described in section II, and relies on the fact that in an isotropic fiber, the only stable polarization configuration of counter-propagating waves is the co-rotating SOPs. Therefore, whatever the initial conditions imposed at both ends the fiber, the system will spontaneously relax towards a co-rotating left-handed or right-handed circular state. Moreover, in contrast to the previous case, occurring into a randomly birefringent telecom fiber, here the cross-polarization coupling between the two counter-propagating waves is twice the value of the nonlinear self-phase coupling term. It then allows for the system to reach faster their natural attractors in a hyperbolic-shaped trajectory. Consequently, both waves will be stronger and longer trapped onto these circular states, which guaranties that a self-polarization process occurs around the middle point of the fiber. This is confirm by numerical simulations of Eqs. (2). Indeed, as depicted in Fig. 37 which shows 200 different random stationary states, the attraction points still correspond to the right and left circular SOPs. It can be clearly seen that these SOPs still play the role of natural attractors for the system since any trajectory will pass close to one of these two fixed points in the middle point of the fiber and remains trapped along a

wide range of distance z. Consequently, if the counter-propagating injected polarization states fluctuate adiabatically, i.e. for sufficiently large coherence times (typically, 2 orders of magnitude slower that the nonlinear time), the spatiotemporal system is then able to follow approximately the stationary behavior, thus explaining this unexpected polarization phenomenon.

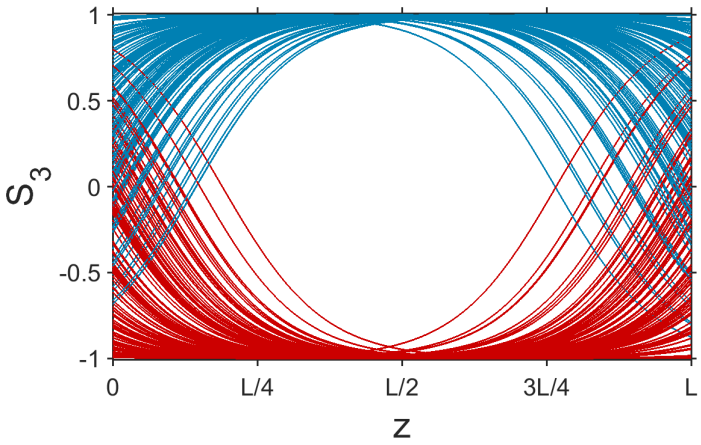

Fig. 37. Stationary solutions $S_3(z)$ along the fiber length for a set of two counter-propagating polarization random waves (200 runs). The trajectories attracted towards the north and the south poles are, respectively, plotted in red and blue.

B. Experimental results

In order to study experimentally this effect of polarization condensation in the mid-point of an isotropic fiber, we have implemented the experimental setup displayed in Fig. 38.

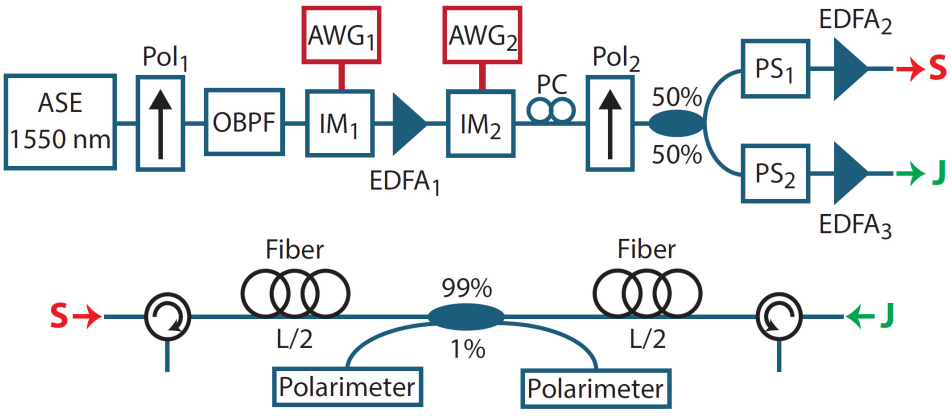

Fig. 38. Experimental setup implemented to highlight the polarization condensation phenomenon in an isotropic fiber. ASE, amplified spontaneous emission; Pol, polarizer; OBPF, optical bandpass filter; IM, intensity modulator; AWG, arbitrary waveform generator; EDFA, erbium doped fiber amplifier; PS, polarization scrambler.

It is rather similar to the previous one described in Fig. 34. However, for that particular case and in order to consider true isotropic fiber segments, short samples have been involved: typically two 100-m long segments of TWHD fibers. Moreover, to prevent any additional source of birefringence, the fibers under-test were

first off-spooled and carefully wound around a 2-m-diameter ring. In this way, the final 200-m long fiber segment can be considered as close as possible to the ideal isotropic case described by Eqs. (2). Then, to enable a direct monitoring of both counter-propagating SOPs, a 99:1 tap coupler was spliced at the exact middle point of the fiber. The input signal consists in our home made 100-GHz partially incoherent wave described above. To reach an efficient nonlinear regime of propagation, a series of two intensity modulators followed by Erbium amplifiers was then implemented to generate 4.5-W peak-power flat-top 5-μs pulses at a repetition rate of 5 kHz. In this way, a high power CW pumping configuration can be approximated with a normalized fiber length of L=2. The initial signal is also split into two parts and independently polarization scrambled before entering the optical fiber.

Figure 39 displays the experimental recordings of the resulting Poincaré spheres of both S and J when the two waves are injected simultaneously at opposite ends of the fiber with a peak power of 4.5 W. To this aim, 256 randomly distributed initial conditions were used for both waves as shown by the red dots covering the corresponding input spheres. In contrast, when monitored in the middle of the fiber (green dots), we can clearly observe that the SOPs of both S and J segregate around two pools of attraction, (here oriented along the S_3 axis), thus demonstrating an efficient self-organization process between the two randomly polarized waves. In contrast, similarly to the previous results obtained in Fig. 35, when monitoring the output Poincaré spheres, the mutual polarization attraction process is no longer visible and both waves recover their respective random polarization distributions.

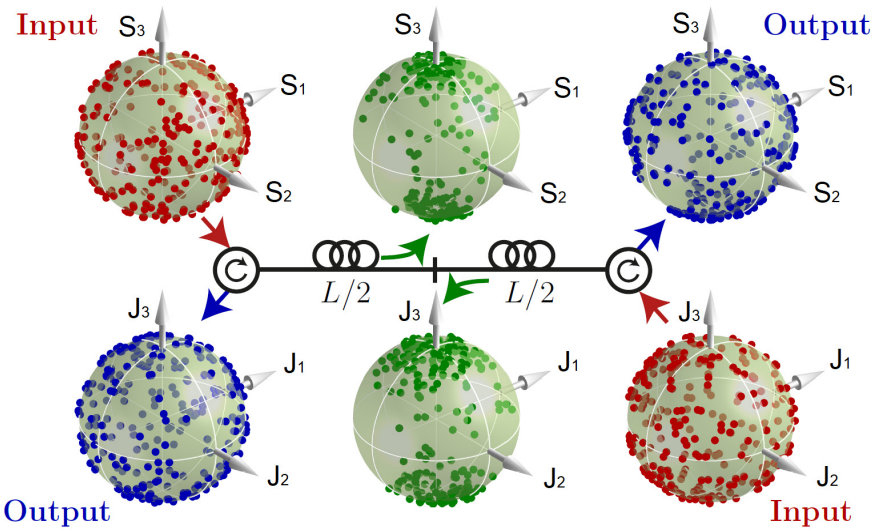

Fig. 39. Experimental Poincaré spheres recorded for S and J when two counter-propagating randomly polarized waves are injected simultaneously at both ends of an isotropic optical fiber. The input spheres are depicted with red dots, whilst the output are plotted by means of blue dots, and in the middle of the fiber with green dots. The power of each wave is set to 4.5 W (L=2) and the number of points is 256.

Finally, to further assess the efficiency of this self-organization process, we have compared in Fig. 40 the probability density function of the three Stokes parameters S_1, S_2, and S_3 of the S wave, respectively, at the input (blue color bars) and in the middle point of the fiber (green bars). These results confirm the expected behavior and show, in agreement with the numerical predictions of Fig. 37 that this process tends to focus the S_1 and S_2 Stokes parameters around the zero value, while segregating S_3 around the two extrema ±1.

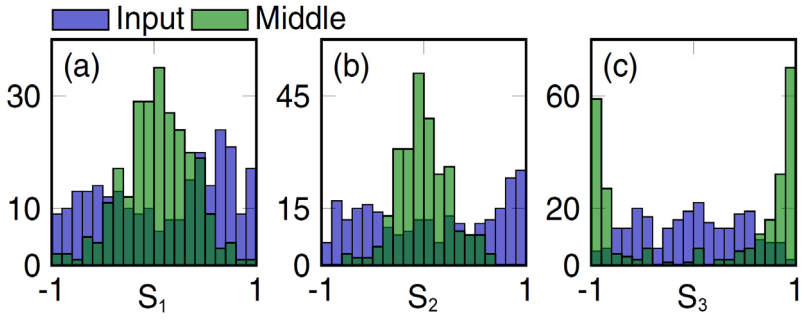

Fig. 40. Experimental probability density function of the Stokes parameters for the S wave recorded at the input (blue color bars) and in the middle of the isotropic fiber (green bars).

XI. POLARIZATION-BASED TUNNELING EFFECT

An important physical aspect of the Omnipolarizer relies on the fact that in the nonlinear stationary regime, both the forward and backward waves are coupled in each point of the fiber. By analogy with the case of two parallel pendulum chains of magnets which are coupled at every point of propagation, here any fluctuation of a wave along the fiber length is immediately compensated by the other wave in such a way to conserve a mutual reciprocal nonlinear birefringence.

This remarkable fact can have important consequences. A fascinating example is that, in the strong nonlinear regime, the previously discussed self-induced attraction process allows to all-optically speed-up the propagation of a polarization burst within the system in such a way to instantaneously write, as a kind of nonlinear mirror, a polarization information onto the backward signal, long before the linear round-trip time. This effect could be also compared to the phase conjugated mirror based on FWM. To this aim, the Omnipolarizer described in Fig. 10 was first subjected to its stationary regime thanks to the injection of a CW signal with a fixed SOP. Next, short polarization spikes are imprinted in such a way to impose strong impulse input SOP variations. These incident fast polarization pulses consist of S_3 spikes whose time duration has been adjusted to 10 µs.

First of all, the polarization burst is injected into the Omnipolarizer in such a way to propagate in a quasi linear regime. The input average power is then fixed to 16 dBm and the reflective coefficient ρ is close to 0.8. The temporal profile of this polarization burst is then detected after a polarizer at each port of the device, i.e. input; output as well as in port #3 of the input circulator to measure the backward signal. Figure 41a displays the experimental monitoring of this polarization burst propagating within the Omnipolarizer in the linear regime. At the origin of times, the polarization burst enters into the system (blue solid-line). Then, this polarization impulse is detected at the output of the device at the time corresponding to the time-of-flight along the fiber span, here 31 µs (red solid-line). Finally, after a reflection at the fiber output and back-propagation, the polarization spike is basically detected on the oscilloscope after a delay corresponding to the round-trip within the fiber, i.e. 62 µs (orange solid-line). We thus denote with “classic-spike” this usual backward replica.

This classical situation turns to be completely different when operating in the nonlinear regime. The input power is therefore increased up to 27 dBm (L=5) whilst ρ is kept constant close to 0.8. For that power, the Omnipolarizer acts in the nonlinear bistable regime. The experimental monitoring of the polarization burst transmission is now displayed in Fig. 41b and reveals a nontrivial behavior. Whereas the temporal profiles recorded at the input and output of the fiber remain similar to the previous linear regime, the backward replica now clearly exhibits the signature of the polarization spike long before its classical return along the fiber span. We talk in this case of “early-spike”, as it is marked in Fig. 41b. In fact, in analogy with the quantum tunneling mechanism, here the data carried by the polarization state of the signal has temporally “jumped” from the input to the output, without a delay imposed by its finite speed of propagation.

As a matter of fact, the early-spike seems to exit from the "residual signal" port#3 of the input circulator at the same time that the forward input spike is injected into the fiber, similarly to a fast-light phenomenon. These observations are clearly related to the stationary states of the system. Indeed, as mainly recalled along this manuscript, both waves nonlinearly interact through a cross-polarization effect in such a way to reach a mutual and stable equilibrium that satisfies the reciprocal birefringence criterion. To this aim, for any propagation distance z, both waves target a stationary state that can mutually compensate for their own and coupled nonlinear birefringence. In these experimental observations, we clearly see the consequences of this mutual arrangement by the fact that a spatially localized fluctuation introduced on one wave, immediately forces the other wave to act in an opposite manner, thus forming a kind of spatial polarization domain walls and creating this "early-spike" response. In the linear regime, the early-spike does not appear, instead, because forward and backward waves are not coupled to each other, which is the case illustrated in Fig. 41a.

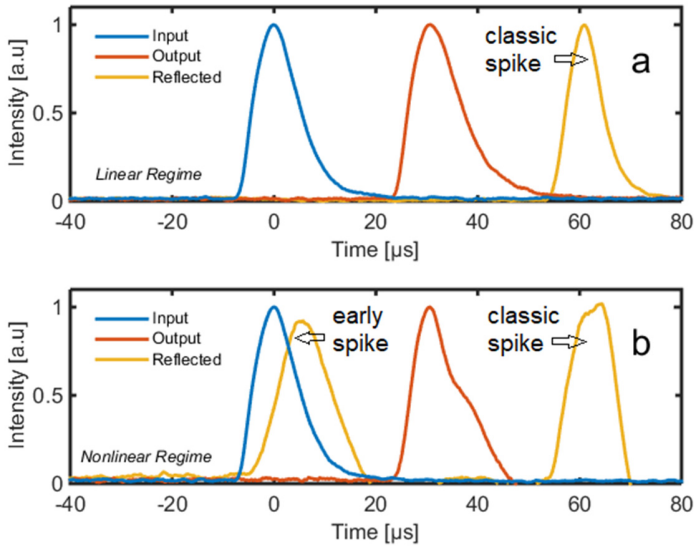

Fig. 41. (a) Intensity profile of the polarization burst propagating into the Omnipolarizer and detected beyond polarizers (a) Linear regime, the power of the input CW is P=16 dBm (b) Nonlinear regime, P=27 dBm.

Numerical simulations of this phenomenon have been carried out based on Eqs. (3) and confirm our previous experimental observations. Numerical results are then displayed in Fig. 42 and illustrate the temporal profile of a single polarization burst recorded at each port of the device, i.e. the input burst (blue line), the output forward burst (red line) as well as the backward replica (green line). The parameters used in our simulations correspond to the experimental configuration reported in Fig. 41. In the case of panel 42a, the power of the CW input signal, over which the input polarization burst is imprinted, is 16 dBm. With such a low power (L=0.4), nonlinear effects do not play any substantial role and the system acts in a quasi-linear regime. Therefore, the input burst is detected at the output of the fiber at a time corresponding to the time-of-flight, while its usual back-reflected replica, namely the "classic-spike" in green line is well detected at port #3 of the Omnipolarizer after a delay corresponding to twice the time-of-flight in the fiber, just as in experimental results of Fig. 41a.

Subsequently, panel 42b displays the temporal profiles of the polarization burst when the initial power P is increased up to 24 dBm (L=2.5). The reflected replica now exhibits the signature of a polarization burst characterized by the appearance of an early-spike long before its classical round-trip along the fiber span. Finally, to prove that the "early-spike effect" is linked to the system nonlinearity, we further increase the power up to 27 dBm (L=5) in panel 42c. In this stronger nonlinear regime, it is noteworthy that the early-spike rises even higher than the classic-spike. Note also, in panels (b&c), that the shape of both the classic-spike in the backward replica as well as the output forward polarization burst are both degraded by the system nonlinearity.

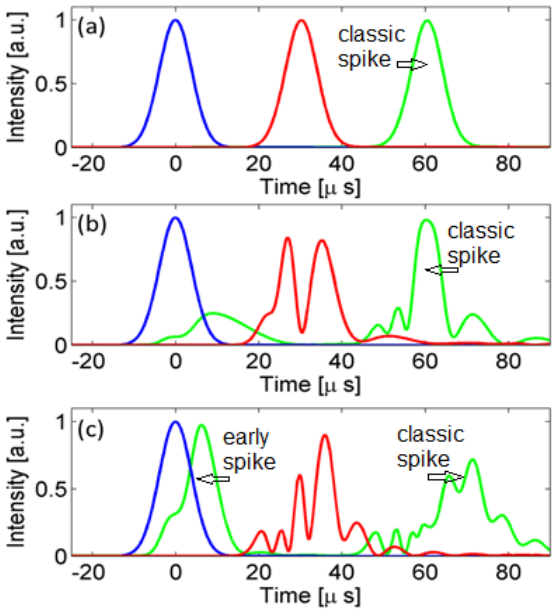

Fig. 42. Numerical simulations illustrating the intensity profile of the polarization burst propagating into the Omnipolarizer: input burst (blue line), output forward burst (red-line) and backward replica (green-line). (a) Linear regime, P=16 dBm (L=0.4). (b) Nonlinear regime, P=24 dBm (L=2.5). (c) Strong nonlinear regime, P=27 dBm (L=5). Other parameters correspond to the experimental configuration of Fig. 41.

It is also important to notice that the nonlinear response time of the Omnipolarizer, which is of the order of L_{nl}/c [49], here close to 5 µs, fixes a lower bound to the temporal width T_{spike} of the input polarization burst which can be detected. Indeed, if $T_{spike} << L_{nl}/c$ then the forward polarization burst is "transparent" to the nonlinear dynamics of the Omnipolarizer and it does not give rise to any backward early-spike: in such an instance only the classic-spike appears, as if the Omnipolarizer worked in a linear regime.

Moreover, it is worth noting that a train of forward input polarization spikes carrying optical data could be injected: in this case a corresponding train of early-spikes would be efficiently transposed and detected on the backward wave beyond the port #3 of the input circulator. The illustration of that process is depicted in Fig. 43 by means of numerical simulations. Note that in this case, the last early-spike must appear before the first backward classical-spike, otherwise they would overlap and the tunneling data would be lost. Being 2L/c the round-trip time at which the first classic-spike appears, we get a temporal transmission window of duration 2L/c during which a train of forward input spikes is quasi-instantaneously copied in the backward replica, as displayed in Fig. 43.

In the simulation under analysis we employ a 6-km long NZDSF, therefore the round-trip time is 60 µs. The input power P is increased up to 36 dBm, so that the nonlinear response becomes shorter $L_{nl}/c \approx 0.5$ µs. Therefore, one can inject polarization bursts characterized by a temporal width of T_{spike} =1 µs. Finally, several input bursts can be successively injected into the fiber giving rise to a sequence of spatial PDWs and thus encoded early-spikes.

We conclude this section by highlighting that the polarization of the backward bursts depends on the stationary-state which is reached by the system before the burst injection. Therefore, we may have input forward bursts, which are linearly polarized along the y-axis and corresponding early-spike replicas which are polarized along another direction, let-us say the x-axis. This paves the way to potential applications in the framework of data-processing. Indeed, from the example discussed above it is clear that a train of y-polarized input forward bursts may be quasi-instantaneously transcribed into a train of x-polarized backward early-spikes, which would give rise to an ultrafast polarization converter. This effect will be highlighted in the case of a birefringent fiber for temporal data compression applications in the ongoing perspectives, section XIV.A.

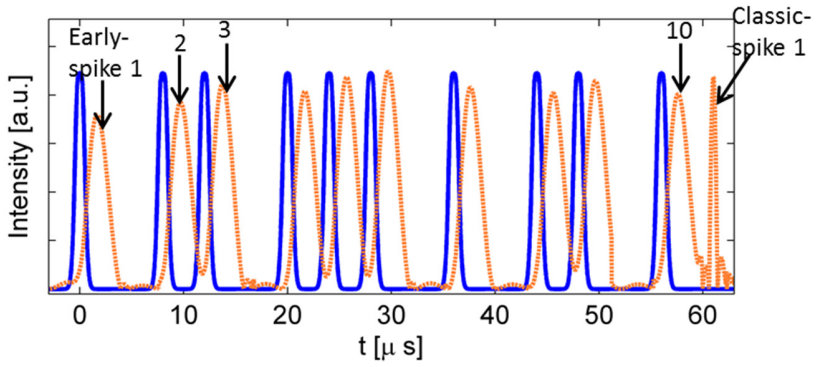

Fig. 43. Numerical simulation displaying the copying process and efficient detection of 10 early-spikes carrying a data packet. The time of flight in the fiber is here 60 μs. A train of 10 forward input polarization spikes (blue solid line) is injected into the fiber and is quasi-instantaneously transposed on the backward replica (orange dotted line). The first three early-spikes are indicated along with the last one (10), which is formed just before the first classic-spike appears at t=60 μs (round-trip time): all the 10 early-spikes are thus correctly detected.

XII. SELF-INDUCED MODAL ATTRACTION

The concept of self-induced polarization attraction within the Omnipolarizer discussed in Secs. II-XI may be extended to the spatial modes of a multimode fiber for spatial multiplexing applications [120]. This paves the way to the more general concept of *self-induced modal attraction*, where the modes may be either polarization or spatial modes of a fiber. A new scenario emerges, where light could self-organize its modal state, namely, the power distribution among the modes as well as their relative phase.

A plethora of paramount applications could benefit from such a phenomenon of modal self-organization. Self-induced modal attraction could lead to the development of an all-optical signal processing technology in the framework of spatial-division-multiplexing schemes, which are rapidly emerging as the most promising solution to face the upcoming capacity crunch of current single-mode systems [120]. Furthermore, it could provide an efficient and all-optical way to counteract parasitic and uncontrolled modal coupling effects in short multimode fibers, which are nowadays widely employed in numerous applications. Finally, self-induced modal attraction could be exploited in multicore fiber lasers for the phase-synchronization of the cores, which allows for focusing most of the energy in the fundamental supermode of the fiber: such an idea has already been explored to synchronize some tens of cores [121], but a clear theoretical understanding is still missing and could be the key to synchronize an unprecedented number of cores.

The aim of this section is not to provide a deep study of modal attraction, which is as much intriguing as challenging and will deserve strong investigations in the future. Here we want to discuss a simple but clear example of modal attraction which permits to disclose its potential application.

The coupled nonlinear Schrödinger equations (CNLSEs) ruling the dynamics of spatial modes in a telecom fiber are complex to derive, even in the simplest bimodal case, which is due to the presence of randomly varying birefringence, random mode coupling and spatial mode dispersion effects [42]. Therefore, for the sake of simplicity, here we consider a bimodal isotropic fiber in which two spatial modes co-propagate and interact with their backward replica generated by a perfectly reflecting mirror. A schematic picture of the case under analysis is illustrated in Fig. 44.

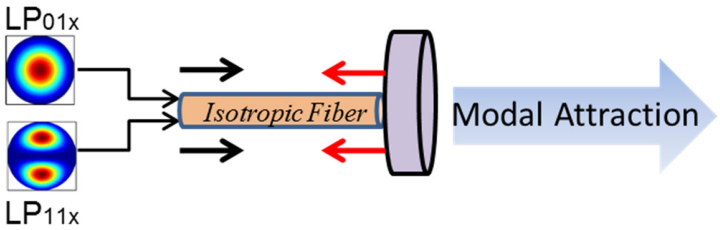

Fig. 44. Schematic illustration of the self-induced modal attraction. A combination of LP_{01x} and LP_{11x} modes is injected into a bimodal isotropic fiber (black arrows) and nonlinearly interacts with its backward replica (red arrows) generated at the fiber output by means of a reflecting device.

This part was mainly derived by M. Guasoni. Here, we indicate with F_n and B_n the electric field envelopes of the forward and backward mode of order-*n*, respectively. Assuming that all the modes are polarized along the same direction, e.g. the x-axis, and following a treatment similar to that discussed in [58], we find that the spatiotemporal dynamics of mode coupling is described by the following CNLSEs:

$$\partial_t F_n + c_n \partial_z F_n = i[C_{nn}|F_n|^2 + 2C_{01}|F_m|^2]F_n + 2i[C_{nn}|B_n|^2 + C_{01}|B_m|^2]F_n + 2iC_{01}B_m B_n^* F_m \quad (7)$$

where n={1,2}, m={1,2}, n≠m, whereas c_n is the group velocity related to mode-*n*. A similar equation is found for F_n by exchanging F↔B and $\partial_z \leftrightarrow -\partial_z$. Here, differently from Ref. [58], we make the realistic assumption that the nonlinear coefficients C_{00}, C_{11} and C_{01}, defined as in Ref. [122], may not be equal and obviously depend on their mutual intermodal effective area. Moreover, we employ the boundary condition $B_n = -F_n$ at the fiber end, which accounts for the presence of a perfect mirror. Note that C_{00} plays the role of the usual nonlinear Kerr coefficient γ in the previously discussed single-mode fibers. Furthermore, as in the polarization domain, we point out that the term $2C_{01}F_mB_mB_n^*$ in Eqs. (7) is responsible for the energy exchange between the two spatial modes, and that the strength of this exchange is thus proportional to C_{01} (the intermodal nonlinear coupling between LP_{01} and LP_{11}).

In analogy with polarization phenomena, we then define the modal Stokes parameters $S^{(m)} = [F_1F_2^* + F_2F_1^*;\ iF_1F_2^* - iF_2F_1^*;\ |F_1|^2-|F_2|^2]$ and $J^{(m)} = [B_1B_2^* + B_2B_1^*;\ iB_1B_2^* - iB_2B_1^*;\ |B_1|^2-|B_2|^2]$, as well as the nonlinear length $L_{nl}=1/(C_{00}P)$, being P the total forward power that in this case reads as $P=|S^{(m)}|=|F_1|^2+|F_2|^2$. Note that we use the superscript (m) to differentiate modal Stokes vectors from polarization ones.

We solve Eqs. (7) for L=4, $C_{11}=C_{00}$, and for different CW input conditions, i.e. different modal repartition $\{F_1(z=0),F_2(z=0)\}$, corresponding to an uniform coverage of the modal Poincaré sphere by $S^{(m)}(z=0)$, as depicted in Fig. 45a. We finally plot the corresponding output $S^{(m)}(z=L)$ (Figs. 45b, 46b) when the system has relaxed towards a stable stationary state of Eq. (7).

In Fig. 45b we observe that, for $C_{01}= C_{00}/1.75=C_{11}/1.75$, a strong attraction is observed towards two distinct points of the sphere. Most important, all the vectors $S^{(m)}(z=L)$ lie close to the circle which corresponds to $S_3^{(m)}=0$, that is to say $|F_1|^2-|F_2|^2=0$. This means that whatever the input values of $F_1(z=0)$ and $F_2(z=0)$, at the output of the system an equipartition of the energy among the two modes is observed, i.e. $|F_1|^2\approx|F_2|^2$, in a similar way than in the *bistable* regime of the Omnipolarizer. The histogram of the ratio $r = |F_1|^2/(|F_1|^2+|F_2|^2)$ in Fig. 45c confirms the modal equipartition: at the fiber input *r* is uniformly distributed between 0 and 1 (not shown), whereas at the fiber output, more than 80% of the occurrences lies around r=0.5.

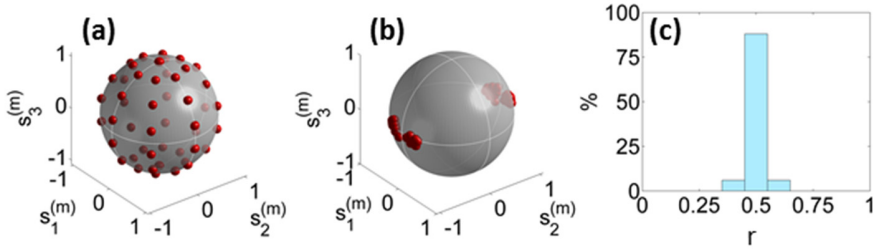

Fig. 45. (a) and (b) Input and output distribution of the modal Stokes vector $S^{(m)}$ when L=4 and $C_{00}=C_{11}=1.75C_{01}$. (c) Histogram of *r* at the fiber output: note that the central bin, corresponding to the range $0.45<r<0.55$, represents more than 80% of the total area of the histogram.

If we now reduce the intermodal nonlinear coupling C_{01} so that $C_{01}=C_{00}/3.5=C_{11}/3.5$, then the output modal equipartition is less efficient, as it is evident from Figs. 46 b&c. This is not surprising, as the strength of the energy exchange between the two fiber modes is proportional to C_{01}: in the limit case of $C_{01}=0$ no modal energy exchange occurs. As a result, we can observe in Fig. 46c that the effect of energy equipartition is almost annihilated in output of the fiber.

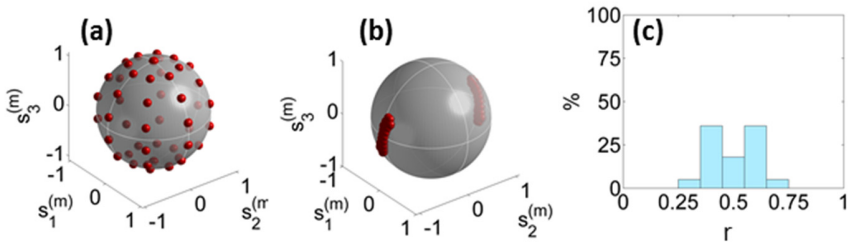

Fig. 46. (a) Same as in Fig. 45 but when $C_{00}=C_{11}=3.5C_{01}$. Note that *r* is not strongly distributed around 0.5 as in Fig. 45c, which is indicative of a weaker equipartition effect.

We point out that coefficients C_{00}, C_{11} and C_{01} can be adjusted over a wide range of values by means of an appropriate fiber design [122-125]. Therefore the two cases here analyzed, that is $C_{00}=C_{11}=1.75C_{01}$ and $C_{00}=C_{11}=3.5C_{01}$, are obtained for quite realistic fiber designs. It turns out that, in a strong nonlinear regime a bimodal fiber could be employed to achieve a truly efficient all-optical equipartition of energy among the two modes, whatever their input energy distribution is. Moreover, as in the Omnipolarizer, a reflective coefficient larger than 1, by means of a multimode amplified loop, should allow to completely trap the output energy in a single spatial mode. From a general point of view, many other applications may be envisaged by exploiting the propagation of multiple modes, especially for SDM and laser technologies.

XIII. CONCLUSIONS ON THE SELF-INDUCED REPOLARIZATION EFFECT

In this chapter, we have reviewed our theoretical, numerical and experimental works dealing with the self-induced repolarization process of light in optical fibers, within a device called Omnipolarizer. The principle of operation is based on a counter-propagating cross-polarization interaction between a forward propagating signal and its backward replica generated at the fiber end by means of a reflective element. This self-repolarization effect finds its origin in the capability of a single-mode system composed of two nonlinearly coupled counter-propagating waves to relax towards a reciprocal nonlinear birefringent steady state. From a general rule of thumb, we have found that this final stationary regime mainly corresponds to a more or less direct spatio-temporal trajectory leading to co-rotating circular SOPs, while satisfying the boundary

conditions imposed at both ends of the system. Depending on the reflective coefficient imposed at the mirror side, we have identified three distinct working regimes, namely the bistable regime, the alignment regime as well as a chaotic or scrambling regime. All of these configurations have been deeply investigated numerically and experimentally, providing a very good agreement between our experimental observations and numerical predictions based on a simple vectorial model of coupled nonlinear Schrödinger equations. Based on these fundamental observations, we have designed and exploited a compact prototype of Omnipolarizer to demonstrate several proof-of-concept experiments. Among them, we have especially exploited this device in order to self-repolarize a 40-Gbit/s RZ OOK signal. Depending on the power ratio between the two counter-propagating waves, we have first been able to track the output SOP of an incident polarization scrambled 40-Gbit/s signal in such a way to align its SOP on a single state, thus enabling a polarization-independent error-free reception. Moreover, for a fixed reflection coefficient just below unity, we have observed the repolarization of light along two orthogonal output SOPs. The SOP at the output of the Omnipolarizer is therefore simply fixed by the sign of the ellipticity of the input signal. Indeed, experimental recordings of the 40-Gbit/s eye-diagrams confirm the binary nature of the output SOP along two orthogonal channels with an extinction ratio higher than 20 dB. This bistable regime and associated hysteresis cycle properties have been then exploited in order to design an all-optical polarization based flip-flop memory and switching device that enables us to route 10-Gbit/s data packets on demand along two orthogonal polarization channels without noticeable degradations. We later explored the chaotic regime of the Omnipolarizer and demonstrated that this regime can be used as an all-optical nondeterministic scrambler for telecom applications as well as a genuine source of chaos for random numbers generation. A fascinating physical aspect of the Omnipolarizer has been also highlighted so as to demonstrate a polarization-based temporal tunneling effect. More specifically, the local coupling induced by the cross-polarization interaction between the two counter-propagating waves enables to instantaneously transpose a polarization information onto the reflected signal, long before the expected time-of-flight induced by the usual round-trip within the fiber. Finally, in the last section of this chapter, we have presented the generalization of the concept of self-induced attraction process to the case of modal attraction in a bimodal few mode fibers. In conclusion, after 10 years of research dedicated to the polarization attraction process, involving 2 Phds students, several postdocs under my supervision and collaboration with the group of D. Sugny, we have published close to 20 manuscripts dealing with this specific topic, as well as several invited talks and postdeadline papers.

XIV. ONGOING PERSPECTIVES

A. Honey, I shrunk the data

Our world today is flooded of digital data. Every day, every second, an incommensurable amount of bytes are generated, transmitted, exchanged, copied and stored by billions of networks users, thus creating a super-giant ocean of information. As a consequence, dealing with such a data traffic expansion will require new approaches for the development of future telecommunication optical networks in order to avoid a potential "Big Data Crash Overflow." One of our outlooks is to demonstrate a novel all-optical functionality enabling a temporal squeezing of optical data in such a way to compress the time-scale of an incident signal [126-127]. Here, the principle of operation is based on the transient regime of the counter-propagating cross-polarization interaction described above and enabling to temporally squeeze optical data by several orders of magnitude. This effect has been first described in the 90s in terms of four-wave mixing in ref. [128-129].

More precisely, as described in the following schematic diagrams of Figs. 47 (a-e), to temporally squeeze an incident signal, the data to compress (in orange, here represented by 50 ns pulses) are injected into a step-index birefringent fiber along two polarization axes. In opposite direction, a short readout pulse (in green), injected along the slow axis, is then coupled into the fibre. When both signals collide and overlap, a new pulse can be generated on the fast axis through this four-wave mixing interaction. The key idea is to carefully manage the differential group delay (walk-off) between both modes of propagation in order to efficiently separate the resulting signal between each bit of information so as to generate a high-quality

compressed replica of the data stream. Rough estimations reveal that several Watts peak-power are required to get a mw level of output compressed signal. Moreover, with a typical relative index difference of 10^{-4}, leading to a differential group delay of the order of 1 ps/m, we should be able to compress optical data by 3 orders of magnitude. In fact the temporal compression factor M can be easily estimated by means of the following expression:

$$M = \frac{2n_s}{\Delta n} \tag{8}$$

With n_s the index of the slow axis and Δn the index difference between both axes. For a typical value of $\Delta n = 6.10^{-4}$, M can be as high as 5.10^3., which leads to the compression of Mbit/s signals into Gbit/s replica or Gbit/s to Tbit/s data compression.

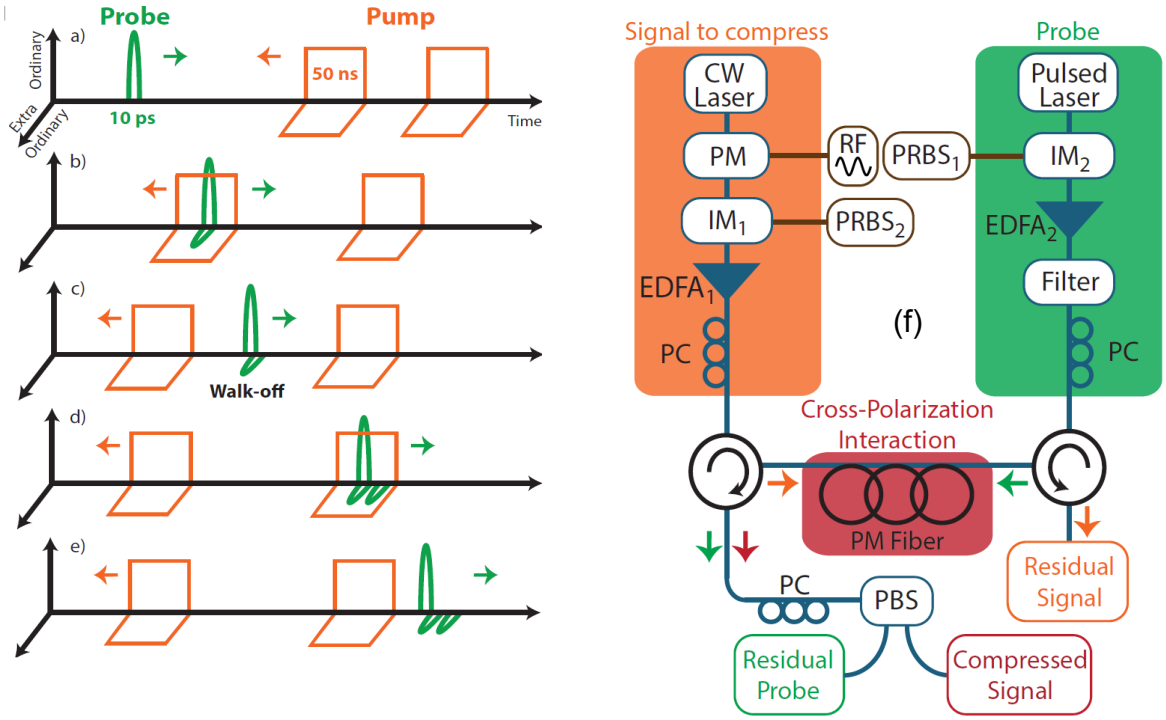

Fig. 47 (a-e) Principle of operation of the temporal data compression device based on counter-propagating waves. The data to compress are depicted in orange solid lines and the resulting compressed signal is displayed in green (f) Experimental setup. PM, polarization maintaining fiber; PRBS, pseudo random bit sequence generator; PC, polarization controller; IM, intensity modulator; PM, phase modulator; EDFA, erbium doped fiber amplifier; PBS, polarization beam splitter.

In order to provide a first proof-of-principle of this temporal compression process, we have implemented the experimental setup depicted in Fig. 47f. A 105-m long polarization-maintaining (PM) optical fiber is here used as nonlinear Kerr medium. The major parameter is here the walk-off in between both principal axes of the PM fiber which has been measured to 2.2 ps/m. Two optical circulators are implemented at each side of the fiber in order to both inject and extract the pump and the probe waves. The pump corresponds to a Mbit/s 50-ns pulse sequence generated from a continuous wave laser centered around 1550 nm and modulated by means of a Mach-Zehnder modulator driven by a pulse pattern generator. To avoid Brillouin back scattering, the pump wave is also phase modulated thanks to a 100-MHz RF signal. A polarization controller is used to adjust the input SOP of the pump beam to equally excite both principal axes of the fiber under test.

The probe wave is generated from a Calmar pulsed laser at a repetition rate of 10 GHz. The repetition rate of the laser is then decreased down to 2 MHz in order to be synchronized with the incident pump sequence. A series of EDFAs are then used to reach an efficient nonlinear FWM interaction in the PM fibre, typically: 10 W peak-power for the read out pulse and pump wave. At the output of the system, a PBS is used to separate the temporally compressed replica of the pump sequence from the residual read out pulse.

One example of data compression is presented in Fig. 48. Here, a data sequence of 10 bits are encoded on the pump wave at a repetition rate of 10 Mbit/s with a return-to-zero format made of 50-n pulses (Fig 48a). The peak power is estimated to 6 W and the polarization of the pump wave is aligned at 45° of the PM fiber axes. At the opposite end of the fiber, the read out pulse (close to 10 ps at the fiber input) are first injected on the slow axis of the PM fiber. Fig. 48b depicts the resulting compressed replica detected at the output of the fiber owing to a 50-GHz bandwidth sampling oscilloscope. As expected, a temporally compressed replica of the counter-propagating pump data sequence is then generated on the fast axis of the PM fiber. The repetition rate of this compressed sequence is close to 40 Gbit/s with optical pulse width below 11 ps (limited here by the bandwidth in detection). It corresponds to a compression factor M of 4300 which is close to the theoretical value obtained for this PM fiber near 4500 owing to Eq. (8). Moreover, we can observe that the numerical simulations, represented with dashed-lines in Figs. 48 b&c and based on a system of two coupled NLS propagating in a birefringent fiber well reproduce the dynamics of this effect.

Furthermore, as shown in Fig. 48c, this temporal compression technique is also able to provide a time reversal replica of the initial pump sequence. Indeed, as shown in Fig. 48c, if the polarization of the probe pulse is then aligned on the fast axis of the PM fiber, the generated pulses on the other axis will travel slower than the probe. In this way, every new generated pulses will be delayed compared to the previous one. Consequently, the data sequence will be temporally reversed in addition to be compressed.

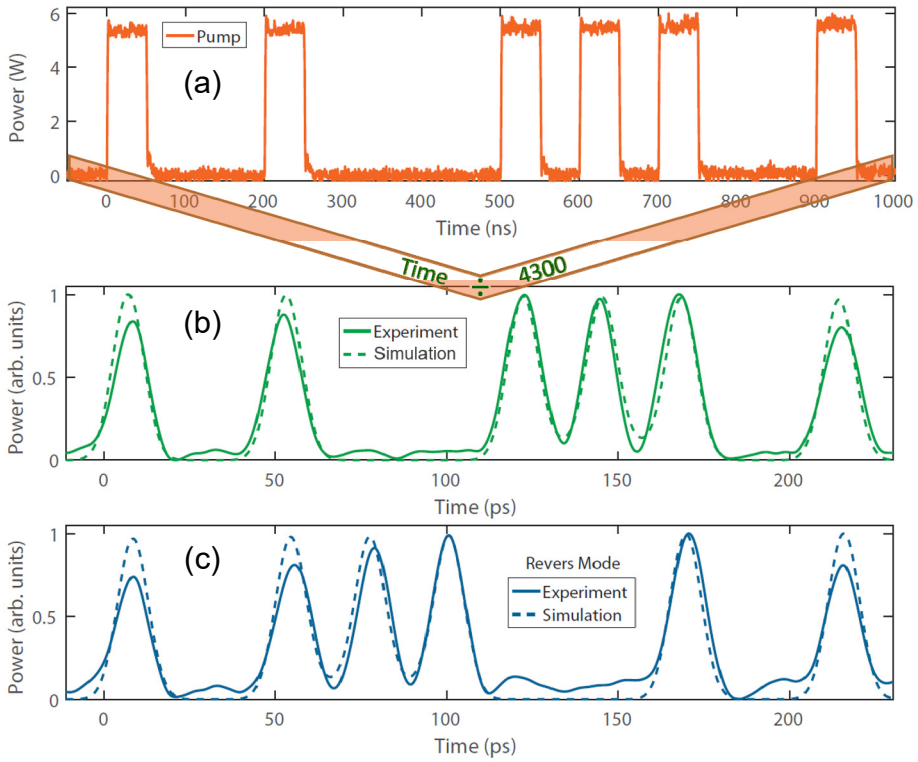

Fig. 48. Example of experimental demonstration of temporal data compression. (a) Pump sequence (ns time scale). (b) Compressed signal (ps scale) obtained by injecting the read out probe pulse on the slow axis of the PM fibre. (c) Same as (b) but when the read out probe pulse is injected on the fast axis of the PM fibre. The sequence is then reversed. In (a) and (c) the dashed lines indicate the numerical simulation results.

B. Imbricated Omnipolarizer

An interesting test to be done in order to improve the efficiency of the Omnipolarizer could be to couple two Omnipolarizers with one master and one slave implemented directly into the feedback loop. In such a system, the symmetry of the system should be broken and this imbricated Omnipolarizer should be characterized by only one pool of attraction (none bistability). Moreover, the threshold of power involved into the alignment regime should be also greatly reduced. The following figure described the principle of operation which could be quickly tested.

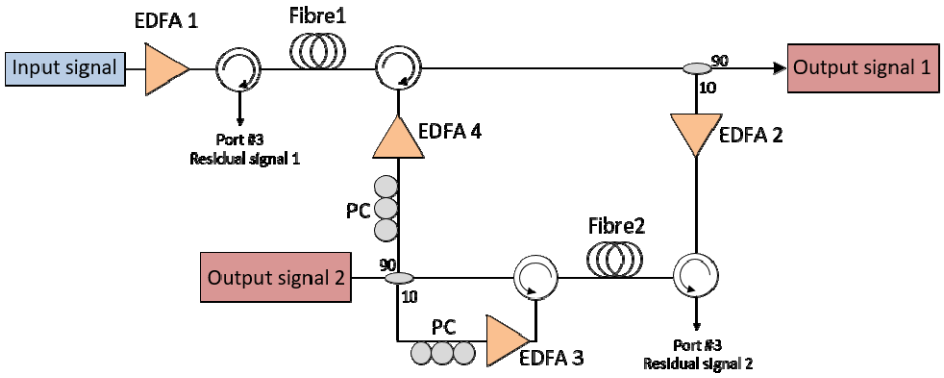

Fig. 49. Principle of operation of the imbricated Omnipolarizer.

C. Spatial Omnipolarizer

As already mentioned in the section XII of this manuscript, one of the future perspective could be to generalize the concept of self-polarization attraction to higher degrees of freedom and to demonstrate the general concept of multi-dimensional condensation of light in multimode fibers thanks to a counter-propagating interaction. On these basis, several modal functionalities could be developed for spatial division multiplexing applications [120] such as all-optical mode cleaner, crosstalk-free transmission as well as spatial routing and switching operations. In this context, we have recently tried to demonstrate the self-attraction polarization process in a bimodal optical fibre. The following schematic diagram illustrates the concept of Omnipolarizer in a bimodal fibre. In this first test, the experiment relies on a 6-km long span of commercially available bimodal fibre from *ofs* (at 1550 nm), in which a polarization scrambled signal is injected with an arbitrary ratio of energy distributed among the LP_{01} and LP_{11} modes. This incident signal then nonlinearly interacts with its own LP_{01} counter-propagating replica generated at the fibre end by means of an amplified reflective loop multimode setup made of a spatial demultiplexer, circulator and EDFA. For this first fundamental study, the input signal consists of the polarization-scrambled 100-GHz incoherent wave described above centered on 1550 nm. The input signal is then polarization scrambled and amplified at an average power of 28 dBm before injecting with an arbitrary spatial mode distribution. Figure 50b displays the experimental measurements of both LP_{01} and LP_{11} output SOPs. First-of-all, despite the fact that the polarization state of the injected bimodal signal is completely scrambled at the input of the fibre (first sphere), the output signal wave exhibits a polarization condensation process for both modes, in which it relaxes to a stationary state for each spatial mode, independently of the input SOP. As in the single mode configuration, this process first occurs around two pools of attraction (bistability) for a feedback power of 26 dBm and then, on a single state for a backward power exceeding 30 dBm. These preliminary results are encouraging but have to be carefully checked and completed. Indeed, it corresponds to a single test made by our last Phd, which unfortunately did not get enough time to go deeper into the analysis. In fact, several questions are still opened. The first one is the output Poincaré sphere recorded for the output LP_{11} in the bistable regime. Indeed, the two pools of SOP attraction do not appear orthogonal at all, which breaks the symmetry of the problem and thus is highly questionable. The second issue is the impact of the power ratio

between the two modes as well as the decorrelation process occurring between the two modes due to the modal dispersion effect. Finally, could we able to reproduce these results by injecting the feedback signal into the LP_{11} rather than in the fundamental mode, and generalize this concept to a higher number of modes?

More generally, as already envisioned in the pioneer work of Dijon in 2005 in a 2-m long bimodal fibre [58], are we able to generalize the concept of self-polarization to a multi-dimensional case for which an arbitrary polarized and distribution of energy among the spatial modes injected into a highly multimode fibre, can be transformed into a pure polarized single-mode state, without any loss of energy? Since this effect is a generalization of the self-repolarization phenomenon, we could anticipate here that the system of two counter-propagating spatial waves has to relax towards a stationary regime for which the mutual cross nonlinear contribution of the refractive index provides a reciprocal steady-state for both waves. This concept has been submitted in a grant proposal for the ERC consolidator but unfortunately, was rejected twice after the oral in Brussels.

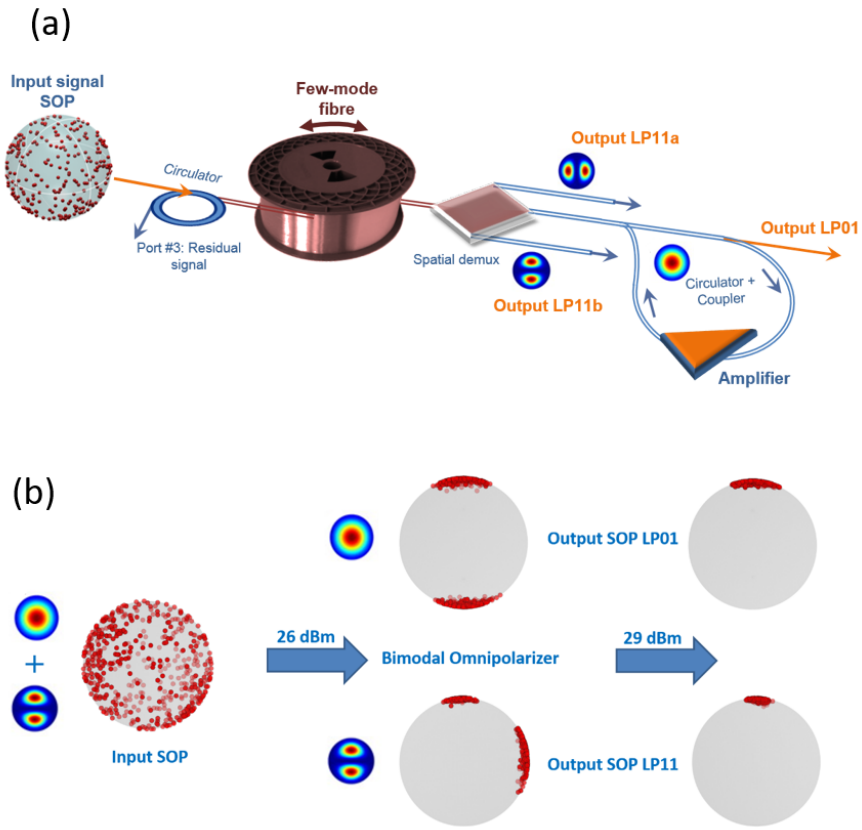

Fig. 50. (a) Schematic diagram of the bimodal Omnipolarizer (b) State-of-polarization on the Poincaré sphere at the input of the fibre and output of the system for the LP_{01} and LP_{11} modes, respectively.

PERSONAL CONCLUSIONS

During these 15 *first* years of research in the Laboratoire Interdisciplinaire Carnot de Bourgogne (ICB) of Dijon in the Solitons, Lasers and Optical Communications group (SLCO), I have exploited the richness and the beauty of linear and nonlinear effects taking place in optical fibers in order to demonstrate novel physical phenomena. As a perpetual leitmotiv, I have also tried to keep a good balance between fundamental science and applications, in particular in the field of optical communications. Following this rule of thumb, I have been involved or have developed numerous subjects of research dealing with nonlinear fiber optics such as optical regeneration, pulse source design, polarization processing, supercontinuum generation, parametric amplification, Kerr resonators, dispersive shock waves, rogue waves, polarization domain walls, inter-modal four wave mixing as well as modulational instability to name a few. The diversity of those different topics helps me to acquire a global overview of the state-of-the-art dealing with optical fibers and more generally in guided optics. Filled with curiosity and the continuous desire to test and develop new concepts, all these ways of research have also fed my understanding, skills and know-hows in the design of more or less complex fiber systems. This is probably the reason why my contributions were mainly experimental so far, though often supported by numerical simulations. The direct consequence of this palette of subjects was definitively the opportunity to meet a lot of brilliant guys during conferences I attended, meetings, workshops and get drink together…cheers! As a result, it is not so surprising that many of my publications have been shared by more than 150 different coauthors. Nevertheless, among these coauthors, mainly are academic researchers and unfortunately only a few are industrial partners, which somehow translates the fact that I did not fully succeed in bridging the gap in between fundamental and applicative science so far. Furthermore, mobility and fruitful collaborations gave me the opportunity to travel all over the world (by the way, generating an unmentionable shameful carbon footprint) and in particular to attend administrative retreats at the University of Auckland in the team of M. Erkintalo and S. Coen. I encourage here any reader, who has the opportunity to get out of his Lab, to accomplish such sabbatical stays. Indeed, working on a complementary topic, in a different politico-administrative system, just like a pure postdoc fellow has no price. In fact, it greatly helps to keep our mind open, whilst looking from a different perspective our own system of research and its global impact. Along these 15 years of research, I was granted with at least 2.5 M€ and supervised a dozen of people including phds and postdocs, which allows me to lead a small group of research, in particular during my ERC starting grant. With more than 110 publications, 4 patents and several invited conferences or postdeadline papers, the outcome is not so bad, close to 30k€ full cost per publication in a simplest approach… However, beyond these contributions to a universal scientific knowledge (which represents our primary job, and has to be sometimes recalled), the dark side still remains the weak impact and connections between my research activities and industrial partners. Indeed, despite the development of two full-integrated prototypes and several attempts of business development, our proposed solutions do not seem to have matched with any market needs, at least of sufficient size. I mostly attribute this unsuccess to the fact that our stories always start from an open scientific question rather than a more pragmatic industrial issue. Regarding this point, the French system and its policy of research could be strongly improved. But unfortunately, the current trend seems to follow a totally different path, with the multiplication of novel agencies, administrative structures, federal grants, sub-call of projects and so on… Anyway, it is also true that, due to our quest of novelty and scientific beauty, our discoveries often appear too complex and mainly rely on nonlinear effects in optical fibers, which has to be said, is nowadays a quite aging field of research. Indeed, even if photonics is almost everywhere in our daily life, we should confess that for nonlinear fiber optics, only a small part of discoveries have really found a deep societal impact. For instance in optical communications, despite the exponential growing demand of bandwidth, mainly dedicated to video on demand, (anti)social networks or pxxn traffics, the advance of coherent detection and digital signal processing have move the main issues from the physical fiber optics layer to numerical communications, leading behind decades of research dedicated to nonlinear solutions (except amplification issues). So what's next in the forthcoming 15 years…? For sure, integrated photonics and in particular Kerr resonators is clearly nowadays hot topics of research, giving rise to a plethora of possible applications.

However, one has to benefit from highly expensive state-of-the-art manufacturing facilities and this field is by far highly competitive, so could only be based on a collaboration network. Nevertheless, studies in fiber based macro-resonators, which are governed by the same physics, are still attractive in order to capture some fundamental effects, such as non-reciprocal steady-states and broken symmetry phenomena. The design and development of novel optical sources, in particular in the Mid-IR sounds also as a possible way of breakthrough discoveries. Finally, but in a non-exhaustive manner, multimode dynamics in optical fibers and associated potential applications in optical communications, lasers, imaging or sensing also arises as a promising way of research.

ACKNOWLEDGEMENTS

I thank P. Morin* (PhD), P. Y. Bony* (PhD), M. Guasoni* (Postdoc), G. Marin* (PhD), N. Berti* (Postdoc), J. Morosi* (PhD invited 4 months), A. Akrout* (Postdoc), E. Assémat (PhD), A. Fusaro (PhD), S. Pitois, A. Picozzi, G. Millot, D. Sugny, H. R. Jauslin, S. Wabnitz, S. Pernot, B. Sinardet, V. Tissot, K. Hammani, C. Finot and B. Kibler and all the people who contribute to this work.
This research was funded by the European Research Council under Grant Agreement 306633, ERC PETAL. https://www.facebook.com/petal.inside. We also thank the financial support of the Conseil Régional de Bourgogne Franche-Comté, l'agence nationale de la recherche (ANR), la délégation régionale à la recherche et à la technologie (DRRT) ainsi que le fond européen de développement régional (FEDER).

**People under my supervision.*

REFERENCES

1. T. Geisler, "Low PMD Transmission Fibres," in *European Conference on Optical Communications ECOC 2006*, paper Mo.3.3.1, 2006.
2. A. J. Barlow, J. J. Ramskov-Hansen, and D. N. Payne "Birefringence and polarization mode-dispersion in spun singlemode fibers," *Appl. Opt.*, vol. 20, pp. 2962-2968, 1981.
3. M. J. Li and D. A. Nolan, "Fiber spin-profile designs for producing fibers with low polarization mode dispersion," *Opt. Lett.*, vol. 23, pp. 1659-1661, 1998.
4. L. Palmieri, "Polarization Properties of Spun Single-Mode Fibers," *IEEE J. Lightw. Technol.*, vol. 24, pp. 4075-4088, 2006.
5. M. Boroditsky, M. Brodsky, N. J. Frigo, P. Magill, and H. Rosenfeldt, "Polarization dynamics in installed fiber optic systems" *IEEE LEOS Annual Meeting Conference Proceedings (LEOS)*, pp. 413–414, 2005.
6. P. M. Krummrich and K. Kotten, "Extremely fast (microsecond scale) polarization changes in high speed long hail WDM transmission systems," in Proc. of Optical Fiber Commun. Conference, Los Angeles, USA, 2004.
7. S. C. Rashleigh, "Origins and control of polarization effect in single-mode fibers," *IEEE J. Lightw. Technol*., vol. 1, pp. 312–331, 1983.
8. R. Ulrich and A. Simon, "Polarization optics of twisted single-mode fibers*," Appl. Opt*., vol. 18, pp. 2241–2251, 1979.
9. A. Simon and R. Ulrich, "Evolution of polarization along a single-mode fiber," *Appl. Phys. Lett*., vol. 31, pp. 517–520, 1977.
10. A. Galtarossa, L. Palmieri, M. Schiano, and T. Tambosso, "Measurement of birefringence correlation length in long single-mode fibers," *Opt. Lett*., vol. 26, pp. 962–964, 2001.
11. C. D. Poole, and R. E. Wagner, "Phenomenological approach to polarization dispersion in long single-mode fibers," *Electron. Lett*., vol. 22, pp. 1029–1030, 1986.
12. A. Galtarossa and C. R. Menyuk, Eds., Polarization Mode Dispersion. New York: Springer-Verlag, 2005.
13. J. Garnier, J. Fatome, and G. Le Meur, "Statistical analysis of pulse propagation driven by polarization-mode dispersion," *J. Opt. Soc. Am. B*, vol. 19, pp. 1968–1977, 2002.
14. P. K. A. Wai and C. R. Menyuk, "Polarization mode dispersion, decorrelation, and diffusion in optical fibers with randomly varying birefringence," *IEEE J. Lightw. Technol*., vol. 14, pp. 148–157, 1996.
15. A. Galtarossa, L. Palmieri, and L. Schenato, "Simplified phenomenological model for randomly birefringent strongly spun fibers," *Opt. Lett*., vol. 31, pp. 2275-2277, 2006.
16. N. Gisin, and B. Huttner, "Combined effects of polarization mode dispersion and polarization dependent losses in optical fibers," *Opt. Commun.,* vol. 142, pp. 119–125, 1997.
17. D. Sperti, P. Serena and A. Bononi, "Optical solutions to improve PDM-QPSK resilience against cross-channel nonlinearities: A Comparison," *IEEE Photon. Technol. Lett.*, vol. 23, pp.667-669, 2011.
18. L. F. Mollenauer, J. P. Gordon, and F. Heismann, "Polarization scattering by soliton–soliton collisions," *Opt. Lett.*, vol. 20, pp. 2060-2062, 1995.
19. J. Renaudier, G. Charlet, M. Salsi, O. B. Pardo, H. Mardoyan, P. Tran, and S. Bigo, "Linear Fiber Impairments Mitigation of 40-Gbit/s Polarization-Multiplexed QPSK by Digital Processing in a Coherent Receiver," *IEEE J. Lightwave Technol*., vol. 26, pp. 36-42, 2008.
20. G. Charlet "Coherent detection associated with digital signal processing for fiber optics communications," *C. R. Physique*, vol. 9, pp. 1012-1030, 2008.
21. G. Charlet, J. Renaudier, M. Salsi, H. Mardoyan, P. Tran, and S. Bigo, "Efficient Mitigation of Fiber Impairments in an Ultra-Long Haul Transmission of 40Gbit/s Polarization-Multiplexed Data, by Digital Processing in a Coherent Receiver," *in Optical Fiber Communication Conference and Exposition*, paper PDP17, 2007.
22. J. Hansryd, P. A. Andrekson, M. Westlund, J. Li, and P. Hedekvist, "Fibre-based optical parametric amplifiers and their applications," *IEEE J. Sel. Top. Quantum Electron*., vol. 8, pp. 506-520, 2002.
23. K. Inoue, "Polarization independent wavelength conversion using fiber four-wave mixing with two orthogonal pump lights of different frequencies," IEEE J. Lightwave Technol., vol. 12, pp. 1916–1920, 1994.
24. K. K. Y. Wong, M. E. Marhic, K. Uesaka and Leonid G., Kazovsky, "Polarization-independent one-pump fiber-optical parametric amplifier," *IEEE Photon Technol Lett*., vol. 14, pp. 1506-1508, 2002.
25. H. Fukuda, K. Yamada, T.Tsuchizawa, T. Watanabe, H. Shinojima, and S. Itabashi, "Silicon photonic circuit with polarization diversity," Opt. Express, vol. 16, pp. 4872-4880, 2008.
26. M. Martinelli, P. Martelli, and S. M. Pietralunga, "Polarization stabilization in optical communications systems," *IEEE J. Lightw. Technol.*, vol. 24, pp. 4172–4183, 2006.
27. B. Koch, R. Noe, D. Sandel, and V. Vitali Mirvoda, "Versatile endless optical polarization controller/tracker/demultiplexer," *Opt. Express* vol. 22, pp. 8259–8276, 2014.
28. B. Koch, R. Noe, V. Mirvoda, H. Griesser, S. Bayer, and H. Wernz "Record 59-krad/s Polarization Tracking in 112-Gb/s 640-km PDM-RZ-DQPSK Transmission," *IEEE Photonics Technol. Lett*., vol. 22, pp. 1407–1409, 2010.
29. W. H. J. Aarts and G. Khoe, "New endless polarization control method using three fiber squeezers," IEEE J. Lightwave Technol., vol. 7, pp. 1033-1043, 1989.
30. B. Koch, R. Noé, V. Mirvoda and D. and Sandel, "100-krad/s endless polarisation tracking with miniaturised module card," *Electron. Lett*., vol. 47, pp. 813-814, 2011.
31. https://www.novoptel.de.
32. https://newridgetech.com/
33. E. Heebner, R. S. Bennink, R. W. Boyd, and R. A. Fisher "Conversion of unpolarized light to polarized light with greater than 50% efficiency by photorefractive two-beam coupling," *Opt. Lett*., vol. **25**, pp. 257-259, 2000.
34. M. Martinelli, M. Cirigliano, M. Ferrario, L. Marazzi, and P. Martelli, "Evidence of Raman-induced polarization pulling," *Opt. Express*, vol. 17, pp. 947-955, 2009.
35. L. Ursini, M. Santagiustina, and L. Palmieri, "Raman Nonlinear Polarization Pulling in the Pump Depleted Regime in Randomly Birefringent Fibers," *IEEE Photon. Technol. Lett.*, vol. 23, pp. 1041-1135, 2011.

36. A. Galtarossa, L. Palmieri, M. Santagiustina, L. Schenato, and L. Ursini, "Polarized Brillouin Amplification in Randomly Birefringent and Unidirectionally Spun Fibers," *IEEE Photon. Technol. Lett*., vol. 20, pp. 1420-1422, 2008.
37. N. J. Muga, M. F. S. Ferreira, and A. N. Pinto "Broadband polarization pulling using Raman amplification," *Opt. Express*, vol. 19, pp. 18707-18712, 2011.
38. V. Kozlov, J. Nuno, J. D. Ania-Castanon and S. Wabnitz, "Theoretical study of optical fiber Raman polarizers with counterpropagating beams," *IEEE J. Lightwave Technol*., Vol. 29, pp. 341-347, 2011.
39. L. Thevenaz, A. Zadok, A. Eyal and M. Tur, "All-optical polarization control through Brillouin amplification", in *Optical Fiber Communication Conference*, OFC'08, paper OML7 (2008).
40. Z. Shmilovitch, N. Primerov, A. Zadok, A. Eyal, S. Chin, L. Thevenaz, and M. Tur "Dual-pump push-pull polarization control using stimulated Brillouin scattering," *Opt. Express*, vol. 19, pp. 25873-25880, 2011.
41. B. Stiller, P. Morin, D. M. Nguyen, J. Fatome, S. Pitois, E. Lantz, H. Maillotte, C. R. Menyuk, and T. Sylvestre, "Demonstration of polarization pulling using a fiber-optic parametric amplifier," *Opt. Express*, vol. 20, pp. 27248-27253, 2012.
42. M. Guasoni, V. Kozlov, and S. Wabnitz, "Theory of polarization attraction in parametric amplifiers based on telecommunication fibers," *J. Opt. Soc. Am. B*, vol. 29, pp. 2710-2720, 2012.
43. S. Pitois and M. Haelterman, "Optical fiber polarization funnel," Nonlinear Guided Waves and Their Applications NLGW'01, paper MC79-1, 2001.
44. J. Fatome, S. Pitois, P. Morin, and G. Millot, "Observation of light-by-light polarization control and stabilization in optical fibre for telecommunication applications," *Opt. Express*, vol. 18, pp. 15311-15317, 2010.
45. J. Fatome, P. Morin, S. Pitois and G. Millot, "Light-by-Light Polarization Control of 10-Gb/s RZ and NRZ Telecommunication Signals," *IEEE J. Sel. Top. Quantum Electron*, vol. 18, pp.621-628, 2012.
46. V. V. Kozlov, J. Nuno and S. Wabnitz, "Theory of lossless polarization attraction in telecommunication fibers," *J. Opt. Soc. Am. B*, vol. 28, pp. 100-108, 2011.
47. K. Turitsyn and S. Wabnitz, "Stability analysis of polarization attraction in optical fibers," *Opt. Commun*., vol. 307, pp. 62-66, 2013.
48. D. Sugny, A. Picozzi, S. Lagrange and H. R. Jauslin, "Role of singular tori in the dynamics of spatiotemporal nonlinear wave systems," *Phys. Rev. Lett.* vol. 103, 034102, 2009.
49. V. V. Kozlov, J. Fatome, P. Morin, S. Pitois, G. Millot and S. Wabnitz, "Nonlinear repolarization dynamics in optical fibers: transient polarization attraction," *J. Opt. Soc. Am. B*, vol. 28, pp. 1782-1791, 2011.
50. E. Assémat, A. Picozzi, H. R. Jauslin and D. Sugny, "Hamiltonian tools for the analysis of optical polarization control," *J. Opt. Soc. Am. B*, vol. 29, pp. 559-571, 2012.
51. E. Assémat, D. Dargent, A. Picozzi, H. R. Jauslin and D. Sugny, "Polarization control in spun and telecommunication optical fibers," *Opt. Lett*., vol. 36, pp. 4038-4040, 2011.
52. P. Morin, J. Fatome, C. Finot, S. Pitois, R. Claveau and G. Millot, "All-optical nonlinear processing of both polarization state and intensity profile for 40 Gbit/s regeneration applications," *Opt. Express*, vol. 19, pp. 17158-17166, 2011.
53. M. Barozzi and A. Vannucci "Lossless polarization attraction of telecom signals: application to all-optical OSNR enhancement," *J. Opt. Soc. Am. B*, vol. 31, pp. 2712-2720, 2014.
54. M. Barozzi and A. Vannucci, "Dynamics of lossless polarization attraction," *Photon. Res.* Vol. **3**, pp. 229-233, 2015.
55. V. Costa Ribeiro, R. S. Luis, J. M. D. Mendinueta, B. J. Puttnam, A. Shahpari, N. J. C. Muga, M. Lima, S. Shinada, N. Wada and A. Teixeira "All-Optical Packet Alignment Using Polarization Attraction Effect," *IEEE Photon. Technol. Lett*., vol. 27, pp. 541-544, 2015.
56. A. DeLong, W. Astar, T. Mahmood and G. M. Carter, "Polarization attraction of 10-Gb/s NRZ-BPSK signal in a highly nonlinear fiber," *Opt. Express* vol. 25, pp. 25625-25636, 2017.
57. P. Morin, S. Pitois, and J. Fatome, "Simultaneous polarization attraction and Raman amplification of a light beam in optical fibers," *J. Opt. Soc. Am. B*, vol. 29, pp. 2046-2052, 2012.
58. S. Pitois, A. Picozzi, G. Millot, H.R. Jauslin, M. Haelterman, "Polarization and modal attractors in conservative counterpropagating four-wave interaction," *Europhys. Lett*., vol. 70, pp. 88-94, 2005.
59. J. Fatome, S. Pitois, P. Morin, D. Sugny, E. Assémat, A. Picozzi, H. R. Jauslin, G. Millot, V. V. Kozlov and S. Wabnitz, "A universal optical all-fiber omnipolarizer," *Sci. Rep*., vol. 2, 938, 2012.
60. P. Y. Bony, M. Guasoni, P. Morin, D. Sugny, A. Picozzi, H. Jauslin, S. Pitois and J. Fatome, "Temporal spying and concealing process in fibre-optic data transmission systems through polarization bypass," *Nat. Commun*., vol. 5, pp. 5:4678, 2014.
61. P.-Y. Bony, M. Guasoni, E. Assémat, S. Pitois, D. Sugny, A. Picozzi, H. R. Jauslin and J. Fatome, "Optical flip-flop memory and data packet switching operation based on polarization bistability in a telecomunnication optical fiber," *J. Opt. Soc. Am. B*, vol. 30, pp. 2318-2325, 2013.
62. M. Guasoni, P. Y. Bony, M. Gilles, A. Picozzi, and J. Fatome, "Fast and Chaotic Fiber-Based Nonlinear Polarization Scrambler," *IEEE J. Select. Topics in Quantum Electron.,* vol. 22, pp. 88-99, 2016.
63. J. Morosi, N. Berti, A. Akrout, A. Picozzi, M. Guasoni and J. Fatome, "Polarization chaos and random bit generation in nonlinear fiber optics induced by a time-delayed counter-propagating feedback loop," *Opt. Express,* vol. 26, pp. 845-858, 2018.
64. A. L. Gaeta, R. W. Boyd, J. R. Ackerhalt and P. W. Milonni, "Instabilities and chaos in the polarizations of counterpropagating light fields," *Phys. Rev. Lett.,* vol. 58, pp. 2432-2435, 1987.
65. D. J. Gauthier, M. S. Malcuit and a. R. Boyd, "Polarization Instabilities of Counterpropagating Laser Beams in Sodium Vapor," *Phys. Rev. Lett*., vol. 61, pp. 1828-1830, 1987.
66. D. J. Gauthier, M. S. Malcuit, A. L. Gaeta and R. W. Boyd, "Polarization bistability of counterpropagating laser beams," *Phys. Rev. Lett.*, vol. 64, pp. 1721-1724, 1990.
67. S. Trillo and S. Wabnitz, "Intermittent spatial chaos in the polarization of counterpropagating beams in a birefringent optical fiber," *Phys. Rev. A*, vol. 36, pp. 3881-3884, 1987.
68. M. V. Tratnik and J. E. Sipe, "Nonlinear polarization dynamics. II. Counterpropagating-beam equations: New simple solutions and the possibilities for chaos," *Phys. Rev. A*, vol. 35, pp. 2976-2988, 1987.
69. A. Fusaro, N. Berti, M. Guasoni, H. R. Jauslin, A. Picozzi, J. Fatome and D. Sugny, "Self-polarization effect in the middle point of an optical fiber," *Phys. Rev. A*, vol. 99, 043826, 2019.

70. A. Fusaro, N. Berti, M. Guasoni, H. R. Jauslin, A. Picozzi, J. Fatome and D. Sugny, "Self-organization of the state of polarization in the mid-point of telecommunication optical fiber," *J. Opt. Soc. Am. B*, accepted, 2019.
71. M. Guasoni, P. Morin, P.-Y. Bony, S. Wabnitz and J. Fatome, "Self-induced polarization tracking, tunneling effect and modal attraction in optical fiber," *Optics & Laser Technology*, vol. 80, pp. 247-259, 2016.
72. V. E. Zakharov and A. V. Mikhailov, "Polarization domains in nonlinear optics," *JETP Lett*., vol. 45, pp. 349-352, 1987.
73. S. Wabnitz and B. Daino, "Polarization domains and instabilities in nonlinear optical fibers," *Phys. Lett. A*, vol. 182, pp. 289-293, 1993.
74. S. Pitois, G. Millot, and S. Wabnitz, "Polarization domain wall solitons with counterpropagating laser beams," *Phys. Rev. Lett.*, vol. 81, pp. 1409-1412, 1998.
75. S. Pitois, G. Millot and S. Wabnitz, "Nonlinear polarization dynamics of counterpropagating waves in an isotropic optical fiber: theory and experiments," *J. Opt. Soc. Am. B*, vol. 18, pp. 432-443, 2001.
76. A. E. Kaplan, "Light-induced nonreciprocity, field invariants, and nonlinear eigenpolarizations," *Opt. Lett*., vol. 8, pp. 560-562, 1983.
77. S. Wabnitz and G. Gregori, "Symmetry-breaking and intrinsic polarization instability in degenerate four-wave mixing," *Opt. Commun*. Vol. 59, pp. 72-76, 1986.
78. A. L. Gaeta, R. W. Boyd, J. R. Ackerhalt and P. W. Milonni, "Instabilities and chaos in the polarization of counterpropagating light fields," *Phys. Rev. Lett*., vol. 58, pp. 2432-2435, 1987.
79. L. Del Bino, J. M. Silver, S. L. Stebbings, and P. Del'Haye, "Symmetry breaking of counter-propagating light in a nonlinear resonator," *Scientific Reports*, vol. 7, 43142, 2017.
80. F. Copie, M. T. M. Woodley, L. Del Bino, J. M. Silver, S. Zhang and P. Del'Haye, "Interplay of Polarization and Time-Reversal Symmetry Breaking in Synchronously Pumped Ring Resonators," *Phys. Rev. Lett*., vol. 122, 013905, 2019.
81. A. E. Kaplan and P. Meystre, "Enhancement of the Sagnac effect due to nonlinearly induced nonreciprocity," Optics Lett., vol. 6, pp. 590-592, 1981.
82. G. P. Agrawal, Nonlinear Fiber Optics, 4th ed., Academic Press, New York, 2007.
83. D. Y. Parpia, B. K. Tanner and D. G. Lord, "Direct optical observation of ferromagnetic domains," *Nature*, vol. 303, pp. 684-685, 1983.
84. A. M Kosevich, "Dynamical and topological solitons in ferromagnets and antiferromagnets," in Solitons, Elsevier, 1986.
85. V. V. Kozlov and S. Wabnitz, "Instability of optical solitons in the boundary value problem for a medium of finite extension," Lett. Math. Phys., vol. 96, pp. 405-413, 2011.
86. E. Assémat, A. Picozzi, H. R. Jauslin and D. Sugny, "Instabilities of optical solitons and Hamiltonian singular solutions in a medium of finite extension," *Phys Rev. A*, vol. 84, 013809, 2011.
87. M. Haelterman and A. P. Sheppard, "Vector soliton associated with polarization modulational instability in the normal-dispersion regime," *Phys. Rev. E*, vol. 49, 3389, 1994.
88. M. Gilles, P.-Y. Bony, J. Garnier, A. Picozzi, M. Guasoni and J. Fatome, "Polarization domain walls in optical fibres as topological bits for data transmission," *Nat. Photonics*, vol. 11, pp. 102-107, 2017.
89. J. Fatome, Y. Wang, B. Garbin, B. Kibler, A. Bendahmane, N. Berti, G. -. Oppo, F. Leo, S. G. Murdoch, M. Erkintalo and S. Coen, "Flip-Flop Polarization Domain Walls in a Kerr Resonator," *in Advanced Photonics NP 2018*, postdeadline paper JTu6F.2, 2018.
90. P. V. Mamyshev, "All-optical data regeneration based on self-phase modulation effect," in *ECOC'98*, pp. 475-476, 1998.
91. M. Matsumoto, "Fiber-Based All-Optical Signal Regeneration," *IEEE J. Sel. Top. Quant.*, vol. 18, pp. 738-752, 2012.
92. L. Provost, C. Finot, K. Mukasa, P. Petropoulos and D. J. Richardson, "Design scaling rules for 2R-Optical Self-Phase Modulation-based regenerators 2R regeneration," *Opt. Express*, vol. 15, pp. 5100-5113, 2007.
93. M. Matsumoto, "Performance Analysis and Comparison of Optical 3R Regenerators Utilizing Self-Phase Modulation in Fibers," *IEEE J. Lightw Technol.*, vol. 22, pp. 1472-1482, 2004.
94. A. Argyris, D. Syvridis, L. Larger, V. Annovazzi-Lodi, P. Colet, I. Fischer, J. García-Ojalvo, C. R. Mirasso, L. Pesquera and K. A. Shore, "Chaos-based communications at high bit rates using commercial fibre-optic links," *Nature*, vol. 438, pp. 343-346, 2005.
95. L. Keuninckx, M. C. Soriano, I. Fischer, C. R. Mirasso, R. M. Nguimdo and G. Van der Sande, "Encryption key distribution via chaos synchronization," *Sci. Rep*., vol. 7, 43428; doi: 10.1038/srep43428, 2017.
96. L. Larger and J. M. Dudley, "Optoelectronic chaos," *Nature*, vol. 465, pp. 41-42, 2010.
97. D. Sussillo, and L. F. Abbott, "Generating coherent patterns of activity from chaotic neural networks," *Neuron*, vol. 63, pp. 544-557, 2009.
98. W. H. J. Aarts, and G. Khoe, "New endless polarization control method using three fiber squeezers," *J. Lightwave Technol.*, vol. 7, pp. 1033-1043, 1989.
99. P. Boffi, M. Ferrario, L. Marazzi, P. Martelli, P. Parolari, A. Righetti, R. Siano, and M. Martinelli, "Stable 100-Gb/s POLMUX-DQPSK transmission with automatic polarization stabilization," *IEEE Photon. Technol. Lett.*, vol. 21, pp. 745-747, 2009.
100. Y. K. Lize, R. Gomma, R. Kashyap, L. Palmer, and A. E. Willner, "Fast all-fiber polarization scrambling using re-entrant Lefèvre controller," *Optics Commun*., vol. 279, pp. 50-52, 2007.
101. F. Heismann, "Compact electro-optic polarization scramblers for optically amplified lightwave systems," *J. Lightwave Technol*., vol. 14, pp. 1801-1814, 1996.
102. http://www.generalphotonics.com/index.php/product/pcd-104-polarization-scrambler/
103. https://agiltron.com/product/high-speed-polarization-scrambler/
104. https://www.novoptel.de/Scrambling/Scrambling_en.php
105. A. Uchida, K. Amano, M. Inoue, K. Hirano, S. Naito, H. Someya, I. Oowada, T. Kurashige, M. Shiki, S. Yoshimori, K. Yoshimura and P. Davis "Fast physical random bit generation with chaotic semiconductor lasers," *Nat. Photon.*, vol. 2, pp.728-732, 2008.
106. I. Kanter, Y. Aviad, I. Reidler, E. Cohen and M. Rosenbluh, "An optical ultrafast random bit generator," *Nat. Photonics*, vol. 4, pp. 58-61, 2010.
107. M. Virte, K. Panajotov, H. Thienpont and M. Sciamanna, "Deterministic polarization chaos from a laser diode", *Nat. Photonics.*, vol. 7, 60-65, 2013.
108. B. Wetzel, K. J. Blow, S. K. Turitsyn, G. Millot, L. Larger and J. M. Dudley, "Random walks and random numbers from supercontinuum generation," *Opt. Express*, vol. 20, pp. 11143-11152, 2012.

109. C. Gabriel, C. Wittmann, D. Sych, R. Dong, W. Mauerer, U. L. Andersen, C. Marquardt and G. Leuchs, "A generator for unique quantum random numbers based on vacuum states," *Nat. Photonics*, vol. 4, pp. 711-715, 2010.
110. W. Cheng, B. Bing, L. Yang, Z. Xiaoming, Y. Meng, C. Yuan, W. Jianfeng, Z. Shaohua, Z. Hongyan, S. Xiheng, M. Xiongfeng, R. Ji-Gang, Z. Jun, P. Cheng-Zhi, F. Jingyun, Z. Qiang and P. Jian-Wei, "Random Number Generation with Cosmic Photons," *Phys. Rev. Lett.*, vol. 118, 140402, 2017.
111. C. R. S. Williams, J. C. Salevan, X. Li, R. Roy and T. E. Murphy, "Fast physical random number generator using amplified spontaneous emission," *Opt. Express*, vol. 18, pp. 23584-23597, 2010.
112. X. Li, A. B. Cohen, T. E. Murphy and R. Roy, "Scalable parallel physical random number generator based on a superluminescent LED," *Opt. Lett.,* vol. 36, 1020-1022, 2011.
113. B. Sanguinetti, A. Martin, H. Zbinden and N. Gisin, "Quantum random number generation on a mobile phone," *Phys. Rev. X*, vol. 4, 031056, 2014.
114. T. Lunghi, J. B. Brask, C. C. W. Lim, Q. Lavigne, J. Bowles, A. Martin, H. Zbinden and N. Brunner, "Self-testing quantum random number generator," *Phys. Rev. Lett*., vol. 114, 150501, 2015.
115. http://www.phy.duke.edu/~rgb/General/dieharder.php
116. M. T. Rosenstein, J. J. Collins and C. J. A. De Luca, "Practical method for calculating largest Lyapunov exponents from small data sets," *Physica D*, vol. 65, pp. 117-134, 1993.
117. M. W. McCall, A. Favaro, P. Kinsler and A. Boardman, "A spacetime cloak, or a history editor," *J. Opt.*, vol. 13, 024003, 2011.
118. M. Fridman, A. Farsi, Y. Okawachi and A. L. Gaeta, "Demonstration of temporal cloaking," *Nature*, vol. 481, pp. 62-65, 2012.
119. J. M. Lukens, D. E. Leaird and A. M. Weiner, "A temporal cloak at telecommunication data rate," *Nature*, vol. 498, pp. 205-208, 2013.
120. D. J. Richardson et al. "Space-division multiplexing in optical fibres," *Nat. Photonics*, vol. 7, pp. 354-362, 2013.
121. E.J. Bochove, P.K. Cheo and G.G. King, "Self-organization in a multicore fiber laser array," *Opt. Lett.*, vol. 28, pp. 1200-1202, 2003.
122. M. Guasoni, V.V.Kozlov and S.Wabnitz, "Theory of modal attraction in bimodal birefringent optical fibers", *Opt. Lett*., vol. 38, pp. 2029-2031, 2013.
123. O. F. Anjum, P. Horak, Y. Jung, M. Suzuki, Y. Yamamoto, T. Hasegawa, P. Petropoulos, D. J. Richardson, and F. Parmigiani, "Bandwidth enhancement of inter-modal four wave mixing Bragg scattering by means of dispersion engineering," *APL Photonics*, vol. 4, 022902, 2019.
124. S. M. M. Friis, I. Begleris, Y. Jung, K. Rottwitt, P. Petropoulos, D. J. Richardson, P. Horak and F. Parmigiani, "Inter-modal four-wave mixing study in a two-mode fiber," *Opt. Express*, vol. 24, pp. 30338-30349, 2016.
125. E. Nazemosadat, A. Lorences-Riesgo, M. Karlsson and P. A. Andrekson, "Design of Highly Nonlinear Few-Mode Fiber for C-Band Optical Parametric Amplification," *J. Lightwave Technol.*, vol. 35, pp. 2810-2817, 2017.
126. M. H. Asghari and B. Jalali, "Anamorphic transformation and its application to time–bandwidth compression," *Appl. Opt*., vol. 52, pp. 6735-6743, 2013.
127. B. Jalali, J. C .K. Chan, A. Mahjoubfar, D. R. Solli and M. H. Asghari, "The Temporal Gearbox," arXiv:1612.04562, 2016.
128. A. N. Starodumov, "Pulse train compression up to terabit rates using four-wave mixing in birefringent fiber," *Optics communications*, vol. 124, pp. 365-372, 1996.
129. A. N. Starodumov, "New method of pulse train compression," *Soviet journal of quantum electronics*, vol. 22, pp. 1045, 1992.

CURRICULUM VITAE

Dr.-Ing. Julien FATOME
41 years old, born in April, 14th 1978
(Charleville-Mézières, France)
French, Married, 3 children.
OSA member
www.julienfatome.com

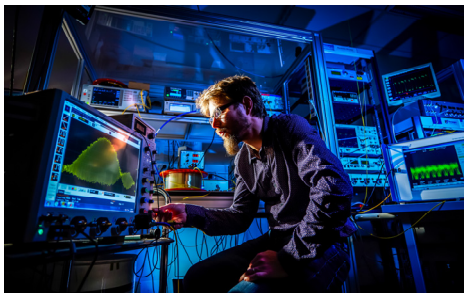

- **Academic positions**

  - **Since 2005: CNRS Research Engineer in Optics**

  Laboratoire Interdisciplinaire Carnot de Bourgogne (ICB), Dijon, France.
  UMR 6303 CNRS-Université Bourgogne Franche-Comté
  In charge of the telecom PICASSO platform.
  Research interest:
  - All-optical polarization control
  - Nonlinear Optics
  - Ultrafast nonlinear processing
  - Optical pulse train generation
  - Soft glass optical fibers
  - Spatial-division multiplexing

  Keywords: Optical fibre, nonlinear optics, all-optical processing, High bit-rate optical communication, polarization control.

  - **First term of 2017 and 2015: 2 stays as invited researcher at the University of Auckland (NZ)**

  Department of physics in the group of M. Erkintalo and S. Coen
  Research interest: Cavity solitons and polarization dynamics in Kerr resonators.

- **Education**

  2005: PhD thesis, delivered the 16th of December 2004
  Laboratoire de Physique de l'Université de Bourgogne.
  High speed pulse propagation at 160-Gbit/s in Dense Dispersion Management optical fiber lines.
  Keywords: Optical fiber, nonlinear optics, pulse generation, pulse characterization.
  2001: Engineering school
  Ecole Supérieure d'Ingénieurs de REcherche en Matériaux (ESIREM) in Dijon.
  Keywords: Materials, ceramic, polymer, glass, optics, electronics.

- **Funding ID** (>2.5 M€ managed since 2006), here the main Grants:
  - Marsden NZ project "Computing with walls of light", 2019-2022, AI, 31k$
  - ANR project APOFIS "All-optical processing in few-mode fibres", 2017-2018, 117k€.
  - ERC Starting Grant PETAL "Polarization condEnsation for Telecom AppLications". 2012-2017, 1.5 M€.
  - Labex Action project Phantom "PHotonic dATa cOMpression devicE". 60 k€, 2014-2015.
  - ANR project SO FAST "All-fibered Optical Sources for Telecommunication Applications". 166 k€, Consortium with ICB and UB Filiale, 2012-2014.
  - Program Synerjinov SysCom "Polarization Attractor prototype". 50 k€, 2011.

- ANR project PERSYST 2 “Research platform on telecommunication systems”. 150 k€. Consortium with FOTON (leader, Lannion) and Alcatel (Marcoussis), 2008-2011.
- ANR project FUTUR “Optical Functions for high bit rate transmission networks”. 240 k€. Consortium with FOTON (leader, Lannion), Alcatel (Marcoussis), IXFIBER (Lannion), LVC (Rennes) and Perfos (Lannion), 2007-2010.

- **PhD students & Postdocs supervising**

I supervised 5 PhDs and won 13 postdoctoral grants since 2007.

- Dr. Coraline Fortier (2007-2010, CNRS PhD grant, 2009 Award of the 10 best young French scientific women by the L’Oreal Foundation, now with TDF company)
- Dr. Anne Boucon (2010, ANR fellowship, now position in Thales)
- Dr. Philippe Morin (2009-2013, National priority scheme, ANR fellowship, now with CEA)
- Dr. Ibrahim El Mansouri (2010-2013, Regional PhD grant, now with APEX company)
- Dr. M. Guasoni (2012-2015, ERC then regional fellowship, granted by a Marie Skłodowska-Curie fellowship action at the Optoelectronics Research Centre, ORC)
- Dr. P-Y Bony, (2012-2015, ERC PhD fellowship, now in postdoc at DTU)
- Dr. M. Gilles, (2014-2017, ERC PhD fellowship, in a computer science company in Lausanne)
- Dr. J. Nuño Del-Campo (2015-2016, ERC fellowship, now in postdoc at CSIC Madrid)
- Dr. A. Bendahmane (2016-2017, ERC fellowship, now in postdoc in IRCICA, Lille)
- Dr. A. Akrout (2017, ERC fellowship)
- Dr. H. Zhang (2018, ANR fellowship)
- Dr. N. Berti (2016-2019, ERC and Regional fellowship)

- **Jury and Reviewing activities**

- Selection jury for CNRS research engineer position in XLIM Limoges (2006)
- Selection jury for ESIREM Engineering school admission.
- Reviewer for Nature Group, OSA, IEEE and Elsevier journals (50 reviews in the past 5 years).
- Evaluation panel for funding agencies: ANR (France), OCE (Canada)
- Part of the thesis jury for Amin Shoaie, PhD in EPFL, Lausanne (2016).
- Part of the thesis jury for François Copie, PhD in Phlam, Lille (2017).
- Member of the CLEO US technical committee, subcommittee S&I 11: Fiber Photonics

- **Teaching**

- I have taught an average of 10 hours per year including practical classes and tutorials.
- Biochemistry department 1st year: Optics
- Biochemistry department 2nd year: Physical measurements techniques
- Master’s degree, training session in optical communications.
- Since my PhD, numerous dissemination activities towards broad audience and schoolchildren (Experimentarium, radio programs, researcher’s night, YOL)

- **Awards**

- 2006 EDF Award of the best scientific thesis of the University of Dijon and Besancon
- 2005 SFP Award of the best oral presentation of the University of Dijon and Besancon

LIST OF PUBLICATIONS AND COMMUNICATIONS

I am co-author of more than 110 publications with more than 150 different co-authors. Here my tract-records and a full list of my publications.

Citations	All	Since 2014
Citations	4360	2965
h-index	33	26
i10-index	82	60

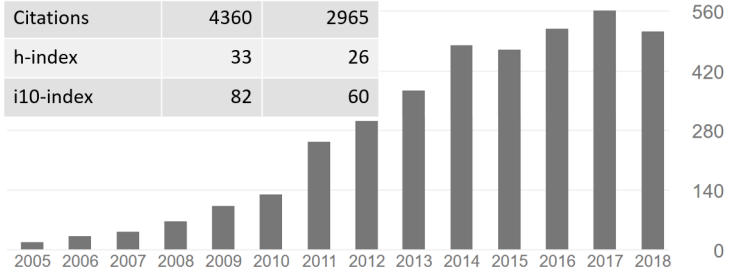

Track records (Google Scholar Sept. 2019)

P1. H. Zhang, M. Gilles, M. Guasoni, B. Kibler, A. Picozzi, and J. Fatome, *Isotropic polarization modulational instability in single mode conventional telecom fibers*, JOSA B 36, 2445-2451 (2019)

P2. A. Fusaro, N. Berti, M. Guasoni, H. R. Jauslin, A. Picozzi, J. Fatome, and D. Sugny, *Self-organization of the state of polarization in the mid-point of telecommunication optical fibers*, JOSA B 36, 2360-2368 (2019)

P3. K. Hammani, J. Fatome, and C. Finot, *Applications of sinusoidal phase modulation in temporal optics to highlight some properties of the Fourier transform*, Eur. J. Phys. 40, 055301 (2019)

P4. H. Zhang, M. Bigot-Astruc, L. Bigot, P. Sillard, and J. Fatome, *Multiple modal and wavelength conversion process of a 10-Gbit/s signal in a 6-LP-mode fiber*, Opt. Express 27, 15413-15425 (2019)

P5. A. Fusaro, N. Berti, M. Guasoni, H. R. Jauslin, A. Picozzi, J. Fatome, and D. Sugny, *Self-polarization effect in the middle point of an optical fiber*, Phys. Rev. A 99, 043826 (2019)

P6. M. Lamy, C. Finot, P. Colman, J. Fatome, G. Millot, G. Roelkens, K. Hammani, *Silicon Waveguides for High-Speed Optical Transmissions and Parametric Conversion Around 2 µm*, IEEE Photon. Technol. Lett. 31, 165-168 (2019)

P7. S. Perret, G. Fanjoux, L. Bigot, J. Fatome, G. Millot, J. M Dudley and T. Sylvestre, *Supercontinuum generation by intermodal four-wave mixing in a step-index few-mode fibre*, APL Photonics 4, 022905 (2019)

P8. A. Bendahmane, J. Fatome, C. Finot, G. Millot, and B. Kibler, *Selective generation of Kerr combs induced by asymmetrically phase-detuned dual pumping of a fiber ring cavity*, Opt. Lett. 43, 4449-4452 (2018)

P9. F. Audo, B. Kibler, J. Fatome and C. Finot, *Experimental observation of the emergence of Peregrine-like events in focusing dam break flows*, Opt. Lett. 43, 2864-2867 (2018)

P10. K. Hammani, L. Markey, M. Lamy, B. Kibler, J. Arocas, J. Fatome, A. Dereux, J-C. Weeber and C. Finot, *Octave Spanning Supercontinuum in Titanium Dioxide Waveguides*, Applied Science 8, 543 (2018)

P11. J. Morosi, N. Berti, A. Akrout, A. Picozzi, M. Guasoni, and J. Fatome, *Polarization chaos and random bit generation in nonlinear fiber optics induced by a time-delayed counter-propagating feedback loop*, Opt. Express 26, 845-858 (2018)

P12. R. Dupiol, A. Bendahmane, K. Krupa, J. Fatome, A. Tonello, M. Fabert, V. Couderc, S. Wabnitz, and G. Millot, *Intermodal modulational instability in graded-index multimode optical fibers*, Opt. Lett. 42, 3419-3422 (2017)

P13. M. Lamy, C. Finot, J. Fatome, M. Brun, P. Labeye, S. Nicolleti, A. Bogris, D. Syvridis, M. A. Ettabib, D. J. Richardson, P. Petropoulos and K. Hammani *10 GBit/s Optical Transmissions at 1.98 µm in cm-long SiGe Waveguides* Electron. Lett. (2017)

P14. A. Parriaux, M. Conforti, A. Bendahmane, J. Fatome, C. Finot, S. Trillo, N. Picqué, and G. Millot, *Spectral broadening of picosecond pulses forming dispersive shock waves in optical fibers,* Opt. Lett. 42, 3044-3047 (2017)

P15. M. Lamy, C. Finot, J. Fatome, J. Arocas, J.-C. Weeber and K. Hammani, *Demonstration of high speed optical transmission at 2 µm in titanium dioxide waveguides,* Applied Science 7, 631 (2017)

P16. M. Guasoni, F. Parmigiani, P. Horak, J. Fatome, and D. J. Richardson *Intermodal Four-Wave-Mixing and Parametric Amplification in km-long Fibers,* J. Ligthwave Technol. 35, 5296-5305 (2017)

P17. F. Audo, S. Boscolo, J. Fatome, B. Kibler, and C. Finot, *Nonlinear spectrum broadening cancellation by sinusoidal phase modulation,* Opt. Lett. 42, 2902-2905 (2017)

P18. Y. Wang, F. Leo, J. Fatome, M. Erkintalo, S. G. Murdoch and S. Coen, *Universal mechanism for the binding of temporal cavity solitons,* Optica 4, 855-863 (2017)

P19. J. Nuño, C. Finot, and J. Fatome, *Linear Sampling and Magnification Technique Based on Phase Modulators and Dispersive Elements: the Temporal Lenticular Lens,* Optical Fiber Technology 36, 125-129 (2017)

P20. M. Guasoni, J. Garnier, B. Rumpf, D. Sugny, J. Fatome, F. Amrani, G. Millot and A. Picozzi, *Incoherent Fermi-Pasta-Ulam, Recurrences and Unconstrained Thermalization Mediated by Strong Phase Correlations* Phys. Rev. X 7, 011025 (2017)

P21. M. Gilles, P-Y. Bony, J. Garnier, A. Picozzi, M. Guasoni and J. Fatome, *Polarization domain walls in optical fibres as topological bits for data transmission,* Nature Photonics 11, 102–107 (2017)

P22. S. Boscolo, J. Fatome and C. Finot, *Impact of amplitude jitter and signal-to-noise ratio on the nonlinear spectral compression in optical fibres,* Opt. Commun. 389, 197-202 (2017)

P23. A. Bendahmane, J. Fatome, C. Finot, G. Millot, and B. Kibler, *Coherent and incoherent seeding of dissipative modulation instability in a nonlinear fiber ring cavity,* Opt. Lett. 42, 251-254 (2017)

P24. A. Ceoldo, A. Bendahmane, J. Fatome, G. Millot, T. Hansson, D. Modotto, S. Wabnitz, and B. Kibler, *Multiple four-wave mixing and Kerr combs in a bichromatically pumped nonlinear fiber ring cavity,* Opt. Lett. 41, 5462-5465 (2016)

P25. J. Nuño, M. Gilles, M. Guasoni, C. Finot, and J. Fatome, *All-optical sampling and magnification based on XPM-induced focusing,* Opt. Express 24, 24921-24929 (2016)

P26. A. Fusaro, J. Garnier, C. Michel, G. Xu, J. Fatome, L.G. Wright, F.W. Wise and A. Picozzi, *Decoupled polarization dynamics of incoherent waves and bimodal spectral incoherent solitons,* Opt. Lett. 41, 3992-3995 (2016)

P27. M. Guasoni, P. Morin, P.-Y. Bony, S. Wabnitz and J. Fatome, *Self-induced polarization tracking, tunneling effect and modal attraction in optical fiber,* Optics & Laser Technology 80, **invited**, 247-259 (2016)

P28. J. Fatome, K. Hammani, B. Kibler and C. Finot, *80-GHz waveform generator by optical Fourier synthesis of four spectral sidebands,* Laser Phys. Lett. 13, 015102 (2016)

P29. J. Nuño, M. Gilles, M. Guasoni, B. Kibler, C. Finot and J. Fatome, *40-GHz pulse source based on XPM-induced focusing in normally dispersive optical fibers,* Opt. Lett. 41, 1110-1113 (2016)

P30. M. Guasoni, P. Y. Bony, M. Gilles, A. Picozzi, and J. Fatome, *All-optical signal processing based on self-induced polarization control in optical fibers,* J. Ligthwave Technol. 34, **invited**, 327-341 (2016)

P31. M. Guasoni, P-Y. Bony, M. Gilles, A. Picozzi and J. Fatome, *Fast and Chaotic Fiber-Based Nonlinear Polarization Scrambler,* IEEE Journal of Selected Topics in Quantum Electronics 22, 4402012 (2016)

P32. M. Conforti, A. Mussot, J. Fatome, A. Picozzi, S. Pitois, C. Finot, M. Haelterman, B. Kibler, C. Michel, and G. Millot, *Turbulent dynamics of an incoherently pumped passive optical fiber cavity: Quasisolitons, dispersive waves, and extreme events,* Phys. Rev. A 91, 023823 (2015)

P33. M. Guasoni, J. Fatome and S. Wabnitz, *Intensity noise-driven nonlinear fiber polarization scrambler*, Opt. Lett. 39, 5309-5312 (2014)

P34. O. Mouawad, F. Amrani, B. Kibler, J. Picot-Clémente, C. Strutynski, J. Fatome, F. Désévédavy, G. Gadret, J-C Jules, O. Heintz, E. Lesniewska and F. Smektala, *Impact of optical and structural aging in As2S3 microstructured optical fibers on mid-infrared supercontinuum generation*, Opt. Express 22, 23912-23919 (2014)

P35. P.Y. Bony, M. Guasoni, P. Morin, D. Sugny, A. Picozzi, H.R. Jauslin, S. Pitois and J. Fatome, *Temporal spying and concealing process in fibre-optic data transmission systems through polarization bypass*, Nat. Commun., 5:4678 (2014)

P36. J. Fatome, C. Finot, G. Millot, A. Armaroli and S. Trillo, *Observation of optical undular bores in multiple four-wave mixing*, Phys. Rev. X 4, 021022 (2014)

P37. Feng, J. Fatome, A. Sysoliatin, Y. K. Chembo, S. Wabnitz and C. Finot, *Wavelength conversion and temporal compression of pulse train using dispersion oscillating fibre,* Electron. Lett. 50, 768-770 (2014)

P38. O. Mouawad, J. Picot-Clémente, F. Amrani, C. Strutynski, J. Fatome, B. Kibler, F. Désévédavy, G. Gadret, J.-C. Jules, D. Deng, Y. Ohishi, and F. Smektala, *Multioctave midinfrared supercontinuum generation in suspended-core chalcogenide fibers*, Opt. Lett. 39, 2684-2687 (2014)

P39. S.Pitois and J. Fatome, *Dispositif innovant de stabilisation de la polarisation de la lumière,* Techniques de l'Ingénieur, re175 (2014)

P40. Frisquet, A. Chabchoub, J. Fatome, C. Finot, B. Kibler, and G. Millot, *Two-stage linear-nonlinear shaping of an optical frequency comb as rogue nonlinear-Schrödinger-equation-solution generator*, Phys. Rev. A 89, 023821 (2014)

P41. M. Guasoni, E. Assémat, P. Morin, A. Picozzi, J. Fatome, S. Pitois, H. R. Jauslin, G. Millot and D. Sugny, *A line of polarization attraction in highly birefringent optical fibers*, J. Opt. Soc. Am. B 31, 572-580 (2014)

P42. Finot, J. Fatome, A. Sysoliatin, A. Kosolapov and S. Wabnitz, *Competing Four-Wave Mixing Processes in Dispersion Oscillating Telecom Fiber*, Opt. Lett. 38, 5361-5364 (2013)

P43. J.-C.Weeber, T. Bernardin, M. G. Nielsen, K. Hassan, S. Kaya, J. Fatome, C. Finot, A. Dereux and N. Pleros, *Nanosecond thermo-optical dynamics of polymer loaded plasmonic waveguides*, Opt. Express 21, 27291-27305 (2013).

P44. B. Varlot, S. Wabnitz, J. Fatome, G. Millot and C. Finot, *Experimental generation of optical flaticon pulses*, Opt. Lett. 38, 3899-3902 (2013)

P45. S. Kaya, J.-C.Weeber, F. Zacharatos, K. Hassan, T. Bernardin, B. Cluzel, J. Fatome, and C. Finot, *Photo-thermal modulation of surface plasmon polariton propagation at telecommunication wavelengths*, Opt. Express 21, 22269-22284 (2013)

P46. P.-Y. Bony, M. Guasoni, E. Assémat, S. Pitois, D. Sugny, A. Picozzi, H. R. Jauslin, and J. Fatome, *Optical flip–flop memory and data packet switching operation based on polarization bistability in a telecommunication optical fiber*, J. Opt. Soc. Am. B 30, 2318-2325 (2013)

P47. J. Fatome, D. Sugny, S. Pitois, P. Morin, M. Guasoni, A. Picozzi, H. R. Jauslin, C. Finot, G. Millot, and S. Wabnitz, *All-optical regeneration of polarization of a 40 Gbit/s return-to-zero telecommunication signal*, Photon. Res. 1, 115-123 (2013)

P48. Savelii, F. Desevedavy, J.-C. Jules, G. Gadret, J. Fatome, B. Kibler, H. Kawashima, Y. Ohishi and F. Smektala, *Management of OH absorption in tellurite optical fibers and related supercontinuum generation*, Opt. Mat., 35, 1595-1599 (2013)

P49. J. Fatome, B. Kibler, and C. Finot, *High-quality optical pulse train generator based on solitons on finite background*, Opt. Lett. 38, 1663-1665 (2013)

P50. S. Wabnitz, C. Finot, J. Fatome and G. Millot, *Shallow water rogue wavetrains in nonlinear optical fibers*, Phys. Lett. A, 377, 932-939 (2013)

P51. J. Fatome, C. Finot, A. Armaroli, and S. Trillo, *Observation of modulationally unstable multi-wave mixing*, Opt. Lett. 38, 181-183 (2013)

P52. J. Fatome, I. El-Mansouri, J.-L. Blanchet, S. Pitois, G. Millot, S. Trillo and S. Wabnitz, *Even harmonic pulse train generation by cross-polarization-modulation seeded instability in optical fibers*, J. Opt. Soc. Am. B 30, 99-106 (2013)

P53. J. Fatome, S. Pitois, P. Morin, E. Assémat, D. Sugny, A. Picozzi, H. R. Jauslin, G. Millot, V. V. Kozlov, and S. Wabnitz, *A universal optical all-fiber Omnipolarizer*, Scientific Reports 2, 938 (2012)

P54. Savelli, O. Mouawad, J. Fatome, B. Kibler, F. Désévédavy, G. Gadret, J-C Jules, P-Y Bony, H. Kawashima, W. Gao, T. Kohoutek, T. Suzuki, Y. Ohishi and F. Smektala, *Mid-infrared 2000-nm bandwidth supercontinuum generation in suspended-core microstructured Sulfide and Tellurite optical fibers*, Opt. Express 20, 27083-27093 (2012)
P55. B. Stiller, P. Morin, D. M. Nguyen, J. Fatome, S. Pitois, E. Lantz, C. R. Menyuk and T. Sylvestre, *Demonstration of polarization pulling using a fiber-optical parametric amplifier*, Opt. Express 20, 27248-27253 (2012).
P56. K. Hammani, B. Kibler, J. Fatome, S. Boscolo, G. Genty, J. M. Dudley, G. Millot and C. Finot, *Nonlinear spectral shaping and optical rogue events in fiber-based systems*, Opt. Fiber Technol. 18, 248-256 (2012)
P57. M. G. Nielsen, J. C. Weeber, K. Hassan, C. Finot, J. Fatome, S. Kaya, L. Markey, O. Albrektsen, S. I. Bozhevolnyi, G. Millot and A. Dereux, *Grating Couplers for Fiber-to-Fiber Characterizations of Stand-Alone Dielectric Loaded Surface Plasmon Waveguide Components*, J. Lightw. Technol. 30, 3118-3125 (2012)
P58. B. Kibler, J. Fatome, C. Finot, G. Millot, G. Genty, B. Wetzel, N. Akhmediev, F. Dias and J. M. Dudley, *Observation of Kuznetsov-Ma soliton dynamics in optical fibre*, Scientific Reports, 2, 463 (2012)
P59. P. Morin, S. Pitois, and J. Fatome, *Simultaneous polarization attraction and Raman amplification of a light beam in optical fibers*, J. Opt. Soc. Am. B 29, 2046-2052 (2012)
P60. P. Morin, S. Pitois, C. Finot and J. Fatome, *Light-by-light polarization control and stabilization in optical fibers for telecommunication applications*, Proc. SPIE 8434, 84340X (2012)
P61. J. Fatome, B. Kibler, E. R. Andresen, H. Rigneault, and C. Finot, *All-fiber spectral compression of picosecond pulses at telecommunication wavelength enhanced by amplitude shaping*, Appl. Opt. 51, 4547-4553 (2012)
P62. Savelii, J. C. Jules, G. Gadret, B. Kibler, J. Fatome, M. El-Amraoui, N. Manikandan, X. Zheng , F. Désévédavy, J. M. Dudley, J. Troles, L. Brilland, G. Renversez and F. Smektala, *Suspended core tellurite glass optical fibers for infrared supercontinuum generation,* Opt. Mat., 33, 1661-1666 (2011)
P63. P. Morin, J. Fatome, C. Finot, S. Pitois, R. Claveau and G. Millot, *All-optical nonlinear processing of both polarization state and intensity profile for 40 Gbit/s regeneration applications*, Opt. Express, 19, 17158-17165 (2011)
P64. El Mansouri, J. Fatome, C. Finot, M. Lintz and S. Pitois, *All-Fibered High-Quality Stable 20-GHz and 40-GHz Picosecond Pulse Generators for 160-Gbit/s OTDM Applications*, IEEE Photon. Technol. Lett., 23, pp.1487-1489 (2011)
P65. V. V. Kozlov, J. Fatome, P. Morin, S.Pitois, G. Millot and S. Wabnitz, *Nonlinear repolarization dynamics in optical fibers: transient polarization attraction*, J. Opt. Soc. Am. B, 28, 1782-1791 (2011)
P66. Finot, J. Fatome, S. Pitois, E. Pincemin and G. Millot, *Active Mamyshev Regenerator*, Optical Review, 18, 257-263 (2011)
P67. J. Fatome, P. Morin, S. Pitois and G. Millot, *Light-by-Light polarization control of 10-Gbit/s RZ and NRZ telecommunication signals*, Journal of Selected Topics in Quantum Electronics, 18, 621-628 (2011)
P68. J. Fatome, B. Kibler, M. El-Amraoui, J-C. Jules, G. Gadret, F. Desevedavy and F. Smektala, *Mid-infrared extension of supercontinuum in a chalcogenide suspended core fibre through soliton gas pumping*, Electron. Lett., 47, 398-400 (2011)
P69. C. Courvoisier, J. Fatome and C. Finot, *Measurement of residual chromatic dispersion and OSNR via nonlinear spectral evolution*, IEEE Photon. Technol. Lett., 23, 537-539 (2011)
P70. H. T. Nguyen, C. Fortier, J. Fatome, G. Aubin, and J-L. Oudar, *A passive all-optical device for 2R regeneration based on the cascade of two high speed saturable absorbers*, J. Lightw. Technol., 29, 1319-1325 (2011)
P71. C. Finot and J. Fatome, *Experimental demonstration of an ultrafast all-optical bit-error indicating scheme*, Microwave and Optical Technology Letters, 53, 392–395 (2011)
P72. K. Hammani, B. Kibler, C. Finot, P. Morin, J. Fatome, J. M. Dudley and G. Millot, *Peregrine soliton generation and breakup in standard telecommunications fiber*, Opt. Lett., 36, 112-114 (2011)
P73. M. El-Amraoui, G. Gadret, J. C. Jules, J. Fatome, C.Fortier, F. Désévédavy, I. Skripatchev, Y. Messaddeq, J. Troles, L. Brilland, W. Gao, T. Suzuki, Y. Ohishi and F. Smektala, *Microstructured chalcogenide optical fibers from As2S3 glass: towards new IR broadband sources*, Opt. Express, 18, 26655-26665 (2010)
P74. B. Kibler, J. Fatome, C. Finot, G. Millot, F. Dias, G. Genty, N. Akhmediev and J. M. Dudley, *The Peregrine soliton in nonlinear fibre optics*, Nature Physics, 6, 790-795 (2010)
P75. C. Finot and J. Fatome, *All-optical fiber-based ultrafast amplitude jitter magnifier*, Opt. Express, 18, 18697-18702 (2010)
P76. J. Fatome and C. Finot, *Scaling guidelines of a soliton-based power limiter for 2R-optical regeneration applications*, J. Lightw. Technol., 28, 2552-2559 (2010)
P77. J. Fatome, S. Pitois, P. Morin, and G. Millot, *Observation of light-by-light polarization control and stabilization in optical fibre for telecommunication applications*, Opt. Express, 18, 15311-15317 (2010)
P78. P. Morin, B. Kibler, J. Fatome, C. Finot, and G. Millot, *Group birefringence cancellation in highly birefringent photonic crystal fibre at telecommunication wavelengths*, Electron. Lett., 46, 525-526 (2010)
P79. J. Fatome, S. Pitois, C. Fortier, B. Kibler, C. Finot, G. Millot, C. Courde, M. Lintz and E. Samain, *Multiple four wave mixing in optical fibers: 1.5-3.4-THz femtosecond pulse sources and real-time monitoring of a 20-GHz picosecond source*, Opt. Commun., 283, 2425-2429 (2010)
P80. M. El-Amraoui, J. Fatome, J. C. Jules, B. Kibler, G. Gadret, C. Fortier, F. Smektala, I. Skripatchev, C.F. Polacchini, Y. Messaddeq, J. Troles, L. Brilland, M. Szpulak, and G. Renversez, *Strong infrared spectral broadening in low-loss As-S chalcogenide suspended core microstructured optical fibers*, Opt. Express, 18, 4547-4556 (2010)
P81. M. Gay, M. Costa e Silva, T. N. Nguyen, L. Bramerie, T. Chartier, M. Joindot, J.C. Simon, J. Fatome, C. Finot and J.L. Oudar, *Bit Error Rate Assessment of 170 Gbit/s Regeneration using a Saturable Absorber and a Nonlinear-Fiber-based Power Limiter*, IEEE Photon. Technol. Lett., 22, 158-160 (2010)
P82. C. Finot, K. Hammani, J. Fatome, J. M. Dudley and G. Millot, *Selection of extreme events generated in Raman fiber amplifiers through spectral offset filtering*, Journal of Quantum Electronics, 2, 205-213 (2010)
P83. T. N. Nguyen, T. Chartier, L. Bramerie, M. Gay, Q. T. Le, S. Lobo, M. Joindot, J-C. Simon, J. Fatome, and C. Finot, *Self-phase-modulation-based 2R regenerator including pulse compression and offset filtering for 42.6 Gbit/s RZ-33% transmission systems*, Opt. Express, 17, 17747-17757 (2009)

P84. J. Fatome, S. Pitois and G. Millot, *Experimental evidence of Brillouin-induced polarization wheeling in highly birefringent optical fibers*, Opt. Express, 17, 12612-12618 (2009)
P85. B. Kibler, T. Martynkien, M. Szpulak, C. Finot, J. Fatome, J. Wojcik, W. Urbanczyk and S. Wabnitz, *Nonlinear femtosecond pulse propagation in an all-solid photonic bandgap fiber*, Opt. Express, 17, 10393-10398 (2009)
P86. J. Fatome, C. Fortier, T. N. Nguyen, T. Chartier, F. Smektala, K. Messaad, B. Kibler, S. Pitois, G. Gadret, C. Finot, J. Troles, F. Desevedavy, P. Houizot, G. Renversez, L. Brilland and N. Traynor, *Linear and nonlinear characterizations of chalcogenide photonic crystal fibers*, J. Lightw. Technol., 27 (11), 1707-1715 (2009)
P87. J. Fatome, C. Fortier and S. Pitois, *Practical design rules for single-channel ultra-high-speed Dense Dispersion Management Telecommunication systems*, Opt. Commun., 282, 1427-1434 (2009)
P88. S. Pitois, C. Finot, J. Fatome and G. Millot, *Design of a continuously tunable delay line using vectorial modulational instability and chromatic dispersion in optical fibers*, Opt. Commun., 282, 1016-1019 (2009)
P89. K. Hammani, C. Finot, S. Pitois, J. Fatome and G. Millot, *Real time measurement of long parabolic optical similaritons*, Electron. Lett., 44, 1239-1240 (2008)
P90. C. Fortier, J. Fatome, S. Pitois, J-P. Couvercelle, M-L. Leonard, E. Pincemin and F. Reynaud, *Stretched fiber based dispersion compensating module for ultra-high-speed Telecommunication systems*, Electron. Lett., 44, 1025-1027 (2008)
P91. C. Fortier, B. Kibler, J. Fatome, C. Finot, S. Pitois and G. Millot, *All-fibered high-quality low duty-cycle 160-GHz femtosecond pulse source*, Laser Physics Letters, 5, 817-820 (2008)
P92. C. Fortier, J. Fatome, S. Pitois, F. Smektala, G. Millot, J. Troles, F. Desevedavy, P. Houizot, L. Brilland and N. Traynor, *Experimental investigation of Brillouin and Raman scattering in a 2SG sulfide glass microstructured chalcogenide fiber*, Opt. Express, 16, 9398-9404 (2008)
P93. S. Pitois, J. Fatome and G. Millot, *Polarization attraction using counter-propagating waves in optical fiber at telecommunication wavelengths*, Optics Express, 16, 6646-6651 (2008)
P94. C. Finot, T. N. Nguyen, J. Fatome, T. Chartier, S. Pitois, L. Bramerie, M. Gay and J-C. Simon, *Numerical study of an optical regenerator exploiting self-phase modulation and spectral offset filtering at 40 Gbit/s*, Opt. Commun., 281, 2252-2264 (2008)
P95. J. Fatome, C. Finot, S. Pitois and G. Millot, *All-fibered high-quality low duty-cycle picosecond high repetition rate pulse sources*, Annales de Physiques, 32, 67-70 (2007)
P96. B. Barviau, C. Finot, J. Fatome, S. Pitois and G. Millot, *Generation from continuous waves of frequency combs with large overall bandwidth and tunable central wavelength*, Electron. Lett., 43, 886-887 (2007)
P97. C. Finot, J. Fatome, S. Pitois and G. Millot, *All-fibered high-quality low duty-cycle 20-GHz and 40-GHz picosecond pulse sources*, IEEE Photon. Technol. Lett., 19, 1711-1713 (2007)
P98. J. Fatome, S. Pitois, D. Massoubre, J-L. Oudar, and G. Millot, *Cascadability and reshaping properties of a saturable absorber inserted inside a RZ transmission line for future 160-Gbit/s all-optical 2R-regenerators*, Opt. Commun., 279, 364-369 (2007)
P99. J. Fatome, J. Garnier, S. Pitois, M. Petit, G. Millot, M. Gay, B. Clouet, L. Bramerie and J-C. Simon, *All-Optical Measurements of Background, Amplitude and Timing Jitter for high speed pulse trains or PRBS sequences using autocorrelation function*, Opt. Fiber Technol., 14, 84-91 (2008)
P100. J. Fatome, S. Pitois, A. Kamagate, G. Millot, D. Massoubre and J-L. Oudar, *All-optical reshaping based on a passive saturable absorber microcavity device for future 160-Gb/s applications*, IEEE Photon. Technol. Lett., 19, 245-247 (2007)
P101. J. Fatome, S. Pitois and G. Millot, *20-GHz to 1-THz repetition rate pulse sources based on multiple four wave mixing in optical fibers*, Journal of Quantum Electronics, 42, 1038-1046, (2006)
P102. J. Fatome, D. Massoubre, S. Pitois, G. Millot, J. Landreau, J. Decobert and J-L. Oudar, *Component with a saturable absorber for the completely optical regeneration at ultra-high repetition rate*, Journal de Physique IV, 135, 157-159 (2006)
P103. J. Fatome, S. Pitois and G. Millot, *320/640-GHz high quality pulse sources based on multiple Four Wave Mixing in highly nonlinear optical fiber*, Electron. Lett., 41, 1391-1392 (2005)
P104. Massoubre, J-L. Oudar, J. Fatome, S. Pitois, G. Millot, J. Decobert and J. Landreau, *All-optical extinction ratio enhancement of a 160 GHz pulse train using a saturable absorber vertical microcavity*, Opt. Lett., 31, 537-539 (2006)
P105. S. Pitois, C. Finot, J. Fatome, B. Sinardet and G. Millot, *Generation of 20-GHz picosecond pulse trains in the normal and anomalous dispersion regimes of optical fibers*, Opt. Commun., 260, 301-306 (2006)
P106. J. Fatome, S. Pitois, P. Tchofo Dinda, D. Erasme and G. Millot, *Comparison of conventional and dense dispersion managed systems for 160 Gb/s transmissions*, Opt. Commun., 260, 548-553 (2006)
P107. J. Fatome, S. Pitois and G. Millot, *Measurement of Nonlinear and Chromatic Dispersion Parameters of Optical Fibers using Modulation Instability*, Opt. Fiber Technol., 12, 243-250 (2006)
P108. J. Fatome, S. Pitois, P. Tchofo Dinda, G. Millot, E. Le Rouzic, B. Cuenot, E. Pincemin and S. Gosselin, *Effectiveness of fiber lines with symmetric dispersion swing for 160 Gb/s terrestrial transmission systems*, IEEE Photon. Technol. Lett., 16, 2365-2367 (2004)
P109. J. Fatome, S. Pitois and G. Millot, *Influence of third-order dispersion on the temporal Talbot effect*, Opt. Commun., 234, 29-34 (2004)
P110. J. Fatome, S. Pitois and G. Millot, *Sensitivity of SHG-FROG for the Characterisation of Ultrahigh-Repetition-Rate Telecommunication Laser Sources*, Opt. Fiber Technol., 10, 73-78 (2004)
P111. J. Fatome, S. Pitois, P. Tchofo Dinda and G. Millot, *Experimental demonstration of 160-GHz densely dispersion-managed soliton transmission in a single channel over 896 km of commercial fibers*, Opt. Express, 11, 1553-1558 (2003)
P112. P. Tchofo Dinda, A. Labruyere, A. B. Moubissi, K. Nakkeeran, J. Fatome, S. Pitois and G. Millot, *Methodology for designing densely dispersion-managed optical fiber systems for ultra-fast optical communication Annales des Télécommunications*, invited paper, 58, n°11-12, 1785-1808 (2003)
P113. S. Pitois, J. Fatome and G. Millot, *Generation of a 160-GHz transform-limited pedestal-free pulse train through multiwave mixing compression of a dual-frequency beat signal*, Opt. Lett., 27, 1729-1731 (2002)
P114. J. Garnier, J. Fatome, and G. Le Meur, *Statistical analysis of pulse propagation driven by polarization mode dispersion*, J. Opt. Soc. Am. B, 19, 1968-1977 (2002)

Invited conferences

I am co-author of more than 100 conference proceedings including 21 given invited talks and 3 postdeadlines.

C1. H. Zhang, M. Bigot-Astruc, L. Bigot, P. Sillard, and J. Fatome, "Multiple Modal and Wavelength Conversion Process of a 10-Gbit/s Signal in a 6-LP-Mode Fiber," CLEO US 2019, **chair choice**, 05-10 Mai 2019, San José, CA (US).
C2. J. Fatome, Polarization Domain Walls in Optical Fibres and Kerr resonators, invited, workshop on recent advances in ultrafast nonlinear fiber optics, **invited**, 04-05 Dec. 2018, Lille, France.
C3. M. Gilles, P-Y Bony, M. Guasoni, A. Picozzi and J. Fatome, Polarization Domain Walls in Optical Fibres, ECOC, **invited**, Tu4A.5, 22-26 Spet. 2018, Rome, Italy.
C4. J. Fatome, Y. Wang, B. Garbin, B. Kibler, A. Bendahmane, N. Berti, G. -. Oppo, F. Leo, S. G. Murdoch, M. Erkintalo, and S. Coen, "Flip-Flop Polarization Domain Walls in a Kerr Resonator," in Advanced Photonics 2018, **postdeadline paper** JTu6F.2, 2-5 july, Zurich Switzerland.
C5. J. Fatome, Polarization domain walls as bit entities in optical fibers and Kerr resonators, invited, Progress in Nonlinear Photonics: Waveguides and Resonators, **invited**, March 28 - 29, 2018, Bath, UK.
C6. J. Nuño, C. Finot, G. Millot, S. Trillo and J. Fatome, Ballistic dispersive shock waves in optical fibers, Nonlinear Photonics, **postdeadline paper**, 5-8 Sept. 2016, Sydney, Australia.
C7. M. Gilles, P-Y. Bony, J. Garnier, A. Picozzi, M. Guasoni and J. Fatome, Universal polarization domain walls in optical fibers as topological bit-entities for data transmission, Nonlinear Photonics, **postdeadline paper**, 5-8 Sept. 2016, Sydney, Australia.
C8. J. Fatome, Shaping of light through cross-polarized phase modulation, Auckland Photonics Workshop, **invited,** 02 sept. 2016, Auckland, New-Zealand.
C9. J. Fatome, Nonlinear Polarization Manipulation in Optical Fibers, Frontier in Optics (FIO 2015), **invited**, 18-22 Oct. 2015, San Jose, US.
C10. P. Y. Bony, M. Guasoni, S. Pitois, A. Picozzi, D. Sugny, H. Jauslin, G. Millot, S. Wabnitz and J. Fatome, *All-optical polarization control for telecom applications*, Optical Fiber Communications (OFC 2015), **invited**, 22-26 March. 2015, Los Angeles, US.
C11. J. Fatome, S. Pitois, P. Morin, P. Y. Bony, M. Guasoni, A. Picozzi, D. Sugny, H. Jauslin, G. Millot and S. Wabnitz,*All-optical control of polarization state in optical fibre for telecom applications*, IEEE Photonics Conference (IPC 2014), **invited**, 12-16 Oct. 2014, San Diego, US.
C12. P-Y. Bony, M. Guasoni, S. Pitois, P. Morin, D. Sugny, A. Picozzi, H. R. Jauslin, G. Millot, S. Wabnitz and J. Fatome, *All-optical polarization control in fibers for telecom applications*, Advanced Laser Technologies (ALT14), **invited,** 6-10 Oct. 2014, Cassis, France.
C13. J. Fatome, S. Pitois, P. Morin, P. Y. Bony, M. Guasoni, A. Picozzi, D. Sugny, H. Jauslin and S. Wabnitz, *All-optical scrambling process in optical fibers*, International Conference on Transparent Optical Networks, **invited**, 6-10 Juil.2014, Graz, Austria.
C14. P. Morin, P. Y. Bony, M. Guasoni, S. Pitois, D. Sugny, A. Picozzi, H. R.Jauslin G. Millot, S. Wabnitz and J. Fatome,*Auto-organisation de la polarisation dans les fibres optiques: L'Omnipolariseur*, Journée Électromagnétisme, Polarisation et Optique Statistique EPOS 2013,**invited**, 19 Nov., Marseilles, 2013.
C15. J. Fatome, S. Pitois, P. Morin, P.Y.Bony, M. Guasoni, A. Picozzi, D. Sugny, H. Jauslin, G. Millot and S. Wabnitz,*Self-organization of polarization state in optical fibers for Telecommunication applications*, Spatio-Temporal Complexity in Optical Fibers Workshop, **invited**, 16-18 Sept., Como, 2013.
C16. P. Morin, S. Pitois, P. Y. Bony, M. Guasoni, D. Sugny, A. Picozzi, H. Jauslin, G. Millot, S. Wabnitz and J. Fatome, L'Omnipolariseur : *Démonstration expérimentale d'un phénomène d'auto-polarisation de la lumière dans les fibres optiques*, Journées nationales d'optique guidées, JNOG 2013, **invited**, 8-11 July, Villetaneuse.
C17. P.-Y. Bony, P. Morin, M. Guasoni, S. Pitois, and J. Fatome *All-optical polarization-based temporal cloaking*, European Conference on Lasers and Electro-Optics, CLEO Europe 2013, **Postdeadline** PD-B.8, 12-16 May, Munich, 2013.
C18. J. Fatome, S. Pitois, and P. Morin,*All-optical Control of Polarization State in Optical Fibers for Telecommunication Applications*, 2012 SIAM Conference on Nonlinear Waves and Coherent Structures (NW12), **invited**, june 2012, Seattle États-Unis (2012)
C19. J. Fatome, P. Morin, S. Pitois, C. Finot and G. Millot,*Light-by-light polarization control and its applications in optical communications*, **invited**, Nonlinear Photonics, Saint Petersburg, 24 aout-26 aout 2011.
C20. J. Fatome, S. Pitois, P. Morin, C. Finot and G. Millot,*Light-by-Light polarization control for telecommunication applications,* International Conference on Transparent Optical Networks, **invited**, Juin 27-Juillet01, 2010, Munich, Allemagne.
C21. J. Fatome, S. Pitois, P. TchofoDinda et G. Millot,*Propagation d'impulsions ultra-courtes à 160-Gbit/s dans des lignes de fibres optiques gérées en dispersion*, 6ième Journées des Ecoles Doctorales Louis Pasteur et Carnot (JED 2005), Mai 18-19, 2005, Dijon, France. **(Best thesis award from EDF)**
C22. J. Fatome, S. Pitois and G. Millot,*Generation and characterization of ultrahigh-repetition-rate pulse trains for optical fiber communications lines*, 25th International Congress on High Speed Photography and Photonics (HSPP 2002), **invited**, Sept. 29 - Oct. 4, 2002, Beaune, France.

Book chapters

B1. "*Polarization manipulation in optical fibres*" by M. Guasoni and J. Fatome in *Pulse Shaping and Signal Processing using Optical Fibres,* Wiley, 2015.

B2. *"Experiments on Breathers in Nonlinear Fibre Optics"* by B. Kibler, J. Fatome, C. Finot and G. Millot, in *Rogue and Shock Waves in Nonlinear Dispersive Media* by M. Onorato, S. Resitori and F. Baronio, Lecture Notes in Physics book series (LNP, volume 926), Springer 2016.

B3. *"Temporal and Spectral Nonlinear Pulse Shaping Methods in Optical Fibers"* by S. Boscolo, J. Fatome, S. K. Turitsyn, G. Millot and C. Finot *in All-optical signal processing,* 105-128 Springer 2015.

Patents

Pat1. S. Pitois and J. Fatome, *Système de contrôle de polarisation tout-optique a faisceau de pompe contra-propagative*, Brevet N°FR 09/04451 (2009)

Pat2. C. Finot and J. Fatome, *Dispositif et procédé de traitement d'un signal optique*, Brevet FR n°10/52276 (2010)

Pat3. S. Pitois, J. Fatome, P. Morin and G. Millot, *Procédé et dispositif pour le contrôle d'un paramètre physique d'un signal optique*, Brevet FR n° 11/02472 (2011)

Pat4. C. Finot, J. Fatome and B. Kibler, *Générateur et procédé pour la génération d'impulsions optiques à haut taux de répétition*, Brevet FR n° 13/50331 (2013)

Broad audience and Vulgarization

- Several times in the news of CNRS and INP.
- Open Lab in ICB, 2018.
- European researchers' night, Atheneum, sept. 2015.
- International year of light in Burgundy 2014-2015.
- Petal.inside (www.facebook.com/petal.inside), Fev. 2013-2017.
- « Scientifique, toi aussi » (CEA), janv. 2013
- 10 years of Expérimentarium, CSGA, mai 2011.
- Radio « le microscope et la blouse », radio Campus, mai 2011.
- European researchers' night, Atheneum, sept. 2009.
- Radio de vulgarisation scientifique, Dijon radio culture, juin 2008.
- European researchers' night, Atheneum, sept. 2007.
- Radio « La tête au carré » in France Inter, Paris, mars 2007.
- Materials night, Atheneum, Nov.,2006.
- European researchers' night, Atheneum, sept. 2006.
- Vibration night, Atheneum, Oct., 2005.
- V6. Participation fête de la science, chambre du commerce et de l'industrie, 2005.
- Radio « Le microscope et la blouse », radio campus 2005.
- TV « Fugues », France 3 régionale Bourgogne Franche-Comté, 2005.
- Festival « A pas contés » Dijon, 2005.
- Festival «La bricole, Art et Technologie » Dijon, 2004.
- Expérimentarium, *Lumière sous la mer,* de 2001 à 2005.